

Multi-frequency observations
of the outer solar corona with the
Gauribidanur radioheliograph

Thesis submitted for the degree of Doctor of Philosophy
in the Faculty of Science, Bangalore University

by

R.RAMESH



Indian Institute of Astrophysics
Bangalore

1998

Declaration

I hereby declare that the matter embodied in this thesis is the result of the work carried out by me in the Indian Institute of Astrophysics, Bangalore. I further declare that no part of this work has been submitted for the award of any other degree, diploma, membership, associateship or similar title of any university or institution.

Certified



Prof.R.Cowsik

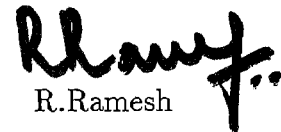
(Thesis Supervisor)



Director

Indian Institute of Astrophysics
Bangalore-560 034

Oct. 27, 1998



R.Ramesh

(Ph.D Candidate)

Abstract

A new radioheliograph dedicated to observations of the outer corona of the Sun has been built by the Indian Institute of Astrophysics at the Gauribidanur radio observatory and is in operation since April 1997. This instrument (hereafter referred to as the Gauribidanur radioheliograph, GRH) is capable of producing two-dimensional pictures of the solar corona in the frequency range 40 - 150 MHz (a height range of $\approx 0.1 - 0.6 R_{\odot}$ above the photosphere). At present this is the only instrument of its kind in the world in the above frequency range for regular observations of the Sun.

The GRH is a T-shaped array with a long E-W arm and a short South arm. It works on the well known principles of synthesis imaging where the outputs from the individual antenna groups are taken separately to the receiver building and fed to a receiver system which measures the spatial coherence between the received signals. Since the GRH has 32 antenna groups (16 E-W + 16 South), a 1024 channel digital receiver is used to correlate the signals received by the different antenna groups. Included in this thesis is a description of the receiver system and its various sub-units. The details of the Walsh switching scheme and its effectiveness in removing the contribution from unwanted signals are described. The tests carried out to measure the cross-talk between the input signals to the correlator, DC offset in the A/D convertors, effects of the residual errors in the correlator system on the measured visibilities in the u-v plane are discussed in detail.

One of the biggest challenges in the synthesis imaging of any radio source is the removal of instrumental/propagation errors from the observed quantities. There are several techniques in use at present which derive the correction terms from the observed quantities themselves. Some of the practical and technical problems in applying the existing techniques to solar observations

with arrays like the GRH and the details of the scheme that we have developed are given. The successful use of our scheme in practice is illustrated by comparing the maps obtained with the GRH with those made at other wavelengths as well as using other techniques. A quantitative estimate of the possible errors in the present scheme is also carried out.

The estimation of electron density at various heights in the ambient corona as well as above the active regions is generally done using density models derived from the white light data obtained during solar eclipses and using coronagraphs. From radio observations, it is possible to calculate the altitude of the emitting regions and the density, in an independent way, if the source under observation shows regular movement across the solar disk. Using the one-dimensional observations carried out with the E-W arm of the GRH at 51 and 77 MHz, the altitudes of the plasma levels at these frequencies are derived.

Two-dimensional maps obtained with the GRH on quiet days when no non-thermal emission (burst activity) was seen in our records, were used to study the thermal emission from the undisturbed corona. The effects of coronal streamers, holes, and scattering by small-scale density inhomogeneities in the corona on the observed quiet Sun emission and the low values of the observed brightness temperature are discussed.

An understanding of coronal mass ejections (CMEs) and its origin is one of active areas of research in the field of solar physics. An attempt has been made to identify the pre-event signatures of the CMEs from the radio data observed with the GRH. In one case study, the mass of the coronal material that was associated with a halo CME has been estimated from the global restructuring of the corona in the aftermath of the event.

Acknowledgements

I am grateful to Prof.R.Cowsik for having kindly agreed to be my thesis supervisor, despite his heavy work schedule as the Director of the institute. Without his help and support for the Gauribidanur radioheliograph project at various stages, this thesis would not have taken shape.

I sincerely thank Prof.M.C.Radhakrishna, Prof.A.R.Hanumanthappa and Prof.M.N.Anandram of the Physics department, Bangalore University for their guidance and help in matters related to this thesis with the university.

I take this opportunity to express my gratitude to Prof.Ch.V.Sastry to whom I owe this thesis. The innumerable hours of discussions I had with him helped me in learning the basics of radio astronomy and solar radio physics.

I would like to thank my colleagues of the radio astronomy group at the institute, Dr.K.R.Subramanian from whom I learnt the practical details of the construction of analog receiver systems, and Mr.M.S.SundaraRajan without whom the digital correlator receiver for the heliograph would not have been possible.

Prof.Hiroshi Nakajima of the Nobeyama radio observatory, Japan assisted in procuring the correlator chips for the heliograph. I would like to thank him for his help and suggestions at various stages of my thesis work. I acknowledge the help extended by Prof.Govind Swarup in obtaining the correlator chips.

It is my sincere duty to thank Dr.Masanori Nishio of the Kagoshima University, Japan who introduced me to the technique of phase calibration of radio interferometer arrays using redundant baselines, during his visit to the institute under the Indo-Japanese collaborative program.

I thank Dr.N.Udayashankar of Raman Research Institute for his help at various stages of my thesis work and also for his critical comments on the chapters on digital techniques and calibration presented in this thesis.

My thanks are due also to my colleague R.Sridhar, Dr.Mark Wieringa of the Australia Telescope National Facility and Kumar Golap of the University of Mauritius for their help in developing the phase calibration scheme for the heliograph. The self-calibration of the Gauribidanur data using AIPS would not have been possible but for the help of Dr.Ketan Desai of the National Radio Astronomy Observatory, USA. I thank him.

I thank Dr.N.Gopalswamy of the Catholic University of America and Dr.G.Thejappa of the University of Maryland, USA for their kind help in improving the clarity of the chapters on CMEs and quiet Sun presented in this thesis. I would also like to thank Prof.P.Venkatakrishnan and Prof.Vinod Krishan for critically reading the thesis.

With pleasure I thank Dr.K.R.Anantharamaiah, Dr.A.A.Deshpande and other staff members of Raman Research Institute for their help and support in carrying out various activities at the Gauribidanur radio observatory.

The successful operation of the heliograph is due to the hardwork and cooperation of Ebenezer, Hameed, Gowda, Anwar, Rajasekar, Ashwathappa and other supporting staff at the Gauribidanur radio observatory. I sincerely thank them.

It is my duty to thank Prof.S.S.Hasan, members of the Board of Graduate studies and my friends in the institute for their timely help at different stages of my thesis work.

Contents

1	Introduction	5
2	Antenna system	10
2.1	Introduction	10
2.2	Antenna parameters	11
2.3	Array configuration	16
2.4	Element grouping	17
2.4.1	E-W arm	17
2.4.2	South arm	20
2.5	Signal transmission to the receiver building	20
2.6	Grating lobes	22
2.7	Delay shifters	24
A	Appendix	27
A.1	BALUN transformer	27
A.1.1	Quarter-wave ($\lambda/4$) transmission line	27
A.1.2	Feeding the LPD through a co-axial cable	28
A.2	Coherence loss	29
3	Receiver system	30
3.1	Front end analog receiver	30

3.2	Back end digital receiver	32
3.2.1	Walsh switching	33
3.2.2	DC offset in the A/D convertor	35
3.2.3	Cross-talk between antenna signals	37
3.2.4	The 1024 Channel digital correlator	41
3.2.5	Data acquisition	45
3.3	Testing of the correlator chips	45
3.4	Correlator input level Vs residual offset	47
B	Appendix	49
B.1	Estimation of the correlation coefficient ρ_m from the measured correlation count in a one-bit correlator	49
B.2	Amplitude information using a one-bit correlator	51
B.2.1	Calibration of the threshold level V_{th}	55
4	Calibration and Imaging	57
4.1	Introduction	57
4.1.1	External calibration	59
4.1.2	Internal calibration	60
4.1.3	Self-calibration	61
4.1.4	Redundancy calibration	61
4.2	Calibration scheme used in the GRH	63
4.2.1	Principle of the method	63
4.2.2	Application to GRH	65
4.2.3	Error estimation	68
4.3	Map formation	70
C	Appendix	78
C.1	One-dimensional transform	78

5	One-dimensional observations	80
5.1	Introduction	80
5.2	Observations of SVC at meter-decameter wavelengths	81
5.3	Observations with the GRH	84
5.4	Discussions and Conclusions	94
6	'Quiet Sun' at meter-decameter wavelengths	102
6.1	Introduction	102
6.2	Thermal emission from the 'quiet' Sun	104
6.2.1	Scattering	108
6.2.2	Coronal streamers	112
6.2.3	Coronal holes	113
6.2.4	Other possibilities	114
6.3	Observations with the GRH	115
6.4	Discussions and Conclusions	118
7	Radio signatures of Coronal Mass Ejections	134
7.1	Introduction	134
7.2	CME event of April 13, 1997 and its association with radio noise storm	135
7.2.1	Observations	137
7.2.2	Discussions and Conclusions	143
7.3	CME event of September 23, 1997 and its association with Coronal holes, Type radio III bursts	144
7.3.1	Observations	145
7.3.2	Discussion and Conclusions	146
7.4	CME event of October 24, 1997 and mass estimation	150
7.4.1	Observations	151

7.4.2	Mass estimation	152
8	Summary and comments	162
9	Bibliography	164

Chapter 1

Introduction

The Sun is of interest to astronomers for many reasons. It is the only star which can be observed at relatively close quarters; its atmosphere provides an example of a fully ionized plasma in which the generation and propagation of radio waves and other phenomena such as shock waves may be studied. The active Sun and in particular the CMEs and solar flares, have a profound influence on the near-earth environment and the interplanetary medium. For example, the release of energetic particles during a CME or a flare causes communication blackouts. The increasing activity in space science is primarily concentrated on regions intimately coupled to the Sun, the interplanetary medium and the atmospheres of planets.

In the recent years a radical change has taken place in the methods used to study the Sun; the entire electromagnetic spectrum from x-rays to radio frequencies is now available for observations. As a result, we have been able to study the Sun's atmosphere in far greater detail than before, and hence observe a wide range of new phenomena not observable in the visible portion of the electromagnetic spectrum. As far as the radio method of investigating the Sun is concerned, it started with the discovery by Hey in 1942 of the

Sun's radio emission. Since then, discoveries on the nature of the radio Sun followed in quick succession. The results that came out called for further observations with improved techniques. Like any other field of research, each new technique in solar radio astronomy produced new results which, in turn, suggested the next technical advance required.

The first and still today the most common instrument to be used in solar radio astronomy is a single dish telescope. Measurements of the brightness temperature of the Sun with such instruments have resulted in the interpretation of meterwave emission as originating from the corona and the centimeter wave emission from the chromosphere. They have also indicated that most radio bursts are of nonthermal nature. The introduction of the one-dimensional grating (or multi-element) interferometers in the early 1950's significantly advanced the technique of studying the "quiet" Sun and the slowly varying component (SVC) on daily basis. However, in order to study the emission from the localised regions on the Sun, such as the radio bursts, coronal condensations, etc., one requires two-dimensional mapping of the Sun. This led to the construction of a radioheliograph at Culgoora in Australia in the middle of the 1960's (Wild et al. 1967). Although this instrument produced instantaneous pictures of the Sun in two opposite senses of circular polarisation, it mainly contributed to the study of the radio emission from active Sun. Also it was primarily operated at only one frequency (80 MHz) throughout most of its lifetime. Since the characteristics of the sources of solar activity differ considerably at different frequencies, it is necessary to produce instantaneous two-dimensional solar images simultaneously at several frequencies so that the physical nature of the centers of activity at different layers of the Sun could be properly understood. The first multifrequency radioheliograph came into operation in the early 1980's at the Clark Lake

Radio Observatory in U.S.A. (Kundu et al. 1983). This instrument which routinely produced two-dimensional pictures of the outer solar corona in the frequency range 20-120 MHz, provided a wealth of data on both the quiet as well as the active Sun during the period 1980-1985. But ever since the decommissioning of Culgoora and Clark Lake instruments, there has been no other radioheliograph for regular observations of the Sun at meter-decameter wavelengths. With the Nobeyama and the Nancay radioheliographs presently carrying out regular observations of the Sun at centimeter and decimeter-meter wavelength ranges respectively, a dedicated radioheliograph for mapping the Sun at meter-decameter wavelengths can play a major role in the study of emission from the outer solar corona. Also, a multi-wavelength study using data obtained with various ground based instruments and those on board space missions like YOHKOH, WIND, SOHO, ULYSSES, etc. is expected to provide new insights into the Sun.

The Indian Institute of Astrophysics (IIA) has recently completed construction of a new radioheliograph for dedicated observations of the Sun in the frequency range 40-150 MHz, at the Gauribidanur radio observatory (Lat: 13°36'12" N and Long: 77°27'07" E), 80 kms north of Bangalore. This instrument which can map the solar corona at various heights ($\approx 0.1-0.6 R_{\odot}$) above the photosphere, has been in regular operation since April, 1997 onwards.

I joined the solar radio astronomy group at the IIA during the middle of 1992. To begin with, I was assigned the task of testing various aspects of the antenna system and the R.F. cable network. A 2-channel analog receiver was used to test the amplitude and phase stability of the open-wire line system which was used for transmitting the antenna signals to the receiver building. The details of the antenna system and other R.F. hardware used in the GRH

are given in Chapter 2. From the middle of 1994, one dimensional observations were carried out with the E-W arm of the heliograph and a 64-channel digital receiver. These observations were mainly meant for an understanding of various aspects of the digital receiver system, in addition to studying the one-dimensional equatorial brightness distribution of the Sun. With the experience gained, a 1024 channel digital receiver for correlating the signals from all the 32 antenna groups in the heliograph, was built. Chapter 3 gives a description of the various aspects of the digital receiver system used with the GRH.

It is well known that the complex visibilities observed with any radio interferometer array are generally corrupted due to instrumental and propagation errors. Though many calibration schemes are in use at present for correcting the various errors in the observed parameters, their application to an extended and a highly dynamic source like Sun is dubious. So it was decided to develop a calibration scheme that can be specifically used for correcting the observed quantities in T-shaped interferometer array like the GRH. The details of this scheme are described in Chapter 4.

In Chapter 5, the results of the one-dimensional observations made using the 64-channel digital receiver and the E-W arm of the heliograph are presented. It is shown that from a study of the movement of persistent, localised sources on the solar disk, it is possible to estimate the electron density of the solar corona, at a particular height above the photosphere, independent of any models.

One of the intriguing problems in the meter-decameter wavelength radio observations of the emission from the undisturbed solar corona, is the cause for low values of the observed brightness temperature, i.e. $T_b < 10^6$ K. Though many theories invoking, (1) scattering by density inhomogeneities

and (2) refraction effects due to the presence of high density regions, have been put forward, none of them give a satisfactory explanation. In Chapter 6, some of these have been reviewed in the light of new observational results from the GRH.

Yet another topic, in the field of solar physics in general, which has been baffling various people working in this field, is the onset of a CME. Till date, neither the origin of a CME nor its energy release mechanism is properly understood. The radio observations play an important role in the study of the CMEs, since (1) they can image the solar corona against the disk unlike a white light coronagraph. By observing CMEs against the disk, they can be detected early in their development and directly associated with the underlying photospheric features; (2) they are sensitive to a broad range of temperature, from chromospheric to coronal, by virtue of the $T^{-1/2}$ dependence of the thermal free-free emissivity. Though the disk features can be imaged in soft x-rays (SXR) also, they are insensitive to sub-coronal temperatures; (3) unlike the SXR and white light images, they are sensitive to the nonthermal emission due to the radio bursts that accompany the CMEs and (4) they can be made with ground based instruments. Though the GRH is operated as a transit instrument at present, on many occasions, it was possible to map coronal features prior to and in the aftermath of the CME events. The results of some of these observations made with the GRH are described in Chapter 7. In Chapter 8, a summary of the results of my thesis work is presented.

Chapter 2

Antenna system

2.1 Introduction

The Gauribidanur radioheliograph is a T-shaped interferometer array, with the long arm (1280 m) in the E-W direction and the short arm (441 m) along the South direction. The co-ordinates of the array, referred to the mid-point of the E-W arm are, Lat: $13^{\circ}36'12''$ N and Long: $77^{\circ}27'07''$ E. As the main purpose of the construction of this instrument is to obtain maps of the outer solar corona at several frequencies, it was decided to use an antenna that provides an almost continuous coverage over a wide range of frequencies, i.e., a frequency independent antenna as the basic receiving element. The conventional dipole antennas, which have a simple design, are essentially resonant structures with their important properties like input impedance, radiation pattern, directive gain, beamwidth, etc., going through maximum and minimum values at particular frequencies. The performance of a dipole antenna w.r.t. the above electrical properties is mainly characterized by its dimensions (*characteristic lengths*) measured in wavelengths (Weeks, 1968). This implies that conventional dipole antennas are inherently frequency-dependant.

The structural feature required for frequency-independent operation is the absence of characteristic lengths (Rumsey, 1966). One of the important class of frequency independent antennas is the Log Periodic Dipole antenna, where bandwidths of 10:1 or more can be achieved by careful designing. The frequencies at which the antenna performance will be identical are related by the equation,

$$f_n = f_{n+1} k \quad (2.1)$$

i.e.,

$$\log(f_{n+1}) = \log(f_n) + \log(1/k) \quad (2.2)$$

where k is a constant. From the above equation, one can see that the performance is a periodic function of the logarithm of the frequency, hence the name, log periodic dipole (LPD).

2.2 Antenna parameters

Figure 2.1 shows the structure of the LPD used in the GRH. It consists of a number of dipoles of different lengths and spacing and is fed at the small end of the structure using a co-axial cable. The maximum radiation is towards this end. The LPD is made of aluminium tubes and has an effective collecting area (A_e) of $0.5 \lambda^2$. It has been designed to operate in the frequency range of 40-150 MHz with a characteristic impedance (Z_o) of 50Ω , VSWR < 2 and a directional gain of 8 dB. The dimensions of the individual dipoles and the spacing between them are given in Table 2.1. One can see that the length (l) of the dipoles and their spacing (s) are graduated in such a way that,

$$\frac{l_{n+1}}{l_n} = \frac{s_{n+1}}{s_n} = k \quad (2.3)$$

where k is the same constant in the equation 2.1. The periodic variation of the electrical properties of the LPD is the result of these structural conditions.

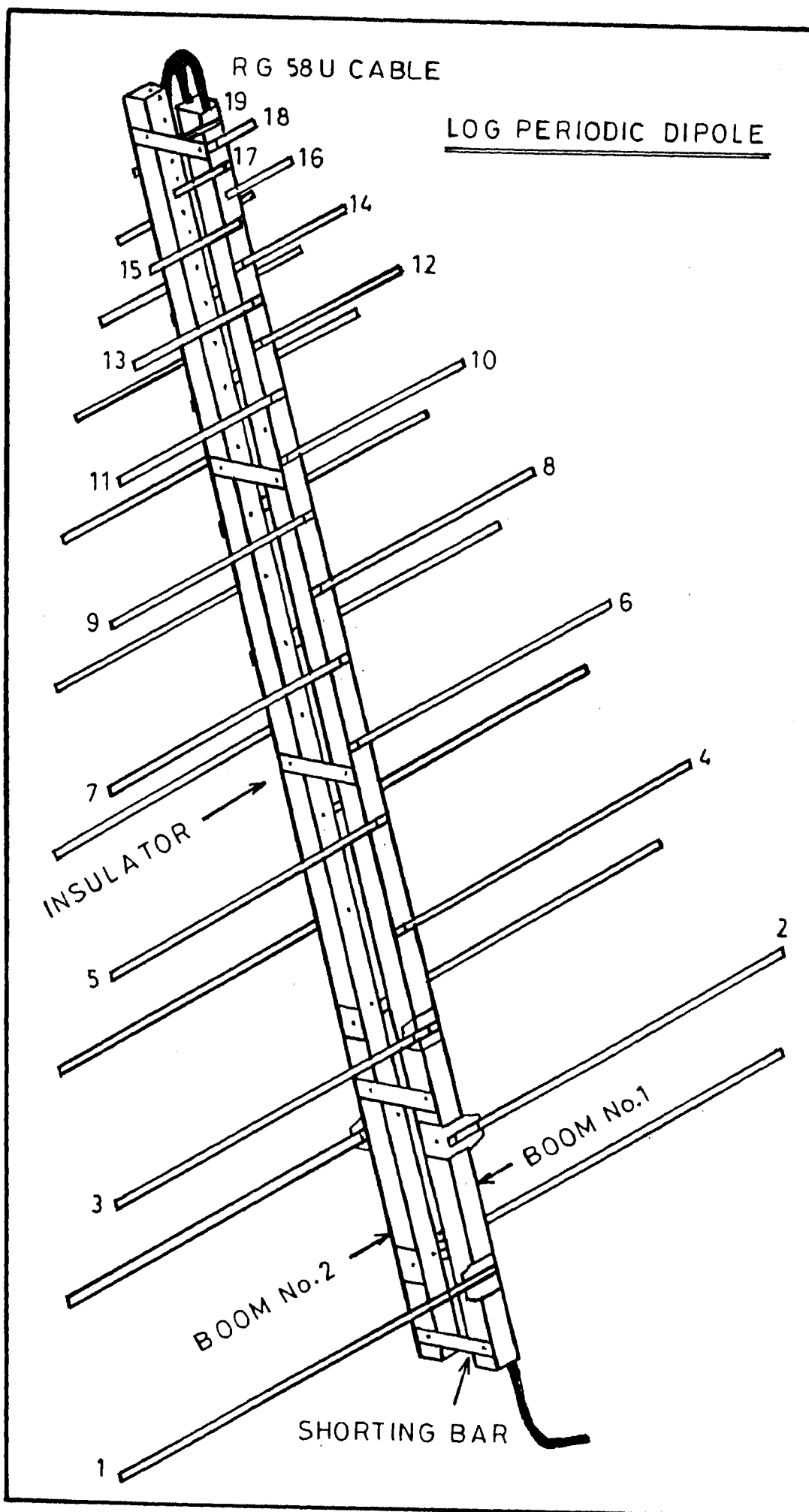


Fig.2.1 Log periodic dipole used in the Gauribidanur Radio Heliograph.

Dipole number	Length (in cm)	Dipole numbers	Spacing (in cm)
1	275	1 & 2	54.8
2	245	2 & 3	48.7
3	218.5	3 & 4	43.4
4	194.5	4 & 5	38.6
5	173	5 & 6	34.4
6	154.5	6 & 7	30.6
7	137.5	7 & 8	27.2
8	122.5	8 & 9	24.2
9	109	9 & 10	21.6
10	97	10 & 11	19.2
11	87	11 & 12	17.1
12	77	12 & 13	15.2
13	68.5	13 & 14	13.8
14	62	14 & 15	12
15	55	15 & 16	10.7
16	49	16 & 17	9.5
17	44	17 & 18	8.5
18	39	18 & 19	7.6
19	35	19 & top	6.7

Table - 2.1

Figure 2.2 shows the VSWR of one of LPD used in the GRH. One important point to be noted here is that the LPD is a balanced device, i.e. the two conductors are at equal and opposite voltages w.r.t. the ground. On the other hand, a co-axial cable is an unbalanced device and so, a balanced-to-unbalanced (BALUN) transformer is necessary to connect them. In the case

of the LPD, a co-axial cable is run through the boom and the connection acts like a BALUN transformer (Appendix A.1).

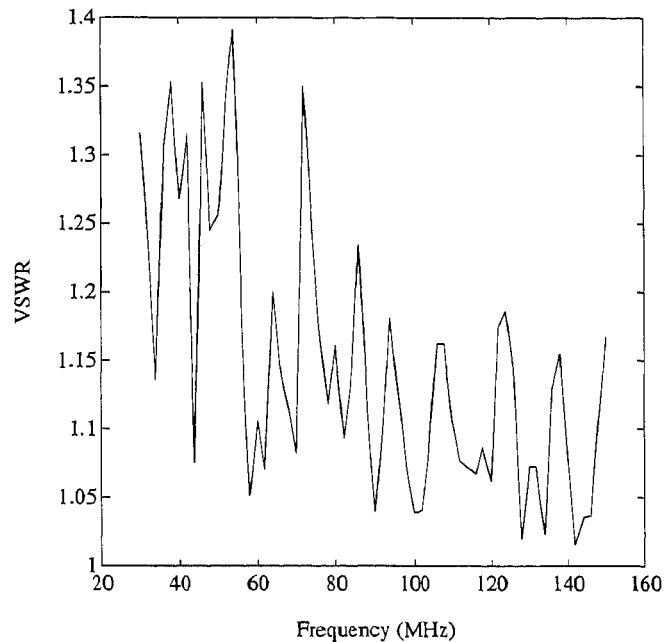


Figure 2.2: VSWR of a Log Periodic Dipole used in the GRH.

Figure 2.3 shows the set-up used to measure the far-field pattern of one of the LPD used in the GRH. A folded dipole of length $\lambda/2$ at 150 MHz was used as the radiating element. Due to space considerations, the LPD under test was kept approximately 480 m away from it. The response pattern of the LPD along the E-plane and H-plane¹ were measured by keeping its orientation parallel and perpendicular to the folded dipole. Figure 2.4 and 2.5 show results of the measurements. The half-power widths are approximately 60° in the E-plane and 100° in the H-plane, which enables observations to be carried out over a wide range of hour angle and declination.

¹E-plane is along the arms of the LPD and H-plane is perpendicular to it.

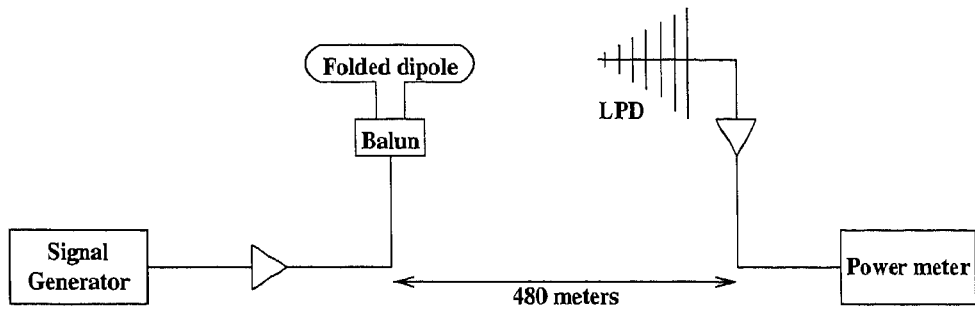


Figure 2.3: Set-up used to measure the far-field radiation pattern of the LPD used in the GRH.

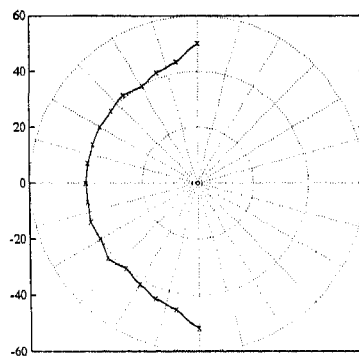


Figure 2.4: Polar plot of the LPD beam pattern in the E-plane.

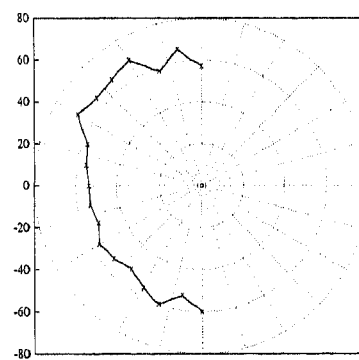


Figure 2.5: Polar plot of the LPD beam pattern in the H-plane.

2.3 Array configuration

The outline of the GRH array is shown in Figure 2.6. The E-W arm has 128 elements separated by 10 m interval except for the elements EW64 and EW65 which are separated by 20 m. The South arm has 64 elements and the first element of the South arm is located at the center of the E-W arm. Because of the limitation in the available space for setting up the array, the elements in the South arm were arranged with an inter-element spacing of 7 m as compared to the 10 m spacing in the E-W arm. This spacing between the individual elements in the E-W and the South arms gives rise to grating lobes along the respective directions, which will be discussed in a later section. All the elements in the array are oriented in the E-W direction and they accept linear polarisation in that direction. The various characteristics of the heliograph are given in Table 2.2.

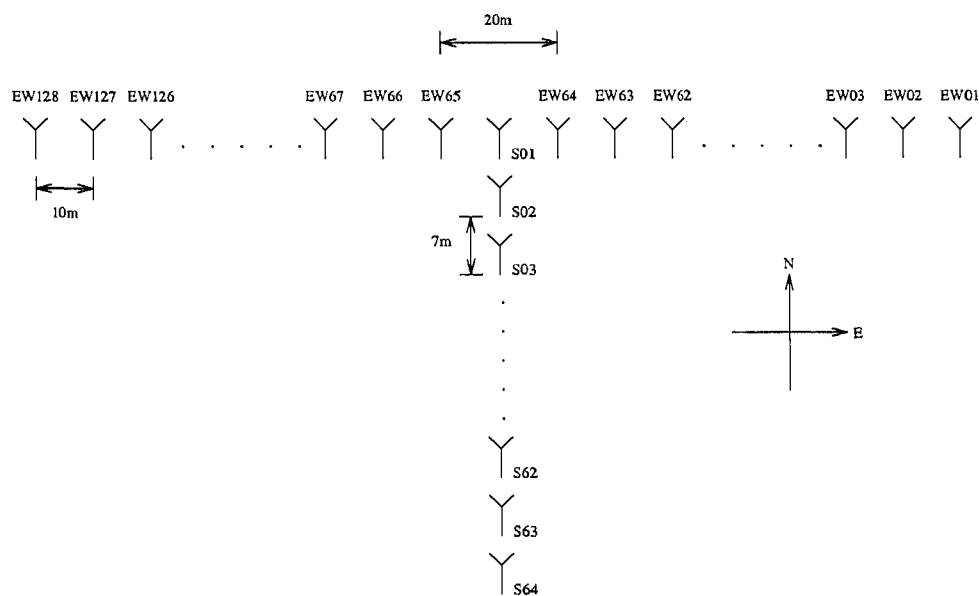


Figure 2.6: Lay-out of the Gauribidanur radioheliograph

Parameter	Value
Basic element	Log periodic dipole
Frequency of operation	40 - 150 MHz
Declination coverage	-31° S to +59° N
Number of antenna groups	32 (16 E-W and 16 South)
Back end receiver	Digital correlator - 1024 channels (1 bit - 2 level)
Effective collecting area	96 λ^2 (total power mode)
Field of view	3° × 4° at 150 MHz
Angular resolution	5' × 8' (R.A. × Dec.) at 150 MHz
I.F. Bandwidth	1 MHz
Sampling Rate	3.6 MHz
Observing period	± 2 hours around local meridian
Sensitivity (5 σ)	$\approx 2 \times 10^{-2}$ sfu at 150 MHz (for 10 sec integration time)

Table - 2.2

2.4 Element grouping

2.4.1 E-W arm

The E-W arm is divided into 16 groups ($G_1, G_2 \dots G_{16}$) of 8 elements each. The signals from the individual elements in a group are combined in a branched feeder system using power combiners and RG8U cables as shown in Figure 2.7. The R.F. signal from each element in a group is passed through a high pass filter which has a cut-off frequency of 50 MHz and then amplified approximately 30 dB in a wide band amplifier (0.5 to 500 MHz). The high

pass filter is used to cut off large interfering signals at frequencies < 40 MHz, which otherwise can give rise to spurious intermodulation products. In addition it also reduces the dynamic range requirements of the subsequent stages of electronics. The insertion loss in the filter is ≈ 1 dB and the loss over its pass band is < 1 dB. After accounting for the loss in the cable ahead of the filter (≈ 1.5 dB at 150 MHz) and the noise figure of the amplifier (≈ 3 dB), the total receiver noise temperature at 150 MHz is about 600 K. At this frequency the sky noise is about 300 K. Therefore the system temperature T_{sys} is, $T_{sky} + T_{rcvr} = 900$ K.

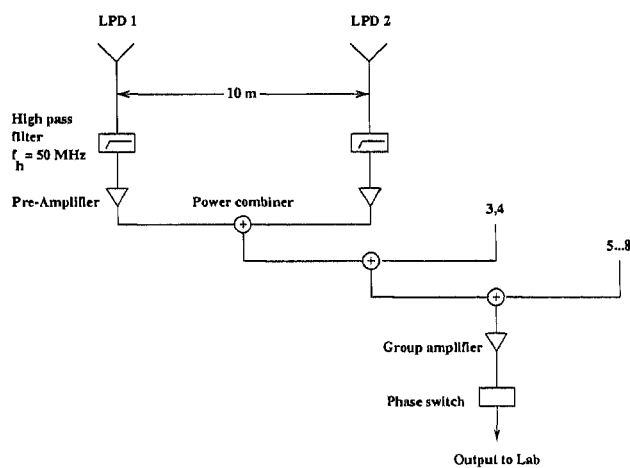


Figure 2.7: One of the 16 groups in the East-West arm

All the groups are equally spaced with the spacing between the phase centers of the adjacent groups being 80 m except for the groups G_8 and G_9 whose phase centers are separated by 90 m. This is due to the 20 m spacing between the antennas EW64 and EW65 as mentioned in the earlier section. It should be noted that all the elements in the E-W arm are not at the same height due to the uneven terrain on which the array is set-up. But within each group, all the antennas are at same height. The height differences can be treated as

phase errors if the region to be mapped is small (Thompson, Moran and Swenson, 1986). The phase error is approximately,

$$\pi(\theta_f/2)^2\theta_b^{-1} \quad (2.4)$$

where θ_f is the width of the synthesized field. The term θ_b is given by λ/h , where λ is the wavelength of observation and h is the height difference. The condition that no phase errors can exceed, say 0.1 radians then requires that,

$$\theta_f < \frac{1}{3}\sqrt{\theta_b} \quad (2.5)$$

In the case of GRH, we are interested in mapping only the Sun, whose size is approximately $0.6^\circ \times 0.6^\circ$ around 150 MHz. This implies that even at the highest frequency of operation with the GRH (150 MHz), the condition in equation (2.5) is satisfied. Therefore, the errors due to the height differences can be corrected during calibration. Table 2.3 shows the height difference among the various groups in the E-W arm w.r.t. the groups in the South arm which are at the same height. The -ve sign implies that the antenna groups are at a lower height compared to those in the South arm.

Group number	Height difference	Group Number	Height difference
1	-2 m	9	0
2	-2 m	10	0
3	-1.5 m	11	-2 m
4	0	12	-3.75 m
5	0	13	-3.75 m
6	0	14	-3.75 m
7	0	15	-3 m
8	0	16	-1.75 m

Table - 2.3

2.4.2 South arm

The South arm is also divided into 16 groups ($G_{17}, G_{18} \dots G_{32}$) but with only 4 elements in each group. Filtered and amplified outputs from the four elements of each group are combined using delay shifters, power combiners and cables as shown in Figure 2.8. The phase centers of the adjacent groups are equally spaced with an interval of 28 m. Delay shifters are used for changing the direction of the beam of each group to minimise coherence loss (see Appendix A.2) when receiving signals from larger zenith angles. A computer-controlled system provides the switching signals for the insertion of the required delay in the signal path.

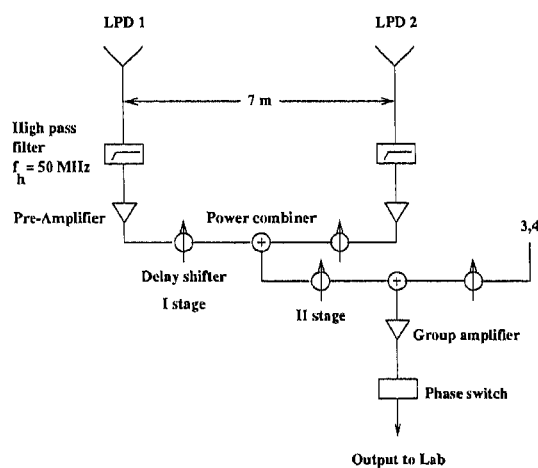


Figure 2.8: One of the 16 groups in the South arm

2.5 Signal transmission to the receiver building

The output from each of the 32 groups is amplified approximately by 34 dB in a wide band amplifier and passed through an electronic switch which periodically inverts the phase of the input signal under the control of the switching

signal sent from the central receiver building. This switching scheme helps in minimising the possible coupling between the adjacent open-wire transmission lines, when the signals are multiplied (see Chapter 3 for the details). The switches have a typical insertion loss of about 4 dB. The isolation between the input and output is about 30 dB. Figure 2.9 shows the schematic of the electronic switch. If the control signal is +ve, the diodes D1 and D2 will be forward biased and the signal flows through them. On the other hand, if the control signal is -ve, then the signal flows through D3 and D4. This action can be viewed as modulating as the input R.F. signal by a square wave that alternates between high and low states or 0° and 180° . After switching, the R.F. signal is sent to the receiver room via open wire transmission lines due to cost considerations and also low attenuation (0.5 dB/100 m at 150 MHz). BALUN transformers are used to connect the R.F. signal at both ends of the open-wire line. Since broad band (40-150 MHz) BALUN transformers were not commercially available, we use transformers designed in our observatory. The measured VSWR of the transformers is ≈ 1.5 at 120 MHz.

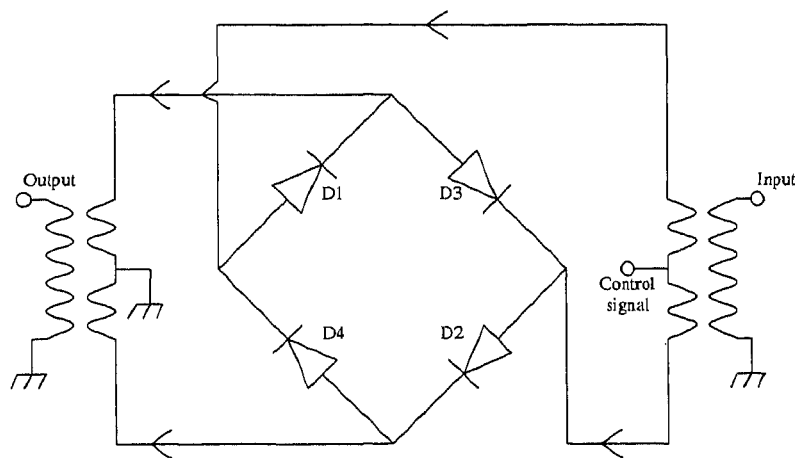


Figure 2.9: Schematic of the electronic switch used in the GRH

2.6 Grating lobes

Due to the array configuration of the GRH, there are grating responses of the *group beam* and the *synthesized beam*. While the former is due to the spacing between the individual antennas within each group, the latter is due to the spacing between the phase centers of adjacent groups. There can be confusion in interpreting the observed data if both the primary and grating responses happen to lie within the same source. Also there is the possibility of contribution from two different sources at the same time, through the primary and the grating responses. The angular separation between the primary response and the first grating response is (Kraus, 1966),

$$\phi_g = \sin^{-1} \left(\frac{\lambda}{d} \right) \quad (2.6)$$

where d is the distance between the phase centers of the individual antennas or group of antennas depending on the case and λ is the wavelength of observation. The angular separation between the adjacent grating lobes is also the same as above. In the case of the GRH, at the highest operating frequency² (150 MHz), the grating responses of the group beam are away from the primary response by approximately 12° and 17° in the E-W and N-S directions (Figures 2.10 and 2.11). Since the angular size of the Sun at 150 MHz is only $\approx 0.6^\circ$, the possibility of both the primary and grating responses receiving radiation from the Sun at the same time can be ruled out. There can be confusion while interpreting the observed data when some other radio source is present at the location of one of the grating responses, in the case of one-dimensional observations. When we correlate the output of each group

²The angular separation between the grating and primary responses decreases with increase in frequency. Therefore any confusion due to the presence of grating responses should be more pronounced at higher frequencies.

in the E-W arm with that in the South arm, bandwidth effects would reduce the coherence of the radiation at the position of these grating lobes, as the compensating delays in the South arm are introduced for a particular right ascension and declination. Though the grating responses in Figures 2.10 and 2.11 are shown to have the same amplitude³ as the primary response, in practice their amplitudes will be lesser since they will be modulated by the beam of a single LPD (Figures 2.4 and 2.5).

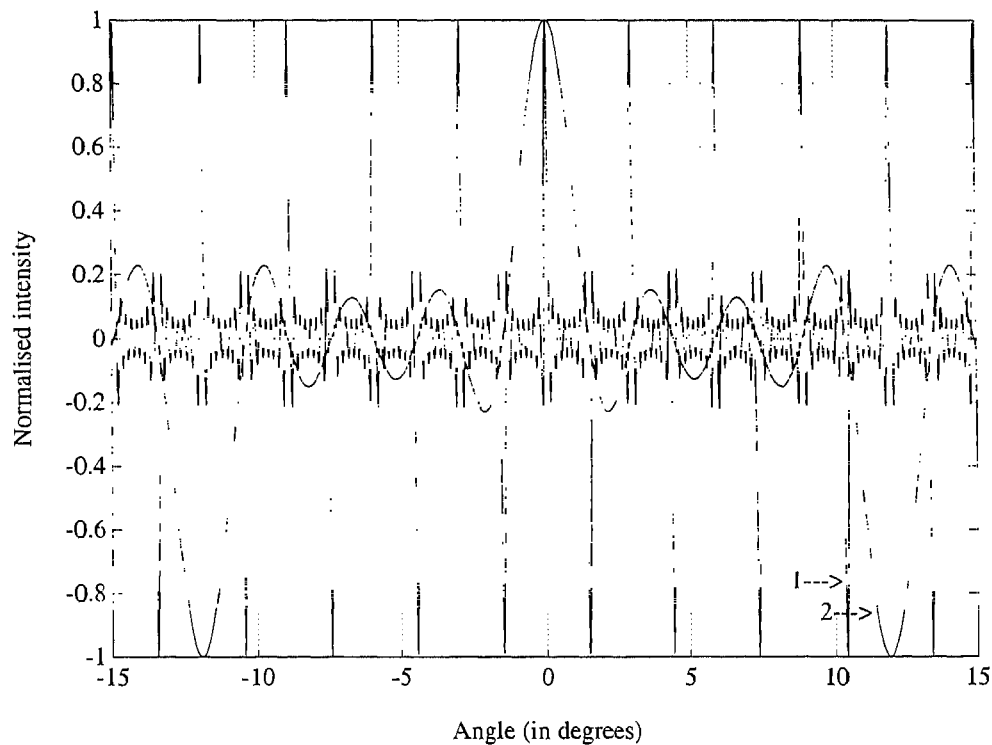


Figure 2.10: Theoretical beam patterns of the E-W arm of the GRH at 150 MHz, (1) E-W array synthesized beam and (2) E-W group beam.

³Since the peak of the sine function alternates between +1 and -1, some of the grating responses have negative amplitude.

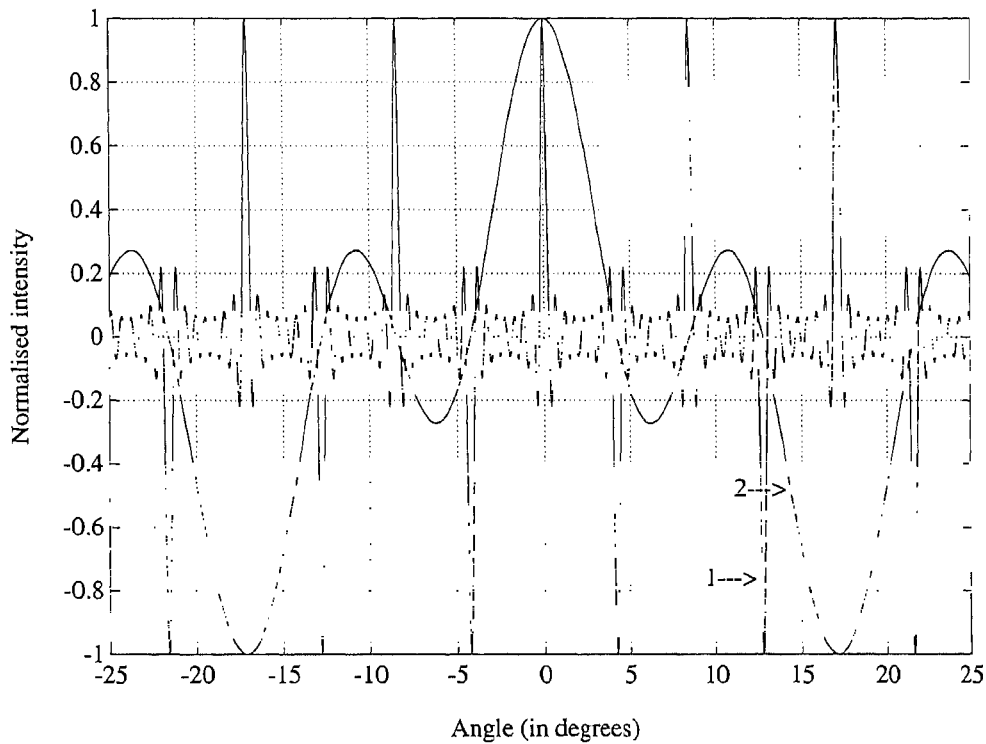


Figure 2.11: Theoretical beam patterns of the South arm of the GRH at 150 MHz, (1) South array synthesized beam and (2) South group beam.

2.7 Delay shifters

In arrays like the GRH where the antennas are fixed in the vertical direction, the only way to change the pointing of the primary beam of each group is by introducing phase gradients. This can be achieved by phase rotating the output of each element within a group, but in the case of arrays like the GRH operated over a wide range of frequencies, one has to use real time delays. In addition, delays have to be introduced at each group output depending on the source position in the sky and the receiver bandwidth. Since the GRH is being operated in the transit mode at present, the beam of each group has to

be steered only along the declination. To accomplish this, delays are introduced at two stages (I stage and II stage) between the elements in each group of the South arm⁴, as the individual elements within the group are combined in a branched feeder system (see Figure 2.8). It was decided to have several sections in each stage, with each section or combination of different sections enabling the beam to be steered by a particular angle in the sky. Table 2.4 gives the details of the delay shifters used in the South arm of the GRH.

Stage	Spacing	Number of Sections	Tilt angle for each section	Step interval
I	7 m	3	8°, 16° & 32°	8°
II	14 m	4	4°, 8°, 16° & 32°	4°

Table - 2.4

The step intervals were chosen to be 8° & 4° in the I and II stages, since the maximum value of the coherence loss due to any delay error will be only 1.7% which can be neglected. It must be noted that apart from the number of sections (in each stage) mentioned in Table 2.4, there is one additional section in both the I and II stage delay shifter units. Since the delays in each section mentioned in Table 2.4 help in steering the beam to only one side of the zenith, this additional section, when used independently or in combination with the other sections in that stage, helps in steering the beam to the other side of the zenith also.

The controlling of the various sections in each stage is accomplished through R.F. diode switches which are driven by a set of 18 control signals (8 for the I stage and 10 for the II stage) transmitted from the receiver building. Figure 2.12 shows one section of the delay shifter unit used in the

⁴The response function of each group in the E-W arm is very broad in declination.

GRH. The R.F. signal, depending on the polarity of the control voltage (V) flows through either the delay path (where a cable of length corresponding to the particular delay is present) or the straight path. The delay/straight path in different sections are enabled depending on the declination of the source.

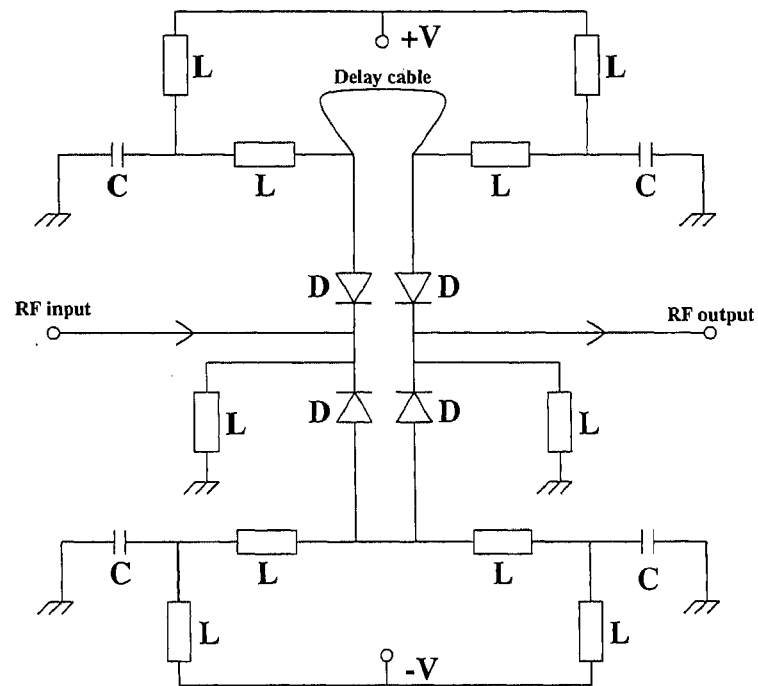


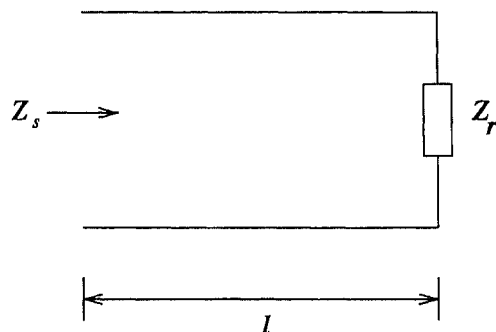
Figure 2.12: A section of the delay shifter unit used in the GRH. In the above figure: C - capacitance, L - inductance, D - diode, V - control voltage.

Appendix A

Appendix

A.1 BALUN transformer

A.1.1 Quarter-wave ($\lambda/4$) transmission line



Consider a transmission line section of length l as shown in the figure. If the line is lossless, then its characteristic impedance Z_o will be purely resistive. For any impedance termination Z_r , the input impedance is given by,

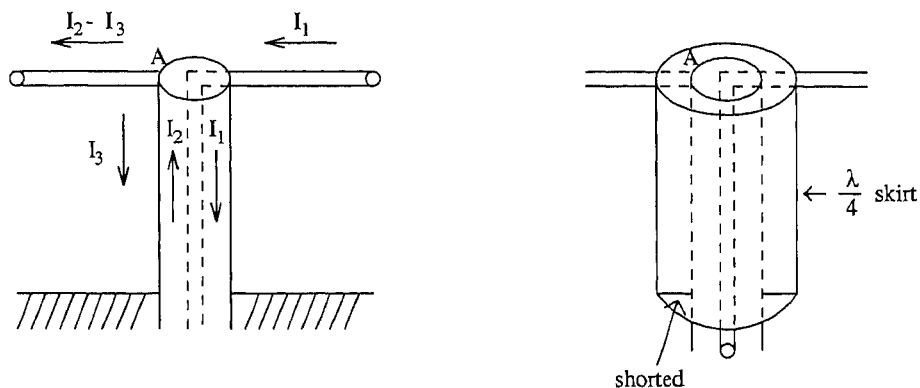
$$Z_s = Z_r \left(\frac{\cos\beta l + jZ_o/Z_r \sin\beta l}{\cos\beta l + jZ_r/Z_o \sin\beta l} \right) \quad (\text{A.1})$$

where $\beta = 2\pi/\lambda$. If $l = \lambda/4$, then $\beta l = \pi/2$. Therefore,

$$Z_s = Z_o^2/Z_r \quad (\text{A.2})$$

The input impedance of a quarter-wave line becomes infinite, if its other end is shorted, i.e. $Z_r = 0$.

A.1.2 Feeding the LPD through a co-axial cable



The LPD is a balanced device in the sense that for equal currents in the two arms of any of the dipole, the arms should have same impedance to the ground. Such a load cannot be directly connected to a co-axial cable as shown in the first half of the above figure, since a co-axial cable is an unbalanced device. In a balanced device, the currents I_1 and I_2 in the two arms should be equal and opposite. But in this case, at the junction A, the current I_2 divides into I_3 , which flows down the outside of the outer conductor and $I_2 - I_3$ which flows on the second arm of the dipole. To avoid this current imbalance between the two arms of the dipole, the amplitude of I_3 should be minimised. The current I_3 depends on the effective impedance of the path outside the conductor. This impedance is usually made high by the addition of a quarter-wave skirt around the outer conductor as shown in second half of the figure. With the skirt shorted to the conductor at the bottom, the impedance between points A and the ground is extremely large, thus making I_3 small. In the case of the LPD's in the GRH, since the co-axial cable

connected to the feed point at the top is run through one of the booms, the connection acts like a quarter-wave skirt, thereby minimising the imbalance. As one can see from the VSWR of the LPD in Figure 2.2, the impedance matching is good over a wide range of frequencies.

A.2 Coherence loss

The output of a correlation interferometer is given by (Thompson, Moran and Swenson, 1986),

$$F = \cos\left(\frac{2\pi D\varepsilon\nu}{c}\right) \quad (\text{A.3})$$

where D is the baseline length, $\varepsilon = \sin\theta$ is the direction cosine measured w.r.t. to the baseline, ν is the frequency of observation and θ is the angle between the wavefront and the normal to the baseline. The above expression is true only if the observing frequency is strictly monochromatic. But in general the received signals are averaged over a band of width $\Delta\nu$ (generally assumed to be rectangular) centered around a frequency ν_{rf} . So, the above equation becomes,

$$F(\nu_{rf}) = \frac{1}{\Delta\nu} \int_{\nu_{rf}-\Delta\nu/2}^{\nu_{rf}+\Delta\nu/2} \cos\left(\frac{2\pi D\varepsilon\nu}{c}\right) d\nu \quad (\text{A.4})$$

$$= \cos\left(\frac{2\pi D\varepsilon\nu_{rf}}{c}\right) \frac{\sin(\pi D\varepsilon\Delta\nu/c)}{\pi D\varepsilon\Delta\nu/c} \quad (\text{A.5})$$

Thus the output is modulated by a sinc function envelope which will be maximum only if the delay ($\tau = D\varepsilon/c$) between the two signals at the correlator input is zero. If the delay between the signals are not compensated before correlation, it will lead to a loss in the coherence between the two signals. In the case of GRH, proper delays are introduced at the required stages to minimise this loss. The modulating function in equation (A.5) is also called the *bandwidth decorrelation function* or *fringe washing function*.

Chapter 3

Receiver system

As mentioned in the Chapter 2, the GRH consists of 32 antenna groups and the R.F. signals from these groups are brought to the receiver building via open-wire transmission lines. These signals are then processed separately in carefully matched amplifiers and digital circuits. This chapter describes the various analog and digital hardware used in the front and back end receiver system of the GRH for the processing of the R.F. signals from the field. Also some of the tests carried out to check various aspects of the digital system and their results are presented.

3.1 Front end analog receiver

In the case of GRH, the amplified R.F. signal from each group goes through two frequency conversions. It is first up-converted to an intermediate frequency (I.F.) of 170 MHz by mixing with a local oscillator (hereafter referred to as the 1st L.O.) signal. This conversion places all the image frequencies well above the frequency range (40-150 MHz) of observation. Multi-frequency operation is achieved by switching the 1st L.O. to different frequencies in the

range 210 to 320 MHz. The I.F. signal is then passed through a bandpass filter with a center frequency (f_c) of 170 MHz and a bandwidth (Δf) of 6 MHz. This filtering operation helps in suppressing the image frequencies as well as any possible inter-modulation products. After further amplification, the signal is down-converted to a 2nd I.F. of 10.7 MHz by mixing with a 2nd L.O. of 180.7 MHz. The output is again amplified and passed through a band pass filter with a f_c of 10.7 MHz and a Δf of 1 MHz. The narrow value of the bandwidth helps in carrying out interference free observations. The I.F. signals from each of the 32 antenna groups are split into in-phase (cosine) and quadrature (sine) components by passing them through analog quadrature hybrids and then fed to the digital back end receiver. Figure 3.1 shows the schematic of one of the front end receiver used in the GRH.

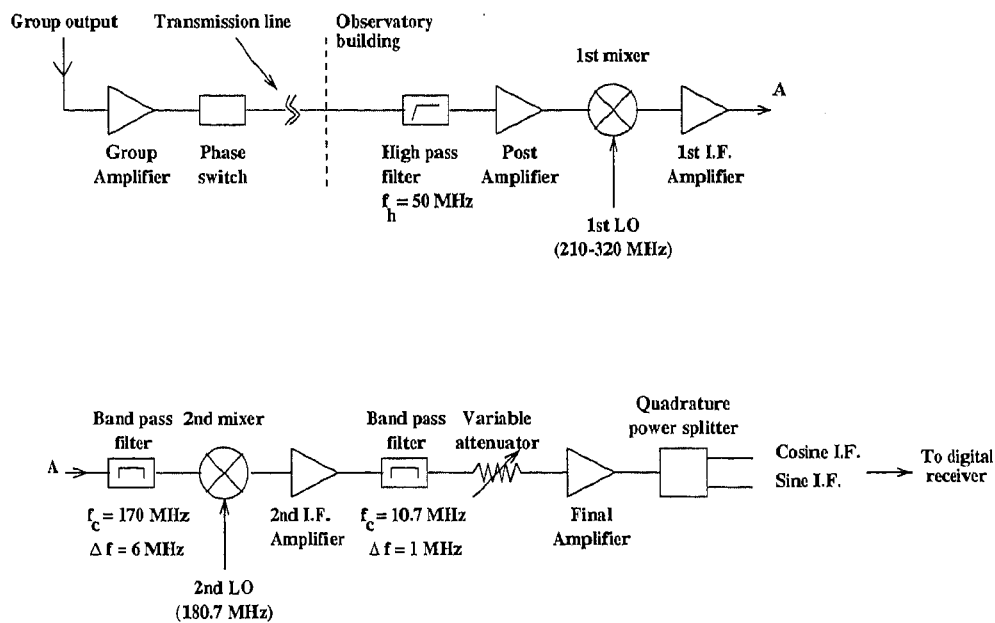


Figure 3.1: Schematic diagram of one of the front end receiver used in the GRH.

3.2 Back end digital receiver

In the GRH, correlations are measured for all the interferometer pairs formed by the 32 antenna groups. These measurements are made using one-bit correlators which can be assembled with simple digital logic, and yields greater stability to the backend than the analog correlator. But the use of one-bit correlator results in a loss of the amplitude information of the input signal (see Appendix B.1) as well a reduction in the sensitivity ($\approx 64\%$) compared to the analog case (Van Vleck and Middleton, 1966). In the case of solar observations, the received signal is so strong that this loss of sensitivity is not severe (Nakajima et al. 1993). In order to obtain all possible multiplications between the 32 antenna groups, i.e. $\frac{n(n-1)}{2} = 512$ complex correlations, a 1024 channel digital correlator is used. Figure 3.2 shows the layout of the multiplication scheme.

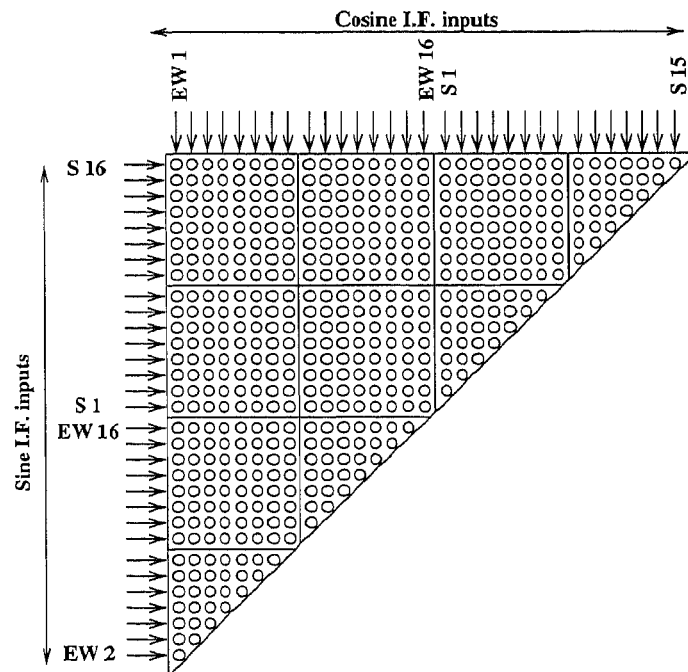


Figure 3.2: Lay-out of the 1024 channel digital correlator system

The signals from the I.F. amplifiers are first quantised to two levels using a zero cross detector. The quantised signals are sampled at a rate of 3.6 MHz and then passed through a delay¹ unit. The delays are implemented using shift registers (Figure 3.3) in which the outputs are tapped at suitable points according to the required value.

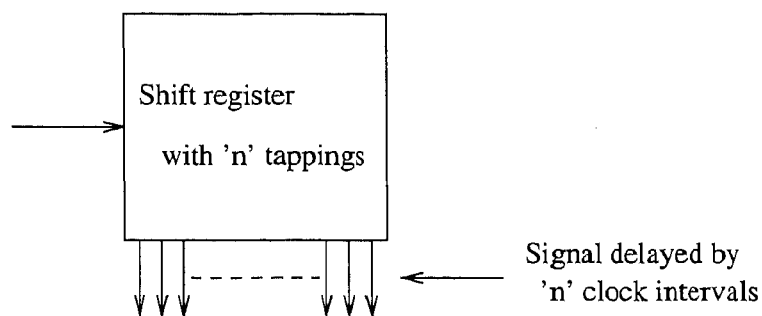


Figure 3.3: Delay unit

The use of digital delays implies that the time delay can be changed only in discrete steps. In the case of GRH, the maximum delay error corresponding to a sampling rate of 3.6 MHz is about 139 nsec. This causes a coherence loss of $\approx 3\%$ for a 1 MHz bandwidth. Though a sampling rate of 3.6 MHz minimises the coherence loss in the present case, it reduces the effective signal bandwidth to 600 KHz, since its 3rd harmonic (10.8 MHz) falls inside the I.F. band which extends from 10.2 MHz to 11.2 MHz.

3.2.1 Walsh switching

The open wire transmission lines carrying R.F. signal from each antenna group are well separated. The I.F. cables and A/D convertors are carefully

¹For observations away from the zenith with relatively large bandwidths, it is necessary to delay the signals appropriately before correlation in order to preserve coherence.

shielded. In spite of these precautions it was found that there is a certain amount of cross-talk between the individual signal channels. Assuming that most of the crosstalk occurs between the signals flowing through the open wire lines, the R.F. output from each antenna group is switched by passing it through an electronic switch which is controlled by the Walsh function signals sent from the receiver building. These switches are kept in the field immediately after the group amplifier. In the case of the GRH, corresponding to each one of the 32 antenna groups, different Walsh signals are sent from the receiver building to the field. Since the switching period for different group outputs are integral fractions of the integration time, the crosstalk signals get averaged to zero as they are correlated half of the time positively and the other half negatively (Granuland, Thompson and Moran, 1978). This switching sequence is subsequently removed at the output of the sampler (using the same Walsh function), thereby also eliminating any errors due to the DC offsets in the A/D convertors. Figure 3.4 shows the operational details of the switching scheme used in the GRH.

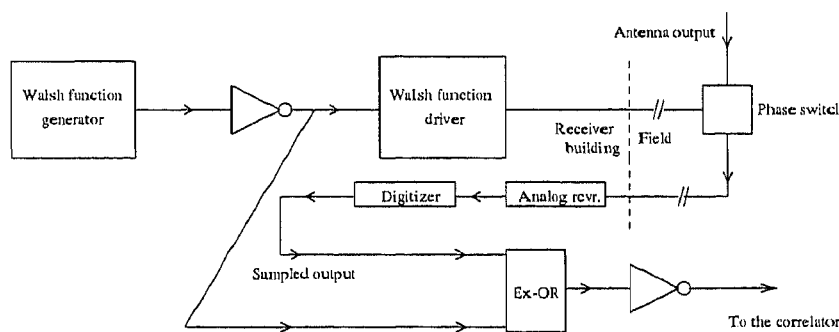


Figure 3.4: Switching scheme used in the GRH

It must be noted that through switching, the unwanted signal will average to zero only if its amplitude is constant over a Walsh cycle, i.e. it should not be a fringe frequency waveform. Otherwise the cross-coupled signals may not

get cancelled accurately. In the case of GRH, the fastest fringe frequency variation is about 21 sec, whereas the largest period amongst the 32 Walsh switching functions is 145 msec, i.e. the integration time used in the receiver system. This will ensure that the unwanted signals will get nearly averaged to zero.

3.2.2 DC offset in the A/D convertor

The DC offset occurs in the comparator, where the input analog signal gets digitized. In the case of GRH where we use a one-bit correlator, the output of the comparator (otherwise called zero crossing detector) is either 1 or 0 depending on whether the input analog signal is above or below the zero level of the comparator. But in practice, the zero level may not be ‘perfect’ as shown in Figure 3.5, i.e. it may have an offset. Because of this, the digitized output from the comparator will be affected and ultimately there will be spurious correlation at the output of the correlator which will limit the dynamic range of the synthesized image (Ekers, 1989). But the effect of this DC offset can be minimised by the use of Walsh switching scheme.

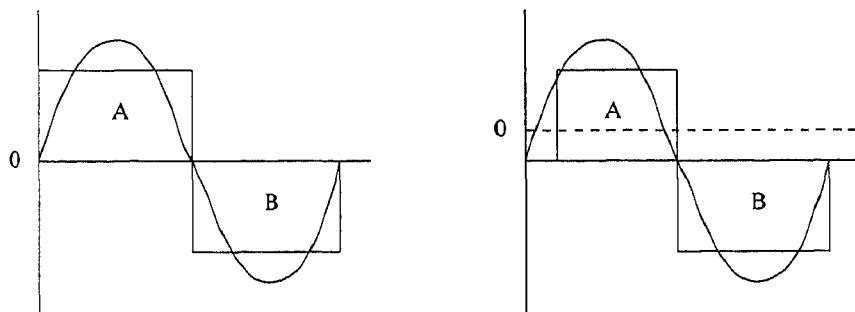


Figure 3.5: DC offset in the A/D convertor

Let S_1 and S_2 which are modulated by Walsh functions f_1 and f_2 be the inputs to comparators 1 and 2 respectively. The output of the two comparators

are given by,

$$S_1 f_1 + DC_1 \quad \text{and} \quad S_2 f_2 + DC_2 \quad (3.1)$$

where DC_1 and DC_2 are the offsets in the comparators 1 and 2 respectively. The comparator outputs are sampled and then demodulated for the Walsh switching action as mentioned earlier. Since different Walsh functions are orthogonal to each other (Thompson, Moran and Swenson, 1986), the demodulated outputs in the two cases are given by,

$$S_1 + DC_1 f_1 \quad \text{and} \quad S_2 + DC_2 f_2 \quad (3.2)$$

These two signals are then fed to the correlator and the output is proportional to,

$$S_1 S_2 \quad (3.3)$$

The terms $S_1 DC_2 f_2$ and $S_2 DC_1 f_1$ will get averaged to zero in the integrator since the inputs (S) are generally Gaussian signals with zero mean and the Walsh functions (f) will have equal number of +ve and -ve periodicities in any one integration period. Thus because of Walsh switching, the unwanted DC terms are not present in the correlator output. The test scheme shown in Figure 3.6 was used in the GRH to test the effectiveness of Walsh switching in removing the DC offset in the comparator. The input to one of the channels was left open (TTL 'High'), while a noise waveform was fed to the other channel. The sampling rate used was 2 MHz and the integration time was 256 msec. The inputs to the correlator are

$$(Noise) f_1 + DC_1 f_1 \quad \text{and} \quad f_2 \quad (3.4)$$

where f_1 and f_2 are the Walsh functions corresponding to the two input channels to the correlator. Since f_1 and f_2 are mutually orthogonal, the

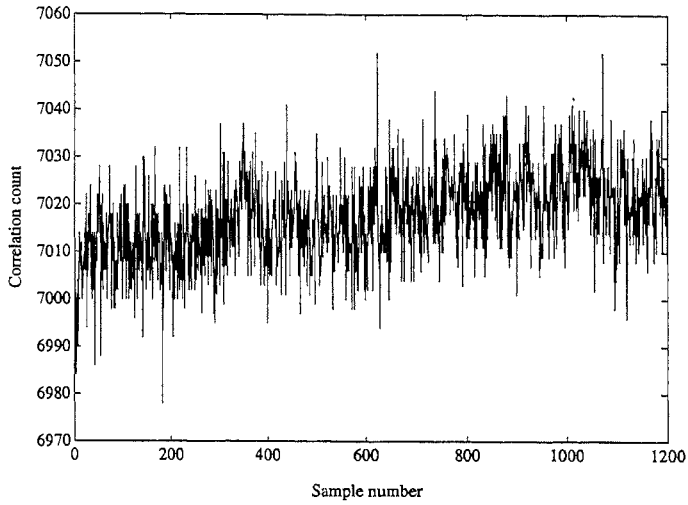


Figure 3.7: Correlator output for comparator DC offset test WITHOUT Walsh switching.

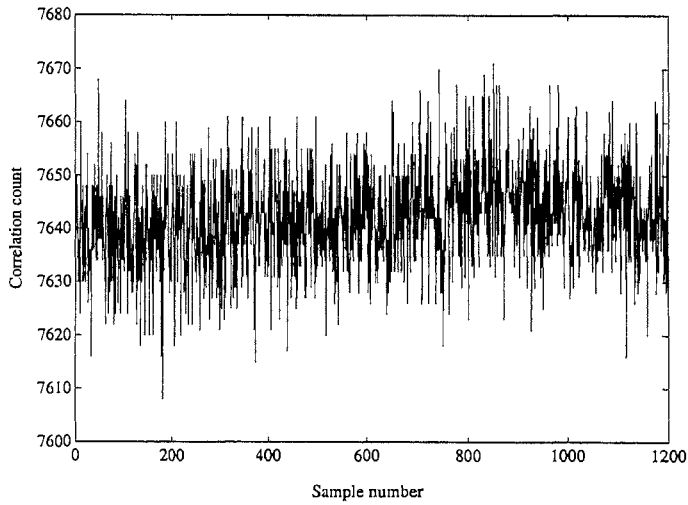


Figure 3.8: Correlator output for comparator DC offset test WITH Walsh switching.

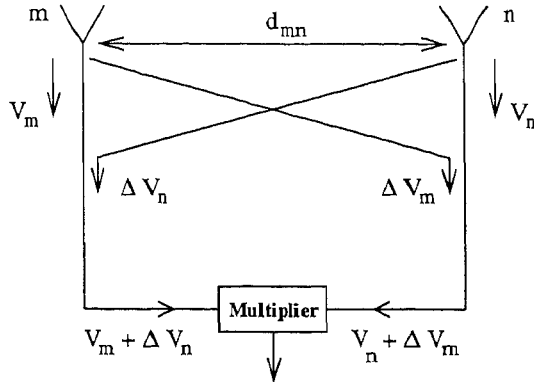


Figure 3.9: Cross-talk in a two element interferometer.

Let

$$V_m = V_n = \sqrt{T_{sys}} \quad \text{and} \quad \Delta V_m = \Delta V_n = \sqrt{\eta T_{sys}} \quad (3.6)$$

where T_{sys} is the system noise and η is the cross-talk between the two antennas in units of power. T_{sys} consists of both the antenna temperature T_s due to the source and the receiver noise T_r . The correlation coefficient due to the cross-talk between the two antennas is given by,

$$\rho_1(d_{mn}) = 2 \frac{\sqrt{\eta T_{sys}} \sqrt{T_{sys}}}{T_{sys}} \quad (3.7)$$

whereas the required correlation coefficient due to the source is,

$$\rho_2(d_{mn}) = \frac{\delta_{mn} T_s}{T_{sys}} \quad (3.8)$$

where δ_{mn} is the amplitude of the Fourier component due to the source. Thus in the presence of cross-talk, an extra term will be present at the output of the correlator. This term if not properly taken care of, will limit the dynamic range of the synthesized image like the DC offset mentioned in the previous section. The phase error due to cross-talk is,

$$\Delta\theta_{mn} = \frac{\rho_1(d_{mn})}{\rho_2(d_{mn})} \quad (3.9)$$

i.e.,

$$\Delta\theta_{mn} = \frac{2\sqrt{\eta} T_{sys}}{\delta_{mn}T_s} \quad (3.10)$$

So, the phase error varies inversely as the amplitude of the Fourier component due to the source. This implies that in the case of observations of extended objects, as the source will get resolved on the longer baselines, the corresponding signal-to-noise (SNR) ratio will be poor and hence the level of cross-talk will be more. The following section illustrates how phase switching using Walsh functions is effective in minimising the effects of cross-talk.

Consider the situation where the output from the two antennas m and n are switched at different rates using Walsh functions which alternate between 0 and 1. Then the input signal to the respective digitizing units will be,

$$V_m f_m + \Delta V_n f_n \quad (3.11)$$

and

$$V_n f_n + \Delta V_m f_m \quad (3.12)$$

When the switching action is removed at the output of the sampler, using the same Walsh functions (Figure 3.4), the input to the correlator would be,

$$V_m + \Delta V_n f_n f_m \quad (3.13)$$

and

$$V_n + \Delta V_m f_m f_n \quad (3.14)$$

By the property of the Walsh functions,

$$\int_0^\tau f_m(t)f_n(t) dt = 0 \quad (3.15)$$

where τ is the integration time. Therefore the correlator output will be proportional to,

$$V_m V_n \quad (3.16)$$

which consist of only the wanted terms, since all the other products average to zero. The effective removal of the unwanted terms depends on the ratio of the time difference between the ON and OFF states of the switching pulse to the period of the pulse. In the case of the GRH, the average value of the periods of the 32 Walsh functions is 100 ms and 10 μ s is the approximate gap between the ON and OFF states of the switching pulse. Therefore, the level in *dB* by which the cross-talk is brought down is given by,

$$10 \log \left(\frac{10 \times 10^{-6}}{100 \times 10^{-3}} \right) \approx -40 \text{ dB} \quad (3.17)$$

Figures 3.10 and 3.11 show the correlation count obtained by observing the emission from the sky background without and with Walsh switching. The sampling rate used was 2 MHz and integration time was 256 msec. Since the emission is mostly uncorrelated, the measured correlation count should be approximately 7678 as mentioned earlier, in the absence of any cross-talk between the signal channels. Figure 3.10 illustrates how the output is influenced by the cross-talk between the signal channels in the absence of Walsh switching. Here again we have plotted only the cosine output of the correlator as like in the DC offset test mentioned in the previous section. But when Walsh switching is employed, the cross-talk signals get averaged out and the average observed count is close to the expected value (Figure 3.11).

3.2.4 The 1024 Channel digital correlator

Figure 3.12 shows the block diagram of 1-bit digitizing circuit used in the GRH. The basic element is the high speed comparator (AD 790). The output of the comparator is a TTL signal corresponding to whether the input I.F. signal is below the ‘ground’ level or above it. This signal is then sampled in a D-type flip flop (74LS74). The sampled signal is demodulated for Walsh

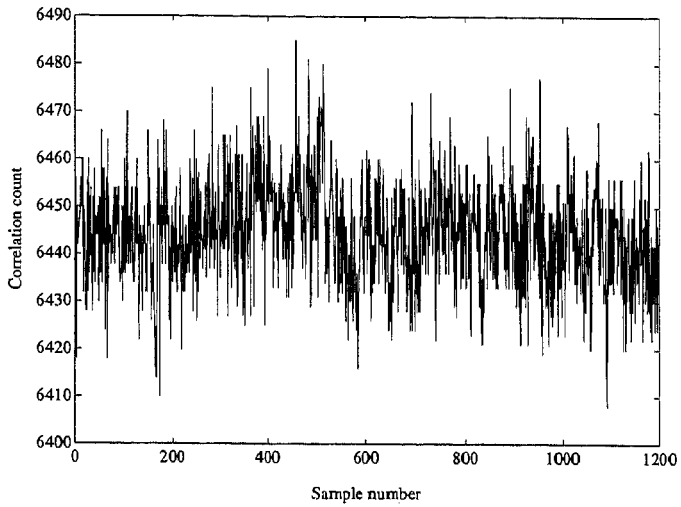


Figure 3.10: Correlator output for cross-talk test WITHOUT Walsh switching.

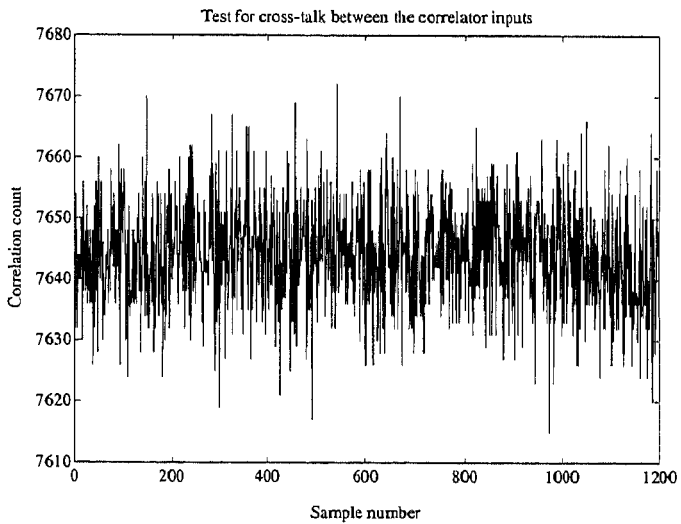


Figure 3.11: Correlator output for cross-talk test WITH Walsh switching.

switching using an Ex-OR gate (74LS86). After the removal of the phase inversion, the sampled signal then flows through the delay lines which have been constructed using a combination of shift registers (74LS164) and multiplexers (74LS151). The necessary delays are implemented as discussed in the earlier section under the control of a computer with the maximum value of the delay being $1.96 \mu\text{sec}$. This allows us to carry out observations of sources even at larger zenith distances without any coherence loss.

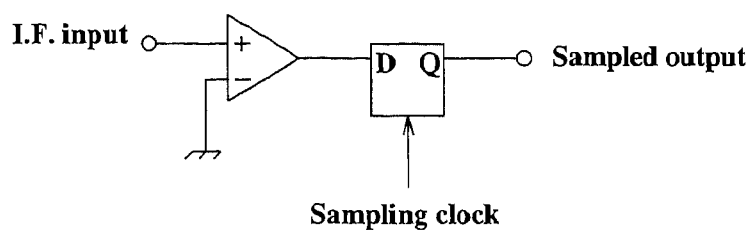


Figure 3.12: Block diagram of 1-bit sampler

The correlator system was built using the chips designed for the N_c radioheliograph, Japan. Each chip is composed of 4 complex correlator units, which corresponds to 2×2 combinations of antennas, and each unit consists of three 4-bit-parallel Ex-OR circuits, one 4-bit parallel Ex-NOR circuit, two addition circuits, two integration circuits, a latch, and a multiplexer circuit. Figure 3.13 shows a unit of the correlator chip. It is to be noted that in the 22-bit counter used for integration, only the 16 MSB^s are read out with the 6 LSB^s being truncated inside the chip itself. The functional diagram of the chip is shown in Figure 3.14, where C_s and S_s are the cosine and sine I.F. signals corresponding to each antenna. The output of the correlator 1 (cosine correlation) is,

$$C_1 \oplus C_2 + S_1 \oplus S_2 \quad (3.18)$$

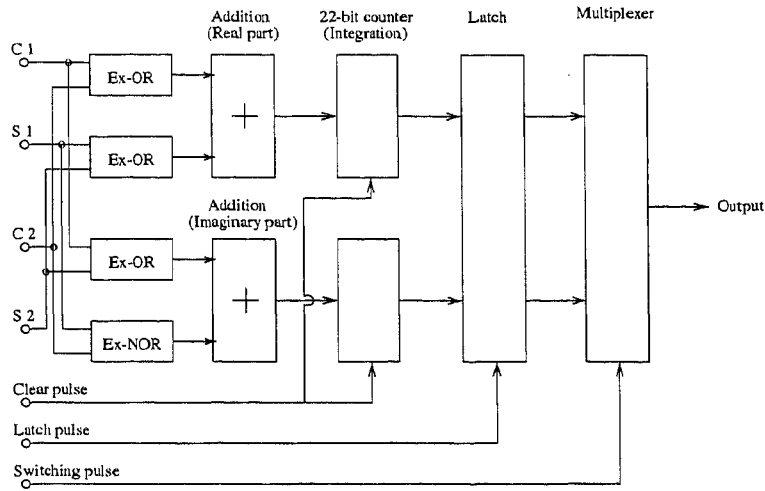


Figure 3.13: An elementary circuit of the correlator chip

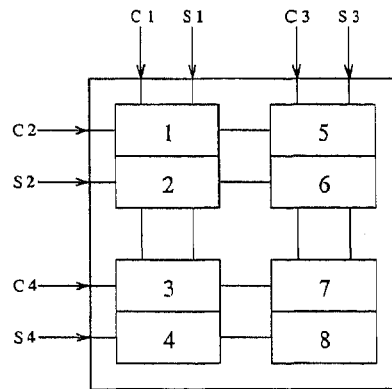


Figure 3.14: Functional diagram of the correlator chip

and the output of the correlator 2 (sine correlation) is,

$$C_1 \oplus S_2 + S_1 \bar{\oplus} C_2 \quad (3.19)$$

Here \oplus represents Ex-OR operation and $\bar{\oplus}$ represents Ex-NOR operation. Similarly the other correlators give corresponding outputs. Thus for each baseline, the chip gives four correlations compared to two (one each for the cosine and the sine correlations) by a single side band (SSB) correlator. But these additional correlations do not offer any advantage in the present case.

3.2.5 Data acquisition

The correlator system comprises of 8 boards and 16 correlator chips are mounted on each one of them. Each board correlates signals corresponding to 8×8 antenna pairs, giving 128 correlations. At the end of each integration period (about 145 msec), correlated data from each of these 128 correlators in one board will be written into a memory unit. This operation goes on synchronously in all the 8 boards. The process of reading correlated data from each chip and writing into the memory unit goes on till we reach 256 integration cycles. During this time i.e., when correlated data is being written into a memory unit, data which was written into another memory unit during earlier 256 integration cycles will be read into a computer. At the end of 256 integration cycles, the roles of the memory units get reversed.

3.3 Testing of the correlator chips

The major sources of errors in any correlator chip are: (1) misbehaviour of the counters and (2) accuracy of the correlator clock. To check the effect of these errors on the observed correlation count, we carried out a test as shown in Figure 3.15. The inputs to the correlator were left open (TTL 'High'). The clock speed used was 2 MHz and the acquired data were integrated for 256×10^{-3} seconds. As mentioned earlier, the correlator chip used in the GRH uses two correlators for each one of the cosine and sine outputs. Therefore for a fully correlated signal, the number of counts accumulated in the counter for the cosine channel should be $2 \times 2 \times 10^6 \times 256 \times 10^{-3} = 1024000$. As mentioned earlier, since we are reading only the 16 MSB^s from the counter, the expected number of counts is, $\frac{1024000}{2^8} = 16000$. The corresponding count in the sine channel should be 8000 (see equations 3.18 and 3.19).

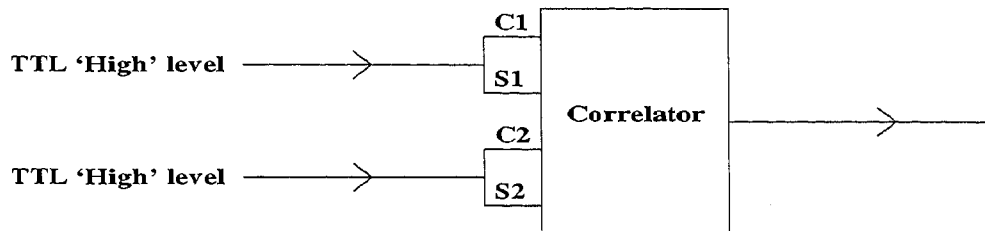


Figure 3.15: DC test for the correlator.

The measured correlation counts in the cosine and the sine outputs of the correlator were 15356 and 7678. As one can see there is only a small difference between the expected and the actual number of counts. This difference is too because of the effective integration time being less than 256×10^{-3} seconds, i.e. $(256 \times 10^{-3} - \Delta t)$ seconds, where Δt seconds is used for resetting the counters before the start of every new integration period. Though this test itself is enough to check the whether the counter is working as expected, we also performed another test to check the different stages of the counter. One of the inputs (1) to the correlator was left open as earlier, while a 2 MHz square waveform was given at the other input (2) as shown in Figure 3.16.

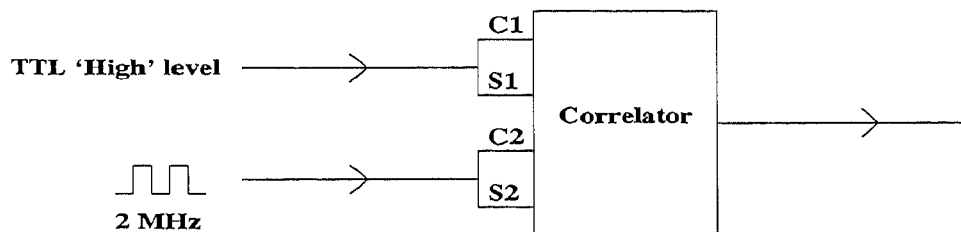


Figure 3.16: Test for the counters inside the correlator chip.

Figure 3.17 shows the cosine output of the correlator for different duty cycles of the input 2 MHz square waveform. Since the output increases linearly with the input, it is clear that different stages of the counter are working as expected. The sine output remained constant at 7586, irrespective of the duty

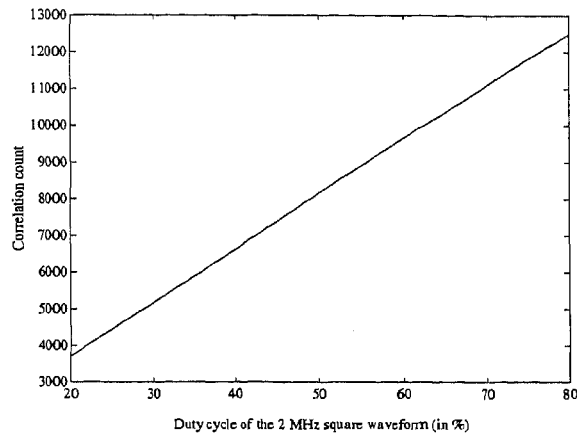


Figure 3.17: Variation of the correlator output (cosine channel) for different duty cycles of the input 2 MHz square waveform.

cycle of the input 2 MHz square waveform. As one can see from equation (3.19), this behaviour is expected since an increase in the duty cycle of the 2 MHz waveform increases the correlation corresponding to $C_1 \oplus S_2$ and decreases the correlation corresponding to $C_2 \oplus S_1$.

3.4 Correlator input level Vs residual offset

Though Walsh switching scheme is helpful in bringing down the level of the spurious correlation, there is always a residual offset present in the output of the correlator, as one can see from Figures 3.8 and 3.11. If the errors due to this residual offset varies with the level of the input signal, then there could be problems while observing extended sources like Sun since the observed visibility amplitude will not be the same over different baselines. We employed the test scheme shown in Figure 3.18 to find out the effect of this residual on the measured correlation count for different levels of the input signal (correlated) to the correlator. The results of this test for the cosine

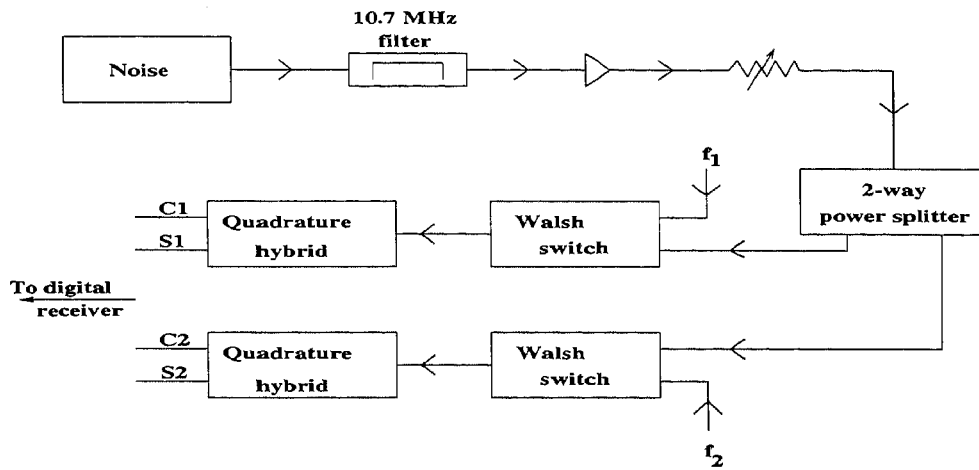


Figure 3.18: Test for checking the effect of residual offset on the level of the input (correlated) signal. f_1 and f_2 are Walsh switching signals.

and sine channels are shown in Figure 3.19. The correlation count in the sine channel remained approximately constant as expected, for different levels of the input. Even for the maximum level of the input, the phase errors due to the variation in the sine channel output was only $\approx 2^\circ$.

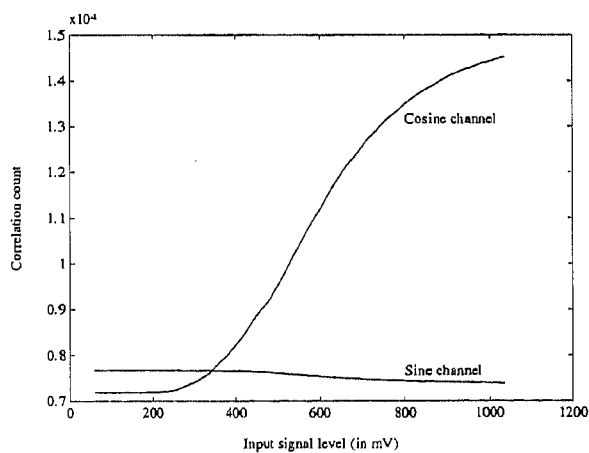


Figure 3.19: Correlator output for different levels of the input signal.

Appendix B

Appendix

B.1 Estimation of the correlation coefficient ρ_m from the measured correlation count in a one-bit correlator

In a one-bit correlator, the I.F. signals are digitized as either +1 or 0 (in some cases +1 and -1) depending on whether they are above or below the threshold level of the comparator. These are then sampled at the required rate, multiplied and averaged in a counter for a pre-determined length of time. The counter output gives the number of coincidences (N_c) between the two inputs to the correlator in a given averaging time. The correlation coefficient (ρ_m) has to be estimated from this.

From statistical theory, we know that the maximum and minimum values which ρ_m can take are +1 and -1, corresponding to the cases of full correlation and anti-correlation respectively. For the uncorrelated case, ρ will be 0. On the basis of this, we can construct a graph as shown in Figure B.1 for a one-bit

correlator. From the figure we can write,

$$\frac{\rho_m - 1}{N_c - N} = \frac{2}{N} \quad (\text{B.1})$$

where N is the the total number of samples in any one integration cycle.

Re-arranging equation B.1, we have,

$$\rho_m = \frac{2N_c}{N} - 1 \quad (\text{B.2})$$

Combining this with Van Vleck correction (Van Vleck and Middleton, 1966), the relation between the correlation co-efficient (ρ_t) of the unquantized case (analog correlator) and the observed correlation count N_c in a one-bit correlator is,

$$\rho_t = \sigma_1 \sigma_2 \sin \left[\frac{\pi}{2} \left(\frac{2N_c}{N} - 1 \right) \right] \quad (\text{B.3})$$

where σ_1 and σ_2 are the rms values of the input signal voltage to the correlator.

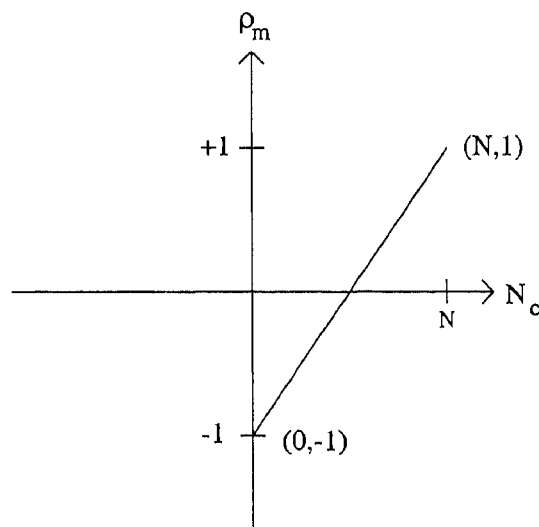


Figure B.1: Correlation co-efficient Vs correlation count in a one-bit correlator.

B.2 Amplitude information using a one-bit correlator

In a one-bit correlator, the output of the quantizer is either ‘high’ or ‘low’ with no information on the absolute strength of the signal (like in correlator systems with an Automatic Gain Control loop), as only the sign of the input waveform is retained. Thus the one-bit digital receiver measures the normalised correlation co-efficient. The output of a one-bit correlator is proportional to the ratio between the power of the correlated and the sum of the correlated plus uncorrelated signal fed at the input. If T_s is the source brightness temperature and T_b is the sky background temperature, then the input to the correlator is (see Figure B.2),

$$X \propto G \sqrt{T_s + T_b} \quad (\text{B.4})$$

where G is a constant. The measured correlation coefficient,

$$\rho_m \propto \frac{T_s}{T_s + T_b} \quad (\text{B.5})$$

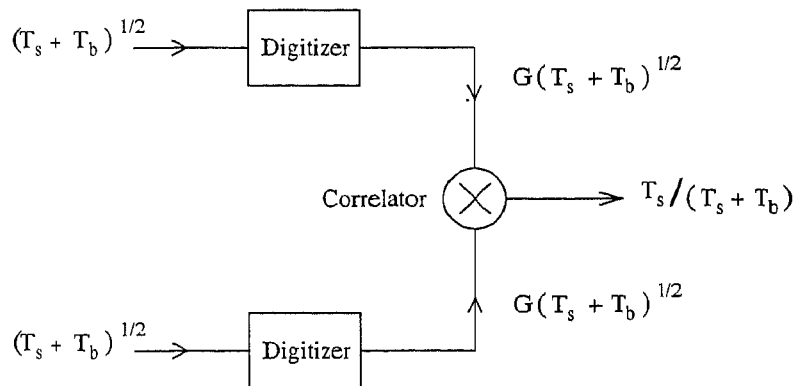


Figure B.2: Output of a one-bit correlator

On the other hand, the output of the analog correlator is proportional to the power of the input signal, i.e.

$$\rho_i \propto T_s \quad (\text{B.6})$$

Hence in order to get the above correlation coefficient from a one-bit digital correlator receiver, the total power received by the antenna i.e. $(T_s + T_b)$ has to be measured separately and multiplied with the measured correlation coefficient (ρ_m).

The conventional techniques to measure the strength of the signal requires square-law detectors, A/D convertors, etc. and also it will be difficult in synchronising the data collection with the correlator data. The following scheme devised by Udayashankar (1986) effectively uses the one-bit correlator itself (Figure B.3) to determine the amplitude of the input signal. It is assumed that the input is a Gaussian signal with a mean value zero (Figure B.4).

1. Digitize the signal to one-bit according to the transfer function.

If the input signal voltage $> V_{th}$, then the comparator output = 1

If the input signal voltage $< V_{th}$, then the comparator output = 0

2. Correlate this signal with 0 and measure the correlation coefficient ρ_m .

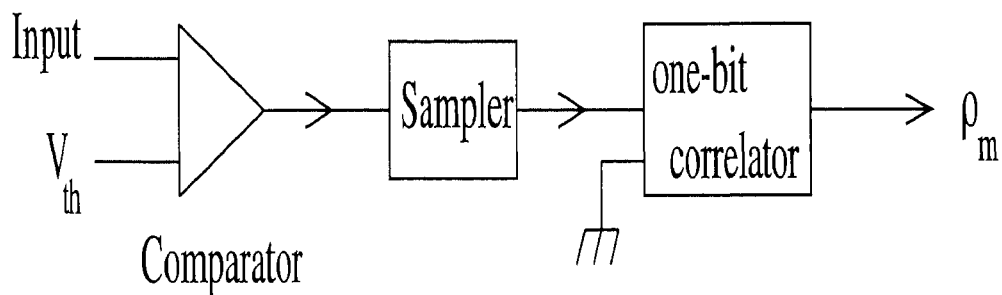


Figure B.3: Set-up to measure the total power using one-bit correlator

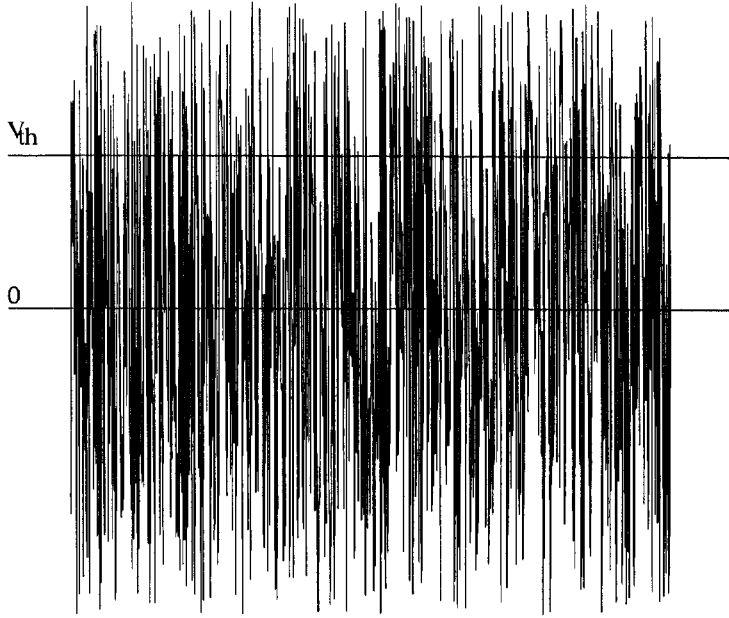


Figure B.4: Input signal to the comparator

$$\text{Probability that the signal voltage is } < V_{th} = \left\{ \begin{array}{l} \text{(Probability that the} \\ \text{voltage is in between} \\ \text{0 and } V_{th}) + \\ \text{(Probability that the} \\ \text{voltage is } < 0) \end{array} \right.$$

$$\text{The correlation coefficient } (\rho_m) = (1/N) \left\{ \begin{array}{l} \text{(Number of samples} \\ \text{with voltage } < V_{th}) - \\ \text{(Number of samples} \\ \text{with voltage } > V_{th}) \end{array} \right.$$

where N is the total number of samples in one integration period.

$$\text{Number of samples with voltage} < V_{th} = \begin{cases} (\text{Number of samples} \\ \text{with voltage} < 0) + \\ (\text{Number of samples} \\ \text{with voltage in between} \\ 0 \text{ and } V_{th}) \end{cases}$$

$$= N/2 + x$$

$$\text{Number of samples with voltage} > V_{th} = \begin{cases} (\text{Total number of} \\ \text{samples}) - (\text{Number of} \\ \text{samples with voltage} \\ < V_{th}) \end{cases}$$

$$= N - (N/2 + x)$$

So,

$$\rho_m = [(N/2 + x) - (N - N/2 - x)]/N$$

\Rightarrow

$$x = (N/2) \rho_m$$

Hence, number of samples with voltage $< V_{th} = N/2 + (N/2)\rho_m$

\Rightarrow Probability for the signal voltage to be $< V_{th} = [N/2 + (N/2)\rho_m]/N$

$$= [1 + \rho_m]/2$$

By Gaussian statistics, probability that the signal level is below V_{th} is given by,

$$\frac{1}{2} + \int_0^{V_{th}} \frac{1}{\sigma\sqrt{2\pi}} \exp\left[-t/(2\sigma^2)\right] dt$$

where σ^2 is the rms power of the signal.

i.e.,

$$\sigma^2 \propto (T_s + T_b) \quad (\text{B.7})$$

Substituting $t/(\sqrt{2}\sigma) = x$, the above integral can be re-written as,

$$\frac{1}{2} + \int_0^{V_{th}/(\sqrt{2}\sigma)} \frac{1}{\sigma\sqrt{2\pi}} \exp[-x^2] \sqrt{2} \sigma dx \quad (\text{B.8})$$

i.e.,

$$\frac{1}{2} + \frac{1}{\sqrt{\pi}} \int_0^{V_{th}/(\sqrt{2}\sigma)} \exp[-x^2] dx \quad (\text{B.9})$$

i.e.,

$$\frac{1}{2} + \frac{1}{2} \operatorname{erf}\left(\frac{V_{th}}{\sqrt{2}\sigma}\right) \quad (\text{B.10})$$

Thus,

$$\rho_m = \operatorname{erf}\left(\frac{V_{th}}{\sqrt{2}\sigma}\right) \quad (\text{B.11})$$

Using standard error function tables, the value of σ can be found from the above equation.

B.2.1 Calibration of the threshold level V_{th}

A proper adjustment of the threshold level is very crucial in getting a correct value for $(T_s + T_b)$. For the GRH, the set-up shown in Figure B.5 was employed to check how the output of the threshold detector varies with the input for different values of V_{th} . The value of σ was calculated from the measured correlation coefficient ρ_m for various peak-to-peak values (V_{pp}) of the input noise signal. The tests were repeated for different values of V_{th} . It was found

that when $V_{th} \approx 50$ mV, the output was linear with the input for values of V_{pp} in the range 150 - 200 mV (Figure B.6). Observations of the sky background in the direction of the radio sources Cassiopeia A and Cygnus A with the above settings gave the following results: The ratio between the values of the sky background temperature measured using the above set-up is,

$$\frac{T_b (Cas A)}{T_b (Cyg A)} \approx 0.66 \quad (B.12)$$

whereas the actual value is ≈ 0.70 (Kraus, 1966).

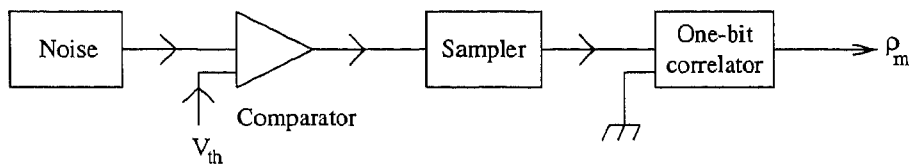


Figure B.5: Set-up to calibrate the threshold detector

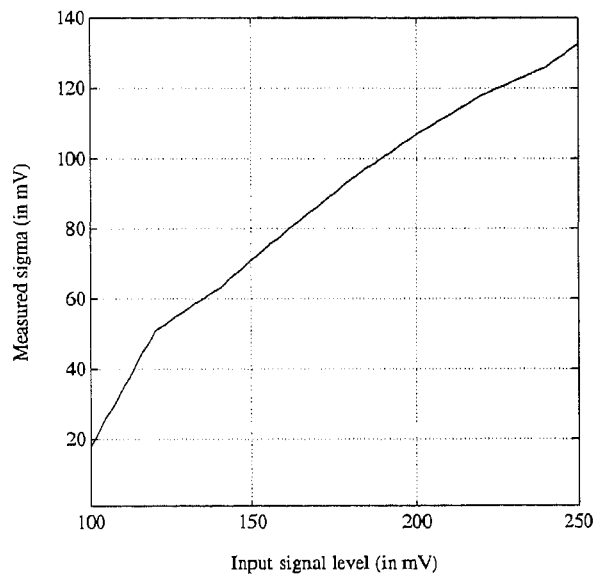


Figure B.6: Results of the test for calibration of the threshold detector.

Chapter 4

Calibration and Imaging

4.1 Introduction

A two-element correlation interferometer measures the spatial coherence of a distant radiation field at a given location as a function of the separation between the antennas, or baseline, measured in wavelengths. The output is usually referred to as the visibility function and is denoted by V_{ij} , with the subscripts indicating which pair of antennas is involved. An array of antennas samples this visibility function at many discrete locations. The process of calibration recovers the true visibilities from the observed quantities which are often corrupted for a multitude of reasons.

There are a wide variety of errors which can affect the visibility data obtained with a radio interferometer. These errors (ϵ) can be divided into different types, depending on whether they get added or multiplied or convolved with the measured visibility data V_{ij} (Ekers, 1989). Additive errors are those whose Fourier transform $F\epsilon$ is added to the image, i.e.,

$$V + \epsilon \rightleftharpoons I + F\epsilon \quad (4.1)$$

where the \rightleftharpoons symbol denotes a Fourier transform relationship between the measurement (u, v) plane and the image (l, m) plane. Examples of additive errors are interference, cross-talk, correlator offsets and receiver noise. These errors are termed additive since they give rise to spurious correlation which affects mainly the signal-to-noise (SNR) of the observed complex visibilities. The position of the structures in the source is not affected.

If the errors ϵ are multiplicative, then

$$V\epsilon \rightleftharpoons I\star F\epsilon \quad (4.2)$$

i.e., the Fourier transform of the errors is convolved with the observed brightness distribution. Examples are atmospheric and ionospheric errors, baseline-based errors like band-pass mismatches, delay errors, etc. These errors introduce extra path difference between the individual signal channels and hence corrupt the phase of the true complex visibility pertaining to the source under study. Since the phase of a complex quantity is affected only when it gets multiplied with another, these errors are called multiplicative errors.

The next type of errors are those which get convolved with the observed visibility function, i.e.

$$V\star\epsilon \rightleftharpoons I F\epsilon \quad (4.3)$$

Examples are the effect of the primary beam of the array elements, since in radio interferometry, the observed brightness is always weighted (multiplied) by the antenna pattern (Equation 4.12).

Due to these errors the observed complex visibility (V^{obs}) on a certain baseline differs from the true response (V^{true}) leading to inaccuracies in the determination of the sky brightness distribution. The measured visibility on the baseline formed by the antennas G_i and G_j can be written as:

$$V_{ij}^{obs} = V_{ij}^{true} g_i g_j^* g_{ij} + c_{ij} + \epsilon_{ij} \quad (4.4)$$

Here g_i is the complex gain of the i^{th} antenna, incorporating all the antenna based amplitude and phase errors, the $*$ denotes complex conjugation. The term g_{ij} represents the baseline dependant complex gain; c_{ij} is an additive error and ϵ_{ij} is the thermal noise plus possible interference. In this chapter, we discuss briefly some of the calibration schemes that are generally used for correcting the visibilities observed with an interferometer array and the practical problems in applying them to an array like the GRH. The schemes have been broadly classified into two categories: (i) *external calibration*, where the correction terms are determined from observations of sources other than those under study and (ii) *internal calibration*, where the correction terms are determined from the source under study itself. The later part of the chapter describes in detail a hybrid scheme that we developed based on the well known principles of closure and redundancy and which is presently being used for calibrating the GRH data.

4.1.1 External calibration

If we assume that the instrumental and atmospheric errors remain constant in time and direction, then the observations of (nearby) calibration sources with known flux and position can be used to correct the observed visibilities of the source under study. In principle this allows the elimination of the terms $g_i g_j g_{ij}^*$ and c_{ij} in equation (4.4) because a calibrator source allows us to predict V_{ij}^{true} , and if its flux is high enough, the noise term ϵ_{ij} can be neglected. In practice this method will work well if, (i) the calibrator source is close to the object under study so that the propagation effects are indistinguishable and (ii) the antenna beam position can be frequently changed between the calibrator and the field of interest. But in the case of dipole arrays like the GRH, changing the position of the antenna beam requires introduction of

phase gradients across the array as mentioned in Chapter 2. This would mean that the instrumental errors may not remain constant, i.e. they change everytime the beam is shifted. The correction terms inferred from observations of a calibration source may not apply to a source observed at a different time and in a different part of the sky, due to the temporal and spatial variations in the ionosphere through which the wavefront passes before reaching the array elements (Kassim et al. 1993). Another reason for not opting for the external calibration method for the GRH is due to the open-wire transmission lines used for bringing the R.F. signals from the field to the receiver building. Though the relative phase variation between the lines is small, since there is a length difference between the lines from the antenna groups in the South arm and the E-W arm, the phase variations due to temperature changes of the ambient medium are difficult to compensate. However the coherence loss due to this length difference is avoided by delaying the signal appropriately before correlation.

4.1.2 Internal calibration

In any radio interferometer array, most data corruption occurs before the signals are correlated. Therefore the errors in the observed visibilities can be ascribed to the individual antennas. If all the antenna pairs in a N element array are cross-correlated, then at any one time, we have $\frac{1}{2} N(N-1)$ complex visibility measurements. But there are only N complex antenna gain errors. Therefore, in principle one can solve for the complex antenna gain factors using the observed field itself (Pearson and Readhead, 1984). There are two different variants of internal calibration that are generally employed:

4.1.3 Self-calibration

The basic idea of self-calibration technique (Readhead and Wilkinson, 1978; Schwab, 1980; Cotton, 1981; Cornwell and Wilkinson, 1981) is that given a source model whose visibility function is V^{mod} , one can solve for the error terms (g^s) by iteratively minimizing the quantity

$$\sum_{1 \leq i < j \leq n} |V_{ij}^{obs} - g_i g_j^* V_{ij}^{mod}|^2 \quad (4.5)$$

To begin with, an initial model of the source is made with whatever details that are available and at the end of each step, a new model is generated using the corrected data. The iteration process is carried out till the residuals reach a minimum (Schwab, 1984). Images of high dynamic range can be made using self-calibration technique (Perley, 1989) although it is presumed to be sensitive to the choice of model distribution that is assumed initially (Shevgaonkar, 1984). But according to Cornwell and Fomalont (1989), self-calibration fails when the source is too complex relative to the model. It is well known that the Sun can be a highly complex source at times. Because of these problems and due to the non-availability of the AIPS software at the Gauribidanur observatory, self-calibration scheme is not used for correcting the GRH data.

4.1.4 Redundancy calibration

Redundant baseline calibration uses the fact that for some types of synthesis arrays, the same baseline vector occurs more than once. Because the true visibilities on identical baselines are equal the measured visibilities themselves can be used to derive the complex antenna gains (instrumental and atmospheric effects). If all the antenna pairs are correlated, then the system of equations given by Eq.(4.4) will be over-determined and one can employ a

least squares technique to estimate the error terms independent of any models or a priori information on the sky brightness distribution (Wieringa, 1991). It has been shown (Noordam and de Bruyn, 1982; Koshishi et al., 1994) that images of high dynamic range can be obtained using calibration schemes based purely on redundancy technique. In the case of the GRH, the baselines in the E-W and the South arms occur more than once, except for the longest baseline along either arm. In principle, the antenna phases of the elements along the E-W arm can be found by using the redundant baselines along the E-W arm. Similarly the antenna phases of the elements along the South arm can be found by using the redundant baselines in that arm. These antenna phases can then be used to correct the observed visibilities on the E-W x S cross baselines, since in a T-shaped array like the GRH, only the visibilities on the cross baselines are necessary for making a 2D map. But due to the presence of delay shifters in the South arm, we are not using this method in the GRH. Since the delay shifters are not set to compensate the exact path length differences between individual antennas in the South arm, there will be residual phase errors. This error will not be present in the antenna phases of the South arm determined by using the redundancy only in that arm. On the other hand, this additional phase due to delay error will contribute to the observed visibility phases between the groups in the E-W and the South arms. Therefore if we to correct the observed visibilities on the cross baselines using the antenna phases of the South arm estimated with the available redundancy in that arm only, there will a shift in the source position along the North-South direction.

4.2 Calibration scheme used in the GRH

In view of the above mentioned problems in adapting the existing phase calibration schemes to the GRH, we had to develop our own imaging scheme. It is shown that a combination of the closure phase method (Jennison, 1958; Rogers et al., 1974) and the availability of redundant baselines can be effectively used to correct the phase errors in the observed complex visibilities. Since the E-W and the South arm of the GRH contain 16 groups each, there are altogether 256 visibilities available for making a 2D map. The observed visibilities are corrected using a phase calibration scheme in which apart from the 256 E-W x S baselines, we also use the fundamental baselines formed by the multiplications $(G_1 \times G_2)$, $(G_2 \times G_3) \dots (G_{15} \times G_{16})$ in the E-W arm. The reason for using the fundamental baselines in the E-W arm is explained in a later section.

4.2.1 Principle of the method

Neglecting the errors due to noise fluctuations in the receiver system, the phase of the observed complex visibility on the baseline formed by the antenna groups G_i and G_j is given by,

$$\phi_{ij}^{obs} = \phi_{ij}^{true} + \phi_i^{err} - \phi_j^{err} + \phi_{ij}^g \quad (4.6)$$

By precisely calculating the time of transit of the centroid of the optical Sun over the local meridian at Gauribidanur, the geometric phase term ϕ_{ij}^g (due to the orientation of the interferometer baseline with respect to the direction of the source) is eliminated from the above equation by using the equation,

$$\begin{aligned} \phi^g &= 2\pi\nu\tau_g \\ &= (u\cos(\delta)\sin(H) + v(\cos(\delta)\cos(H)\sin(\phi) - \sin(\delta)\cos(\phi)) \\ &\quad + w(\cos(\delta)\cos(H)\cos(\phi) + \sin(\delta)\sin(\phi)) \end{aligned}$$

where

- u, v, w - X,Y,Z components of the baseline
- τ_g - delay between the arrival time of the wavefronts
- δ - declination of the source
- ϕ - latitude of the observer
- H - hour angle of the source

Therefore equation (4.6) becomes,

$$\phi_{ij}^{obs} = \phi_{ij}^{true} + \phi_i^{err} - \phi_j^{err} \quad (4.7)$$

The remaining antenna based errors (ϕ_i^{err}) can be eliminated from this equation by forming a closure relation (Jennison, 1956) between the antenna groups G_i , G_j and G_k as shown below.

$$\theta_{ijk} = \phi_{ij}^{obs} + \phi_{jk}^{obs} - \phi_{ik}^{obs} \quad (4.8)$$

i.e.,

$$\theta_{ijk} = \phi_{ij}^{true} + \phi_{jk}^{true} - \phi_{ik}^{true} \quad (4.9)$$

This equation is free of any error terms. By forming all possible closure equations of this type in an N element interferometer and arranging them in the matrix form,

$$Ax = b \quad (4.10)$$

where, A - coefficient matrix

x - column matrix consisting of the true visibility phases (ϕ^{true})

b - column matrix consisting of the closure phases (θ)

one can solve for the true visibility phase (ϕ^{true}) on any baseline using matrix inversion techniques. These phases can then be combined with the observed visibility amplitudes on the corresponding baseline to form the true complex

visibility pertaining to the source. It is to be noted that it is not absolutely necessary to remove the geometrical phase term in equation (4.6) since it will automatically get cancelled while summing the observed phases on the baselines between any 3 interferometers as shown in equation (4.9). In spite of this, the removal of ϕ_g is carried out in the calibration scheme used in the GRH. This helps in removing the phase errors due to the height differences among the various antenna groups so that the redundancy in the baselines, which helps in reducing the number of unknowns, is preserved.

4.2.2 Application to GRH

Consider the multiplications between the groups $G_1, G_2, G_3 \dots G_{16}$ in the E-W arm and G_{17} in the South arm. The possible independent closure equations are,

$$\begin{aligned} \theta_{1,2,17} &= \phi_{1,2}^{true} + \phi_{2,17}^{true} - \phi_{1,17}^{true} \\ \theta_{2,3,17} &= \phi_{2,3}^{true} + \phi_{3,17}^{true} - \phi_{2,17}^{true} \\ &\cdot \\ &\cdot \\ &\cdot \\ \theta_{15,16,17} &= \phi_{15,16}^{true} + \phi_{16,17}^{true} - \phi_{15,17}^{true} \end{aligned}$$

There are 15 equations, whereas the unknowns (ϕ_{ij}^{true}) to be solved for are 17. But the terms $\phi_{1,2}^{true}, \phi_{2,3}^{true} \dots \phi_{15,16}^{true}$ can be set to zero, since the corresponding baselines formed by the multiplications ($G_1 \times G_2$), ($G_2 \times G_3$)... ($G_{15} \times G_{16}$) are redundant and also small enough in length (80 m), that Sun remains unresolved, in our frequency range of observation. Although, this brings down the number of unknowns to 16, it is still one more than the number

of equations. This problem can be better understood if the above set of equations are written in a matrix form as shown below:

$$\begin{pmatrix}
 -1 & 1 & 0 & 0 & 0 & 0 & 0 & 0 & 0 & 0 & 0 & 0 & 0 & 0 & 0 & 0 \\
 0 & -1 & 1 & 0 & 0 & 0 & 0 & 0 & 0 & 0 & 0 & 0 & 0 & 0 & 0 & 0 \\
 0 & 0 & -1 & 1 & 0 & 0 & 0 & 0 & 0 & 0 & 0 & 0 & 0 & 0 & 0 & 0 \\
 0 & 0 & 0 & -1 & 1 & 0 & 0 & 0 & 0 & 0 & 0 & 0 & 0 & 0 & 0 & 0 \\
 0 & 0 & 0 & 0 & -1 & 1 & 0 & 0 & 0 & 0 & 0 & 0 & 0 & 0 & 0 & 0 \\
 0 & 0 & 0 & 0 & 0 & -1 & 1 & 0 & 0 & 0 & 0 & 0 & 0 & 0 & 0 & 0 \\
 0 & 0 & 0 & 0 & 0 & 0 & -1 & 1 & 0 & 0 & 0 & 0 & 0 & 0 & 0 & 0 \\
 0 & 0 & 0 & 0 & 0 & 0 & 0 & -1 & 1 & 0 & 0 & 0 & 0 & 0 & 0 & 0 \\
 0 & 0 & 0 & 0 & 0 & 0 & 0 & 0 & -1 & 1 & 0 & 0 & 0 & 0 & 0 & 0 \\
 0 & 0 & 0 & 0 & 0 & 0 & 0 & 0 & 0 & -1 & 1 & 0 & 0 & 0 & 0 & 0 \\
 0 & 0 & 0 & 0 & 0 & 0 & 0 & 0 & 0 & 0 & -1 & 1 & 0 & 0 & 0 & 0 \\
 0 & 0 & 0 & 0 & 0 & 0 & 0 & 0 & 0 & 0 & 0 & -1 & 1 & 0 & 0 & 0 \\
 0 & 0 & 0 & 0 & 0 & 0 & 0 & 0 & 0 & 0 & 0 & 0 & -1 & 1 & 0 & 0 \\
 0 & 0 & 0 & 0 & 0 & 0 & 0 & 0 & 0 & 0 & 0 & 0 & 0 & -1 & 1 & 0 \\
 0 & 0 & 0 & 0 & 0 & 0 & 0 & 0 & 0 & 0 & 0 & 0 & 0 & 0 & -1 & 1
 \end{pmatrix}
 \begin{pmatrix}
 \phi_{1,17}^{true} \\
 \phi_{2,17}^{true} \\
 \phi_{3,17}^{true} \\
 \phi_{4,17}^{true} \\
 \phi_{5,17}^{true} \\
 \phi_{6,17}^{true} \\
 \phi_{7,17}^{true} \\
 \phi_{8,17}^{true} \\
 \phi_{9,17}^{true} \\
 \phi_{10,17}^{true} \\
 \phi_{11,17}^{true} \\
 \phi_{12,17}^{true} \\
 \phi_{13,17}^{true} \\
 \phi_{14,17}^{true} \\
 \phi_{15,17}^{true} \\
 \phi_{16,17}^{true}
 \end{pmatrix}
 =
 \begin{pmatrix}
 \theta_{1,2,17} \\
 \theta_{2,3,17} \\
 \theta_{3,4,17} \\
 \theta_{4,5,17} \\
 \theta_{5,6,17} \\
 \theta_{6,7,17} \\
 \theta_{7,8,17} \\
 \theta_{8,9,17} \\
 \theta_{9,10,17} \\
 \theta_{10,11,17} \\
 \theta_{11,12,17} \\
 \theta_{12,13,17} \\
 \theta_{13,14,17} \\
 \theta_{14,15,17} \\
 \theta_{15,16,17}
 \end{pmatrix}$$

One can see that the coefficient matrix on the left hand side is not square, as the number of unknown parameters are one more than the estimated closure phases (θ_{ijk}). To overcome this problem, the coefficient matrix is first augmented with a row of zeroes, thereby making it a square matrix. Similarly the right hand side column matrix is also augmented. Then using the technique of singular value decomposition¹ (SVD) to invert the coefficient matrix, a least squares solution (Press et al., 1992) for the unknown visibility

¹Since the coefficient matrix is augmented with a row of zeroes, it becomes a singular matrix.

-.9375	-.8750	-.8125	-.7500	-.6875	-.6250	-.5625	-.5000	-.4375	-.3750	-.3125
-.2500	-.1875	-.1250	-.0625	0						
.0625	-.8750	-.8125	-.7500	-.6875	-.6250	-.5625	-.5000	-.4375	-.3750	-.3125
-.2500	-.1875	-.1250	-.0625	0						
.0625	.1250	-.8125	-.7500	-.6875	-.6250	-.5625	-.5000	-.4375	-.3750	-.3125
-.2500	-.1875	-.1250	-.0625	0						
.0625	.1250	.1875	-.7500	-.6875	-.6250	-.5625	-.5000	-.4375	-.3750	-.3125
-.2500	-.1875	-.1250	-.0625	0						
.0625	.1250	.1875	.2500	-.6875	-.6250	-.5625	-.5000	-.4375	-.3750	-.3125
-.2500	-.1875	-.1250	-.0625	0						
.0625	.1250	.1875	.2500	.3125	-.6250	-.5625	-.5000	-.4375	-.3750	-.3125
-.2500	-.1875	-.1250	-.0625	0						
.0625	.1250	.1875	.2500	.3125	.3750	-.5625	-.5000	-.4375	-.3750	-.3125
-.2500	-.1875	-.1250	-.0625	0						
.0625	.1250	.1875	.2500	.3125	.3750	.4375	-.5000	-.4375	-.3750	-.3125
-.2500	-.1875	-.1250	-.0625	0						
.0625	.1250	.1875	.2500	.3125	.3750	.4375	.5000	-.4375	-.3750	-.3125
-.2500	-.1875	-.1250	-.0625	0						
.0625	.1250	.1875	.2500	.3125	.3750	.4375	.5000	.5625	-.3750	-.3125
-.2500	-.1875	-.1250	-.0625	0						
.0625	.1250	.1875	.2500	.3125	.3750	.4375	.5000	.5625	.6250	-.3125
-.2500	-.1875	-.1250	-.0625	0						
.0625	.1250	.1875	.2500	.3125	.3750	.4375	.5000	.5625	.6250	.6875
-.2500	-.1875	-.1250	-.0625	0						
.0625	.1250	.1875	.2500	.3125	.3750	.4375	.5000	.5625	.6250	.6875
.7500	-.1875	-.1250	-.0625	0						
.0625	.1250	.1875	.2500	.3125	.3750	.4375	.5000	.5625	.6250	.6875
.7500	.8125	-.1250	-.0625	0						
.0625	.1250	.1875	.2500	.3125	.3750	.4375	.5000	.5625	.6250	.6875
.7500	.8125	.8750	-.0625	0						
.0625	.1250	.1875	.2500	.3125	.3750	.4375	.5000	.5625	.6250	.6875
.7500	.8125	.8750	.9375	0						

phases is obtained (see page 67 for the inverse of the coefficient matrix). In a similar way another set of 16 equations for the multiplication of the groups in the E-W arm with the group G_{18} in the South arm is formed and the unknowns are found as before. Likewise the entire operation is carried out 16 times corresponding to each one of the 16 groups in the South arm. In each step, a set of 16 unknowns are determined and thus at the end of 16th step, we have all the 256 ϕ_{ij}^{true} corresponding to the E-W x S multiplications.

In principle one can solve for all the 256 visibility phases at one time using the entire set of 240 closure equations corresponding to all the 16 antenna groups in the South arm². In this case also the number of equations are less than the unknowns, but it may appear that the errors in the estimated visibility phases will be comparatively less, as they will be spread over a larger set. It can be shown that even in this case the errors in the final set of visibility phases will be the same as before, since the elements of the coefficient matrix in this case would essentially be the periodic repetitions of the coefficient matrix in the scheme mentioned in the previous paragraph at 16 different locations corresponding to the unknowns which are to be solved for. All the other elements of the coefficient matrix will be zero.

4.2.3 Error estimation

As it is well known that in an ill-determined system of equations where the number of available equations is less than the unknowns to be solved for, one cannot expect an unique solution (Press et al., 1992). Since in our case the number of equations is one less than the unknowns, a residual error will still be present in each one of the obtained visibility phases. From the matrices

²Here one has to augment the coefficient matrix and the right hand side column matrix with 16 rows of zeroes.

given in page 66 and 67 one can see that,

$$\phi_{1,17} = 0.9375 \phi_{1,17} - 0.0625 (\phi_{2,17} + \phi_{3,17} + \dots + \phi_{16,17}) \quad (4.11)$$

This implies that the deviation in $\phi_{1,17}$ from its true value is only 6.25%. Similarly one can show that the deviations in the other visibility phases is also 6.25%. These deviations are small and hence can be neglected.

Another possible source of error that can affect the visibility phases is the residual baseline based errors (Cornwell and Fomalont, 1989) which will be present inspite of employing phase switching techniques mentioned in Chapter 3. These errors cannot be ascribed to individual antennas and so will not get cancelled through closure methods. The magnitude of these errors can be estimated by observing a point source whose position in the sky is known (Cornwell and Fomalont, 1989). Figure 4.1 shows a plot of these residual errors in one of the closed loop of baselines in the GRH.

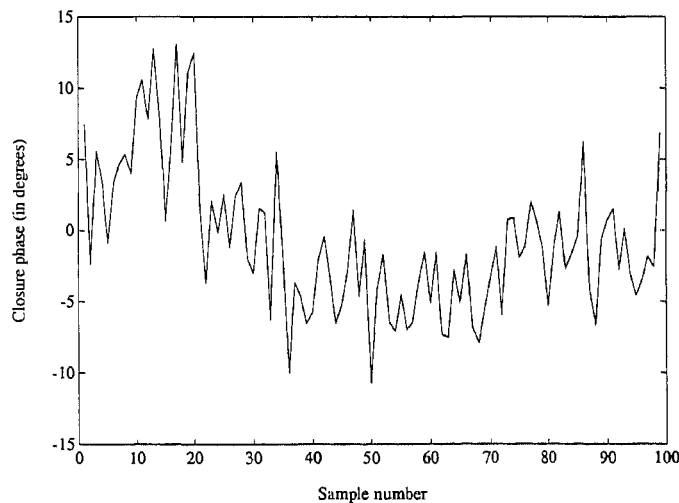


Figure 4.1: Closure phase obtained on the source Cygnus A by summing the observed phases on the baselines formed by the multiplications (8,9), (9,17) and (8,17). The successive samples are separated by about 4.64 secs.

One can neglect these errors since their r.m.s. variation is small ($\approx 3^\circ$). We have taken the closed loop of baselines formed by the antenna groups G_8 , G_9 and G_{17} since the u and v-components of the baselines formed by these antenna groups are the smallest in the GRH and so any possible closure errors due to large scale structures in the sky background should be large in this closure set. The number of samples displayed in Figure 4.1 is rather small, since the duration of observation of any source with the GRH is limited to the half-power width of the primary beam of the groups in the E-W arm, and is equal to approximately 24 minutes (6°) at 40 MHz. The sinusoidal trend that one can see in Figure 4.1 is probably due to the non-closing visibility phases corresponding to the structures in the sky background. These structures are generally resolved on the longer baselines.

4.3 Map formation

The observed complex visibility on any interferometer baseline is,

$$V(u, v, w) = \int \int A(l, m) B(l, m) \exp[-j(lu + mv + nw)] \frac{dl dm}{n} \quad (4.12)$$

where u, v, w are the X, Y, Z components of the baseline in wavelengths expressed in radians, $B(l, m)$ is the sky brightness distribution, $A(l, m)$ is the antenna response and $j = \sqrt{-1}$. In the notation that is followed, X points westwards, Y southwards and Z zenithwise; l, m, n are the direction cosines with these three axes for any point in the sky. As the sky is two dimensional, two independent coordinates are enough to describe any point uniquely and therefore, $n = \sqrt{1 - l^2 - m^2}$. From equation (4.12), the sky brightness distribution is given by,

$$\frac{A(l, m) B(l, m)}{n} = \int \int \int V(u, v, w) \exp[j(lu + mv + nw)] du dv dw \quad (4.13)$$

For a restricted range of l and m , $V(u, v, w)$ is approximately independent of w and hence we can write,

$$\frac{A(l, m) B(l, m)}{n} = \int \int V(u, v) \exp[j(lu + mv)] du dv \quad (4.14)$$

For transit, $l = 0$. Hence,

$$\frac{A(0, m) B(0, m)}{\sqrt{1 - m^2}} = \int V(u, v) \exp[j(mv)] dv \quad (4.15)$$

Calling the lefthand side as raw map, one can solve this for every integration at transit. To avoid the aliasing effects due to the grating lobes that are present in the E-W direction in an array like the GRH (Appendix C.1), a one-dimensional Fourier transform is used to get the sky brightness distribution.

In practice the observed visibilities have to be corrected for amplitude and phase errors before the Fourier transformation is carried out. For each observed complex visibility (i.e., $A_c \cos\theta + jA_s \sin\theta$, where A_c and A_s are the deflections in the cosine and sine channels respectively) we have an amplitude,

$$G = \sqrt{A_c^2 + A_s^2}, \quad (4.16)$$

which has information about the strength of the source. The corresponding phase term which contains information on the position of the source in the sky is,

$$\phi = \tan^{-1} \left(\frac{A_s \sin\theta}{A_c \cos\theta} \right) \quad (4.17)$$

The amplitude term can be corrupted because of gain differences between the various antenna groups and their associated receiver channels. In GRH, these are corrected by observing a point (calibrator) source³, since it should give the same deflection at the output of all the interferometer pairs. Any difference

³Since in the case of GRH, the amplitude errors are relatively small compared to the phase errors, we use the external calibration scheme for correcting the amplitude errors.

in the deflection is noted down and while observing Sun, it is applied as a correction as shown below.

$$\left(G_{ij}^{true}\right)_{Sun} = \left(G_{ij}^{obs}\right)_{Sun} \left(\frac{G_{ij}}{G_{max}}\right)_{cal} \quad (4.18)$$

The corrected amplitudes along with the corresponding phases (corrected as described in the previous section) are then Fourier transformed to get the map. In practice, only a Discrete Fourier Transformation as shown in equation 4.19 is carried out because of the non-uniformity in the distribution of the baseline lengths⁴ along the v -axis from the origin of the uv -plane, which is taken to be the center of the E-W arm.

$$B(0, m) \propto \sum_{j=1}^{16} V(u, v) \exp\left(-i2\pi\frac{v_j}{\lambda}m\right) \quad (4.19)$$

Figure 4.2 shows the map of the solar corona at 75 MHz obtained with the Gauribidanur radioheliograph on April 20, 1997 at 06:30 UT. This map was obtained after the removal of phase errors in the observed complex visibilities using the hybrid method we have developed. Figure 4.3 shows a similar map obtained with the Nancay radioheliograph on the same day, but at 164 MHz. The 75 MHz map obtained using the external calibration method⁵ i.e., by correcting for the instrumental errors using the values estimated through observations of the radio source Virgo A (which is a point source for the GRH) at 16:45 UT is shown in Figure 4.4. During the course of my visit to VLA in connection with the Summer school on Synthesis Imaging, I had an opportunity to run the self-cal routine in AIPS on the GRH data. Figure 4.5

⁴The distance of the first group (G_{17}) in the South arm from the center of the E-W arm is 10.5 m, whereas the other groups in that arm are away from G_{17} by distances which are in integral multiples of 28 m.

⁵It should be noted that in the case of the GRH, the external calibration scheme can be used only if the declination and the right ascension of the calibrator is close to that of the Sun.

shows the map obtained using the self-cal technique for which with the map in Figure 4.2 was used as the starting model. Because of the improved dynamic range, one can now clearly see the discrete source close to the limb on the east. To verify the correctness of our technique, we also compared the GRH maps with the X-ray images of the Sun obtained using the Soft X-ray telescope on board YOHKOH satellite. Figure 5.8 (next chapter) shows one such comparison. As one could see there is a very good spatial correspondence between the features seen in the radio and the X-ray pictures. The similarity between the maps obtained using our technique and those made using other techniques and at other wavelengths indicates that the phase calibration scheme that we have developed works well and is particularly useful for antenna arrays like the GRH.

GAURIBIDANUR RADIO HELIOGRAM - 75 MHz

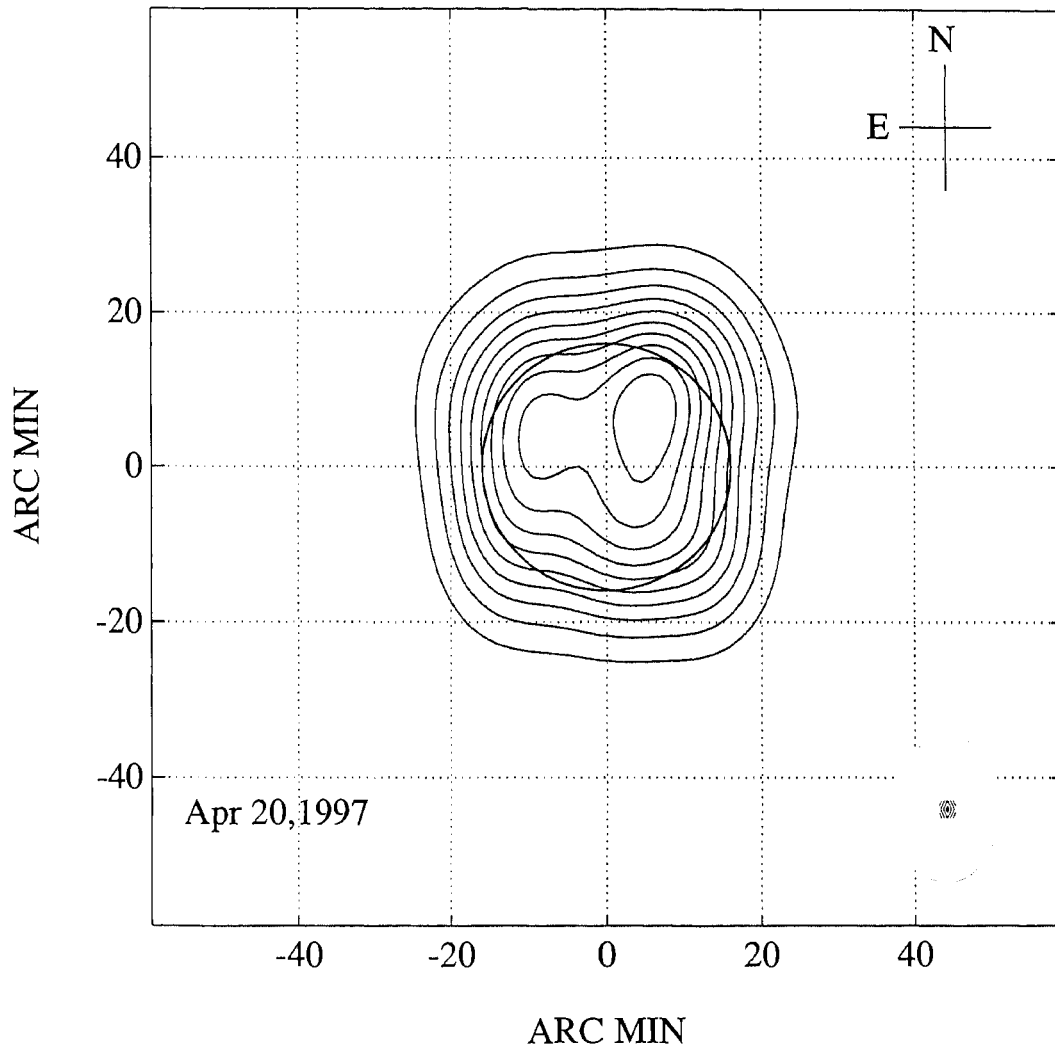


Figure 4.2: Map made by elimination of phase errors using redundancy and closure techniques. The open circle at the centre is the solar limb and the filled circle at the bottom right is the beam of the instrument.

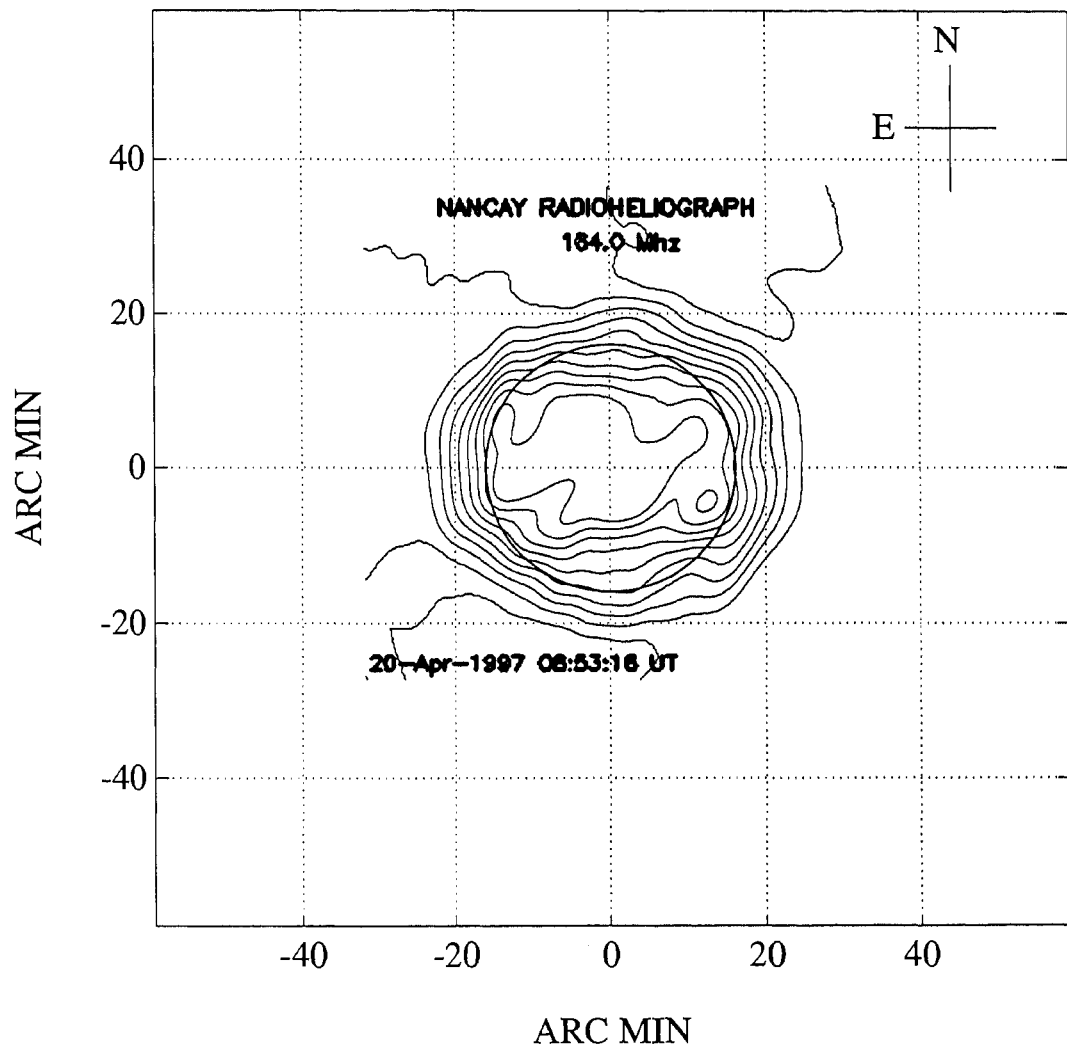


Figure 4.3: Map obtained with the Nancay radio heliograph at 164 MHz on the same day.

GAURIBIDANUR RADIO HELIOGRAM - 75 MHz

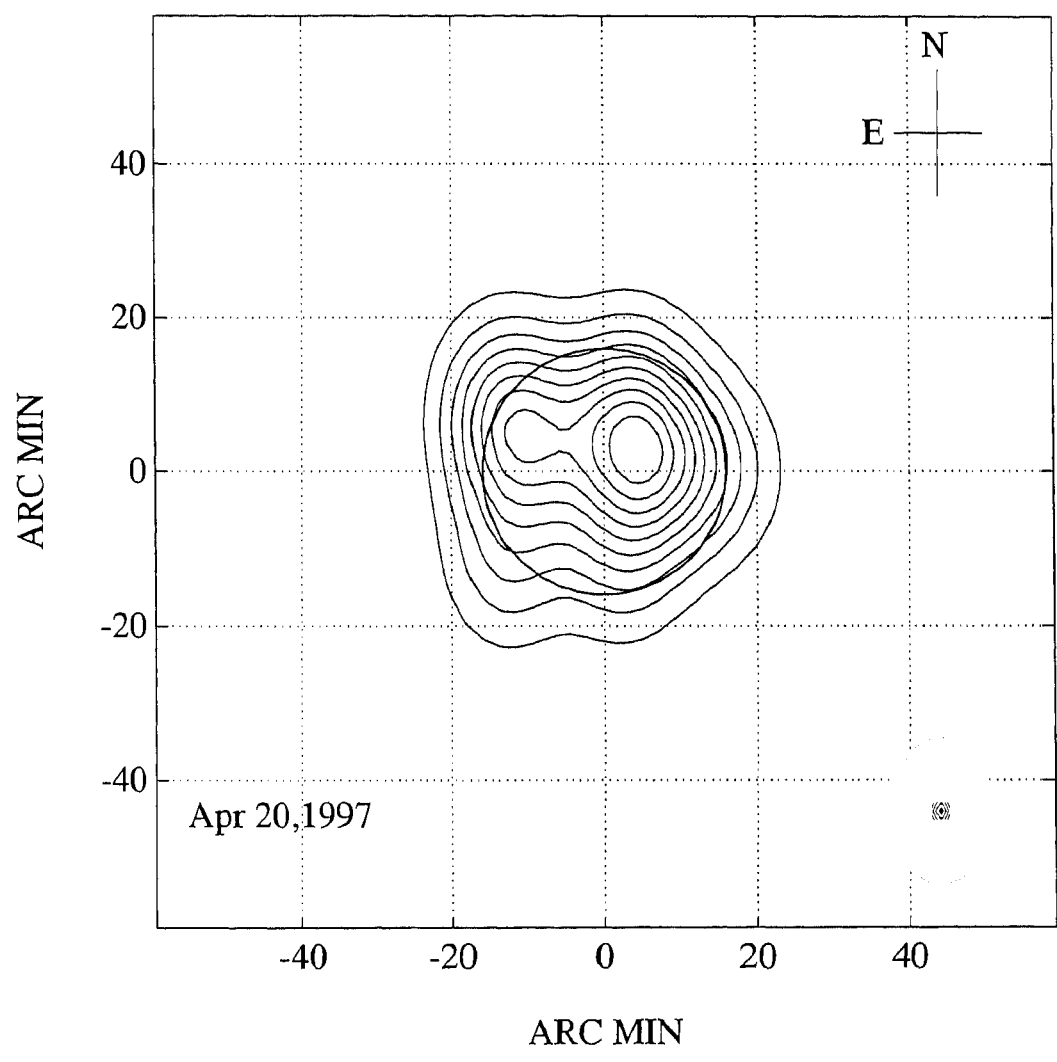


Figure 4.4: Map obtained by removal of phase errors using the values got by observing the radio source Virgo A.

GAURIBIDANUR RADIO HELIOGRAM - 75 MHz

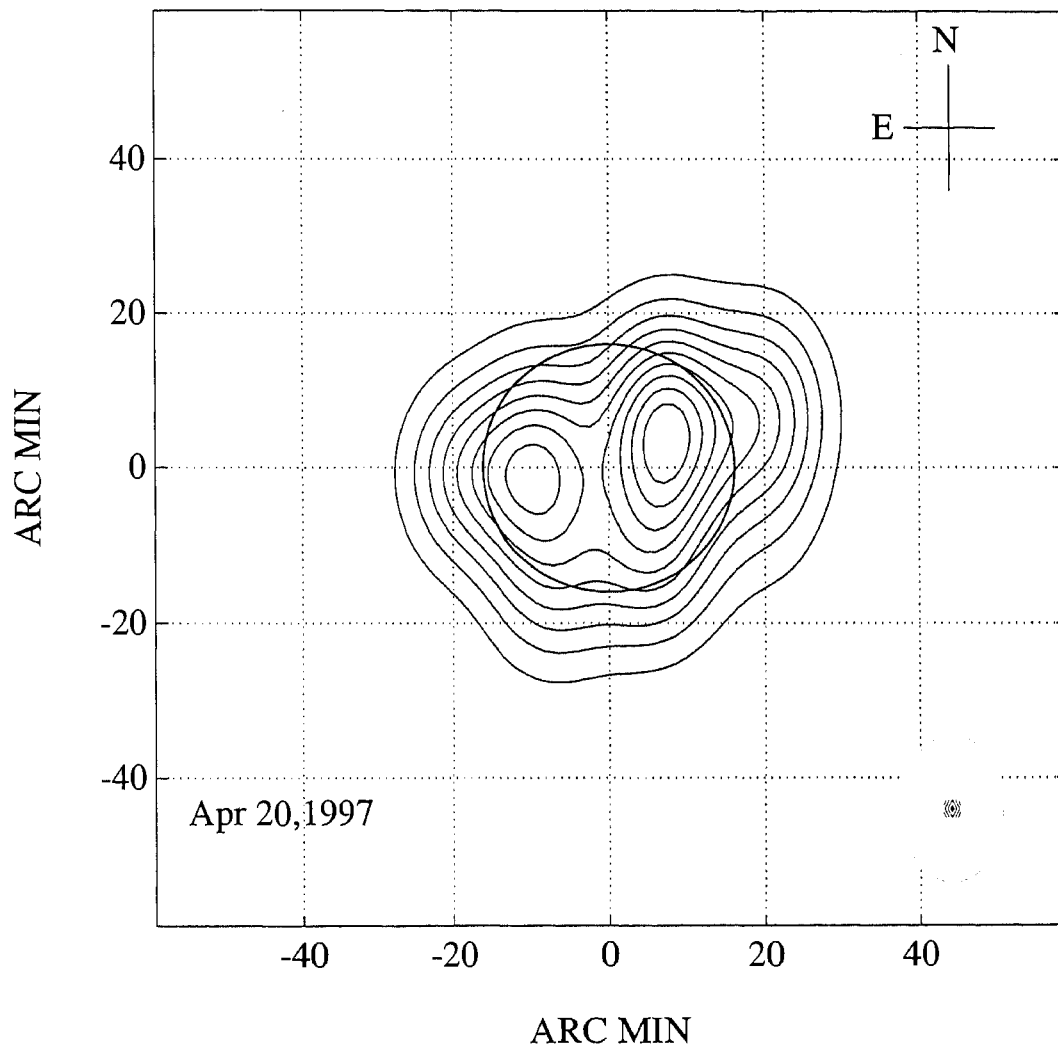


Figure 4.5: Map obtained by using self-calibration technique in AIPS.

Appendix C

Appendix

C.1 One-dimensional transform

As seen in Chapter 2, each antenna group in the E-W arm consists of 8 LPD's and the spacing (d) between them is 10 m. The response function (beam pattern) of each group along the right ascension (l -direction) is given by (Kraus, 1966)

$$p(\phi) = \frac{\sin(8\pi d_\lambda l)}{8 \sin(\pi d_\lambda l)} \quad (\text{C.1})$$

Along the declination (m -direction), the response function of each group is $\approx 100^\circ$ (just that of a single LPD). There are 16 such groups in the E-W arm and their phase centers are separated by 80 m (D_λ), except for G_8 and G_9 which are separated by 90 m (see Chapter 2). The combined pattern of these 16 groups is given by¹

$$P(\phi) = \frac{\sin(16\pi D_\lambda l)}{16 \sin(\pi D_\lambda l)} \quad (\text{C.2})$$

The net response of the E-W arm of the heliograph to any source will be the product of the above two patterns which are shown in Figure C.1. One

¹It is assumed that the error due to additional 10 meters spacing between the groups G_8 and G_9 is negligible.

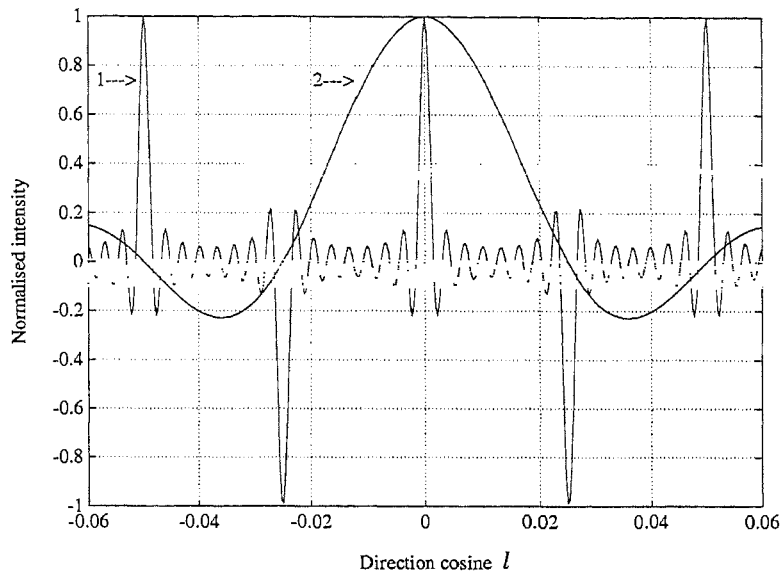


Figure C.1: E-W array synthesized beam (1) and E-W group beam (2) at $\lambda = 2$ m.

can see that except for the beam corresponding to $l = 0$, all the other peaks of the pattern of the E-W arm are located at the nulls of the E-W group beam. Hence there will be no confusion (in the form of contribution from other sources present at the location of these peaks) while imaging any source when it transits the instrumental meridian, i.e. when $l = 0$. But in off-transit mode, when l is changed to phase the array to the required direction, two peaks will be present inside the group beam at the same time and there can be aliasing effects if sources are present at the location of both the peaks. This may lead to errors in the synthesized map (Golap, 1998). So in the GRH, imaging is performed in the transit mode by using a one-dimensional transform along the m -direction. The aliasing problem will be present in the m -direction also, but its effect on the map will not be very severe, as the angular distance between the peaks is comparatively large.

Chapter 5

One-dimensional observations

5.1 Introduction

The slowly varying component (SVC) or the S-component is one of the important observational aspects of the radio emission from Sun, in relation to the understanding of the physical properties of the solar atmosphere. It is called the SVC because of the slow change from day to day of its intensity and position. It originates thermally in localized regions of high electron densities and magnetic fields that exist in the vicinity of sunspots and chromospheric plages. These regions are also called persistent sources, because of their persistence over several solar rotations. The importance of the study of the SVC arises in part from the fact that its measurements made simultaneously at different wavelengths can lead to a determination of physical parameters, notably electron densities and temperatures, in different layers of the solar atmosphere overlying active regions. The SVC has been observed over a wide range of wavelengths ($\lambda = 3$ mm to $\lambda \geq 10$ m), and its association with various optical features seems to depend on the wavelength of observation. In this chapter, we review the earlier observations on SVC

sources at meter-decameter wavelengths and then present the results obtained with the E-W arm of the Gauribidanur radioheliograph at 51 and 77 MHz. These observations were carried out before the GRH started operating in the two-dimensional mode.

5.2 Observations of SVC at meter-decameter wavelengths

In spite of nearly three decades of observations with one-dimensional interferometers and heliographs, the question of existence and origin of the SVC at meter-decameter wavelengths is not entirely settled. A first difficulty is that not all sources are of thermal origin, some of them being faint noise storms which are clearly non-thermal (Alissandrakis, Lantos and Nicolaidis, 1985). The discrimination between the two kinds is not always easy, but in general the noise storms are somewhat brighter, smaller in size and more variable than the thermal sources; in addition they are located close to but not directly above active regions with sunspots (Alissandrakis and Lantos, 1996). The existence of the SVC at meter wavelengths was first demonstrated by Moutot and Boischot (1961), using the E-W one-dimensional scans obtained with the Nancay interferometer at 169 MHz. According to them, the flux density of the bright regions (free of storm bursts) is highly variable and can reach values as high as 15 to 20% of the quiet Sun value. Also the apparent diameter of the sources is much larger than that on centimeter and decimeter wavelengths, being of the order of 10' to 20'. From the observed rotation rate, they estimated the altitude of these regions to be 0.25 R_{\odot} above the photosphere. They also pointed out that the meter wavelength sources do not seem to rotate like the sunspots or the bright regions seen in the centimeter

wavelength radio maps. But in a few cases, there was a close correspondence with the underlying regions at lower altitudes. The measured values of flux density and the diameter were proportional to each other, implying the constancy of the brightness temperature (T_b) of the emitting regions. Axisa et al. (1971) studied the behaviour of the SVC at 169 MHz using the data obtained with the Nancay E-W interferometer and pointed out that the SVC at meter wavelengths can be best explained in terms of thermal emission from the streamers. According to Newkirk (1967), these features occur away from active regions and generally overlie quiescent filaments (prominences) seen in the $H\alpha$ pictures. The estimated altitude of the SVC sources associated with the filaments was found to be $0.39 R_\odot$ above the photosphere. Dulk and Sheridan (1974), using the two-dimensional maps obtained with the Culgoora radioheliograph at 80 and 160 MHz pointed out that the temperature in the middle corona above the new, hot active regions must be approximately the same as the ambient corona. According to them, the brightest feature on their maps seems to lie directly above a quiescent filament, which was remote from active regions. The region was seen more prominently in the 80 MHz map compared to the 160 MHz map, with the observed T_b being 1.4×10^6 K at 80 MHz and 1.1×10^6 K at 160 MHz. It was shown by Sastry, Shevgaonkar and Ramanuja (1983) that the regions of enhanced emission seen in their maps obtained at 34.5 MHz with the Gauribidanur Decameter Wave radio telescope can be best explained in terms of thermal emission from regions of enhanced density ($\times 5$) and temperature ($\times 2.5$) w.r.t. the background corona.

Given the inherent problem in obtaining images with high angular resolution at long wavelengths, the best method for identifying the nature of the discrete sources is to get their spectral behaviour by comparing observations carried out at more than one frequency. Lantos et al. (1987) who compared

the maps obtained with the Nancay radioheliograph (NRH) at 169 MHz and those obtained with the Clark Lake radioheliograph (CLRH) at 30.9, 50.0 and 73.8 MHz, pointed out that the SVC at meter-decameter wavelengths appears to have its origin in more than one type of activity, contrary to those at centimeter and decimeter wavelengths. Though weak noise storm continua are the most frequent sources of the SVC at 169 MHz, they tend to disappear at lower frequencies. On the other hand, the contrast of thermal sources like the streamers is more at decameter wavelengths, since the variations in the optical depth can be prominently observed at these wavelengths.

A study of the variability of the SVC at meter-decameter wavelengths was carried out during the period of sunspot minimum by Shevgaonkar, Kundu and Jackson (1988) using the VLA data at 327 MHz and the CLRH data at 38.5, 50.0 and 73.8 MHz. They pointed out that although non-thermal emission mechanisms appears to support the variation in T_b over periods of less than 1 hr, they fail to explain the low values of observed T_b , i.e. $\leq 10^6$ K. On the other hand, the long-lasting SVC sources which overlie $H\alpha$ filaments are successfully explained by thermal models. On the basis of the observations carried out with the CLRH during the sunspot minimum period of September 1985, it was shown by Schmahl, Gopalswamy and Kundu (1994) that the discrete sources seen in their maps which moved slowly from one limb to the other were associated with coronal streamers. The average values of the observed T_b were 2.5×10^5 , 3.3×10^5 and 3.7×10^5 K at 38.5, 50.0 and 73.8 MHz respectively. It is possible that at meter-decameter wavelengths the relative importance of the different sources of the SVC may vary with the phase of the solar activity cycle. According to Bazelyan (1987), one has to carry out systematic observations during periods of suppressed activity to establish the nature of the SVC sources at decameter wavelengths. In the

following section, we present evidence for a close association between the SVC sources seen in the low frequency radio maps and the sunspot active regions using the data obtained with the E-W arm of the GRH and the SXR data obtained with the YOHKOH. From the observed rotation rate/day of the SVC sources seen in our maps, we also estimated their altitude above the photosphere. It must be pointed out that operation of the E-W arm of the heliograph in the one-dimensional mode gives a factor of 2 improvement in the resolution along the E-W direction, compared to the two-dimensional case (Christiansen and Högbom, 1969).

5.3 Observations with the GRH

The observations reported in this section were carried out during the sunspot minimum period of February, 1995. The E-W arm was divided into 8 groups of 16 elements each and the outputs of these groups were correlated in a 64 channel digital correlator. Phase corrected outputs from the 7 baselines were added together to synthesize E-W one-dimensional brightness distribution of the Sun at 51 and 77 MHz. On each day the observations were carried out for about 30 minutes around the local noon (± 15 minutes on either side of transit of the Sun over the local meridian at Gauribidanur), which is approximately 06:30 UT. The Sun was relatively quiet and no transient burst activity were seen in our data. The observations on the radio source 3C144 was used for calibrating the solar data. To remove the sidelobe contribution, the scans were CLEANed (Högbom, 1974) with the observed beam on a point source. From the observations made during the period Feb 20 to Feb 22, 1995, the presence of a discrete source of enhanced emission was noticed in our one-dimensional maps obtained at 51 and 77 MHz.

Figures 5.1 and 5.2 show the SXR pictures obtained with the YOHKOH on Feb 20 and 23, 1995 at 11:54:54 UT and 11:10:18 UT respectively. Our aim was to compare the maps obtained with the GRH and the SXR images for a study of the discrete source seen in our maps. Since the response pattern of the E-W arm of the heliograph is very broad in declination, it cannot resolve radio sources located at different solar latitudes, but which cross the meridian at the same time. Therefore one single region of enhanced emission may correspond to a superposition of several sources in declination. Because of this, the SXR images were integrated along the N-S direction and then compared with the GRH data. Figure 5.3 shows one such one-dimensional profile of the YOHKOH image obtained on Feb 20, 1995. The maps obtained with the GRH on the same day at 51 and 77 MHz is overplotted on the YOHKOH map. One can notice a close correspondence between the location of the active regions seen in the X-ray data and the enhanced emission in the radio data. This enhanced emission could be seen in the radio data obtained on the following days also (Feb 21 and Feb 22) and furthermore, the region of enhanced emission showed a regular rotation across the solar disk for a period of 3 days from Feb 20 to Feb 22 (Figure 5.4 and 5.5). On each day the location of the region of enhanced emission was established by taking the derivative of the observed data and noting where the derivative changes sign. Though we could unambiguously fix the location of the peak of the observed emission on Feb 20, 21 and 22 by this method, we could not clearly locate the peak of the observed emission on Feb 23. It is probable that the confusion is due to the appearance of another active region on the disk towards the east (Figure 5.2). From the location of the peak of the observed emission in the map obtained on successive days, the rotation rate/day of the region was calculated and the values are $\approx 5.5'$ at 77 MHz and $\approx 6.5'$ at 51 MHz. This difference in

the rotation rate is expected because of the difference in the height of the emissive region (Kundu, 1965). From the observed rotation rate/day of the persistent source, one can estimate its height above the photosphere by using the formula (Moutot and Boischot, 1961),

$$h = [\alpha \cos(L) d/\beta] - R_{\odot} \quad (5.1)$$

where h - Altitude of the active region above the photosphere (in kms)

α - Apparent rotation of the active center in 24 hours (in degrees), at a given frequency

L - Heliographic latitude of the active region (in degrees)

β - Rotation of the Sun in 24 hours ($\approx 13^{\circ}.2$)

d - Earth-Sun distance (15×10^7 kms)

R_{\odot} - Radius of the Sun (6.96×10^5 kms)

From the location of the active regions in Figure 5.1 and 5.2, the value of L was taken to be $\approx 20^{\circ}$. Substituting all the values in equation 5.1, the value of h in the present case was estimated to be $0.65 R_{\odot}$ at 51 MHz and $0.40 R_{\odot}$ at 77 MHz. Since the radiation at any given frequency originates at/or above the corresponding plasma level, the electron density can be estimated using the formula,

$$f_p = 9 \times 10^{-3} N_e^{1/2} \quad (5.2)$$

where f_p is in Hz and N_e in cm^{-3} . In the present case the density at heights $0.65 R_{\odot}$ and $0.40 R_{\odot}$ above the photosphere are $3.2 \times 10^7 \text{ cm}^{-3}$ and $7.3 \times 10^7 \text{ cm}^{-3}$ respectively. According to Newkirk (1961), the electron density in the solar corona at a distance ρ from the center of the Sun is given by,

$$N(\rho) = 4.2 \times 10^4 D 10^{4.32/\rho} \quad (5.3)$$

where $D = 0.1$ to 0.5 for a coronal hole, ≈ 2 for an active region, ≈ 10 for a dense streamer, and ≈ 1 for quiet corona (Thejappa and Kundu, 1992).

Figure 5.1: SXR image of the Sun obtained with YOHKOH on Feb 20, 1995 at 11:54:54 UT. North is straight up and East is to the left.

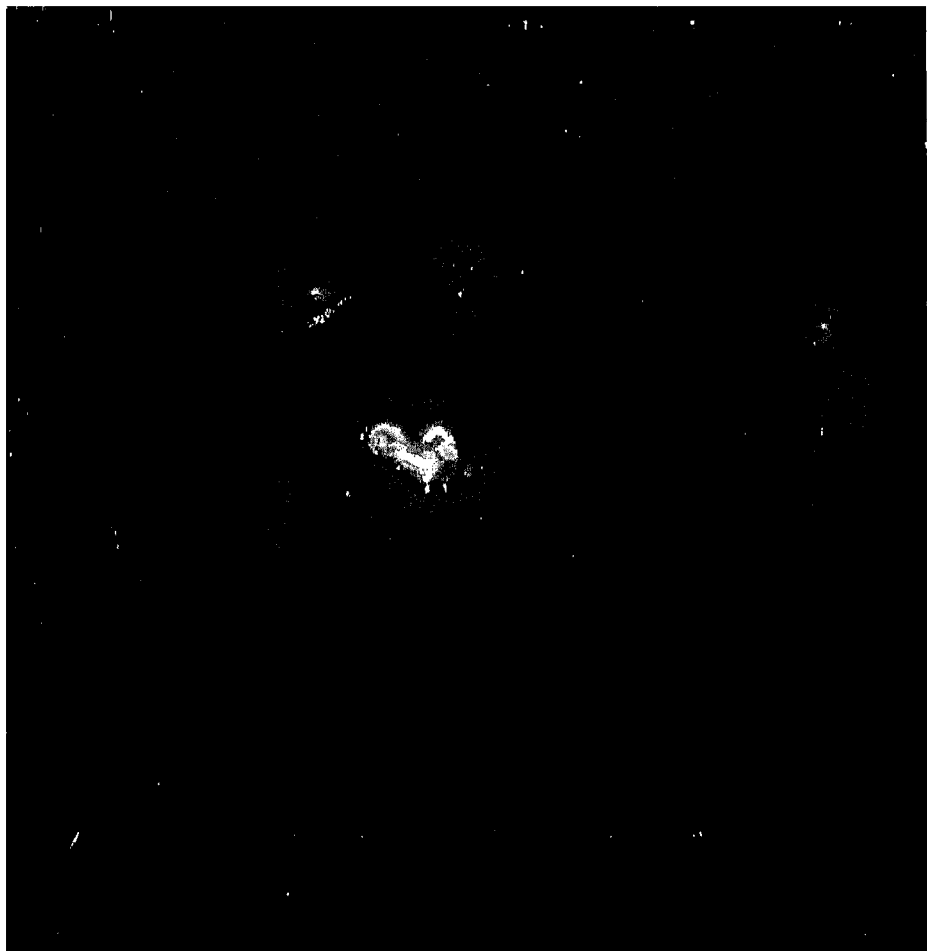
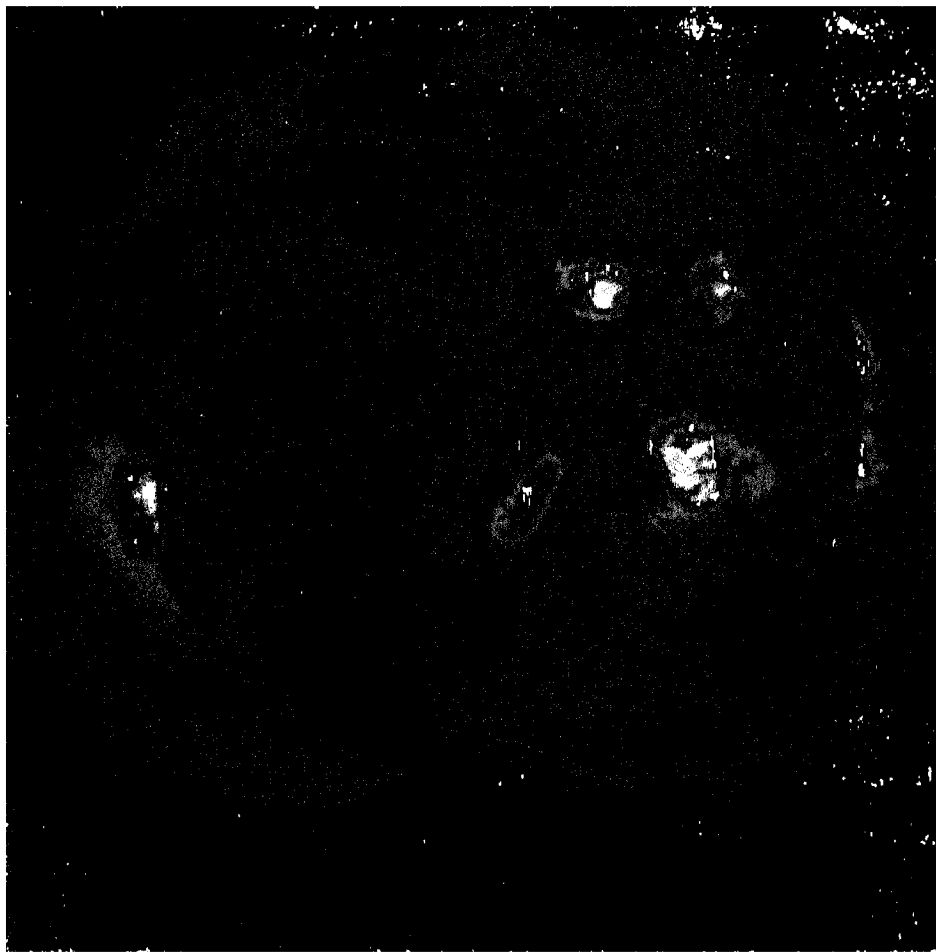


Figure 5.2: SXR image of the Sun obtained with YOHKOH on Feb 23, 1995 at 11:10:18 UT. North is straight up and East is to the left.



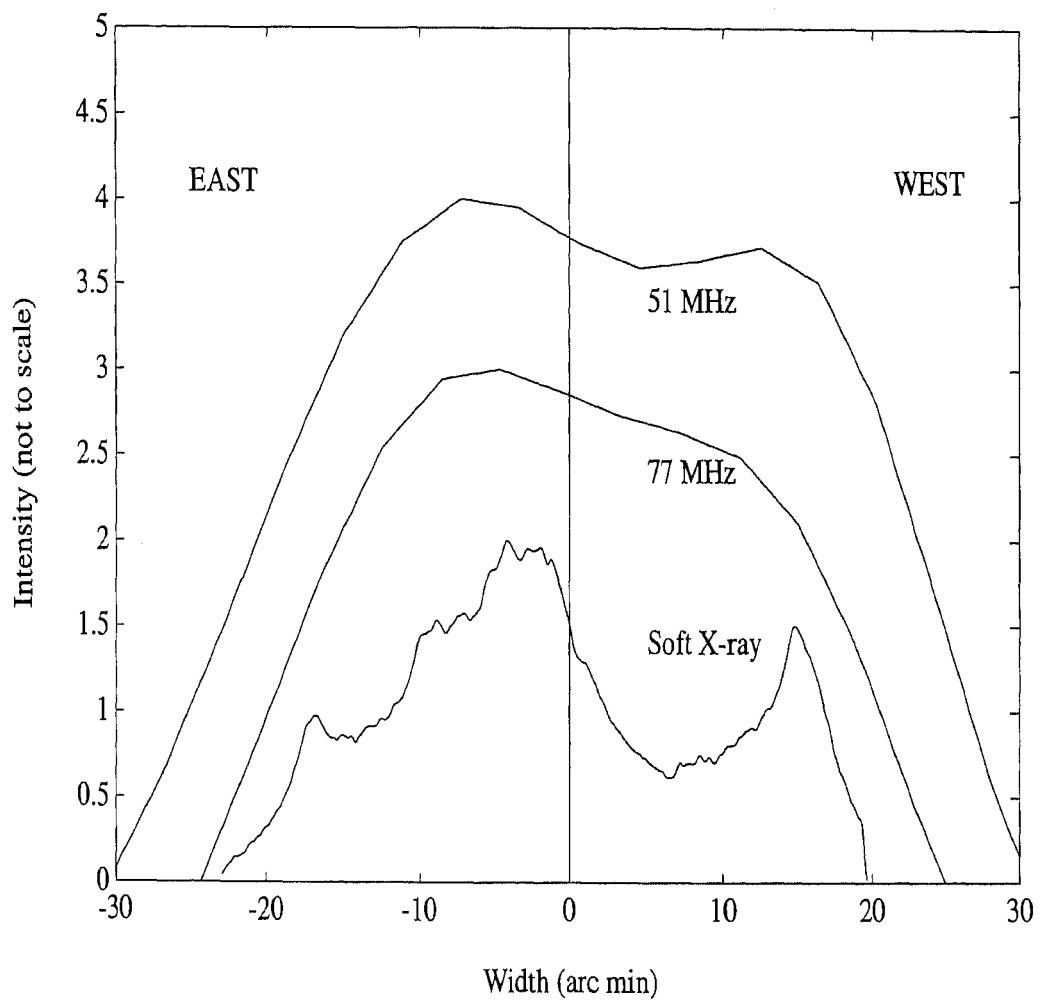


Figure 5.3: E-W brightness distribution of the Sun obtained with GRH and SXR telescope on board YOHKOH.

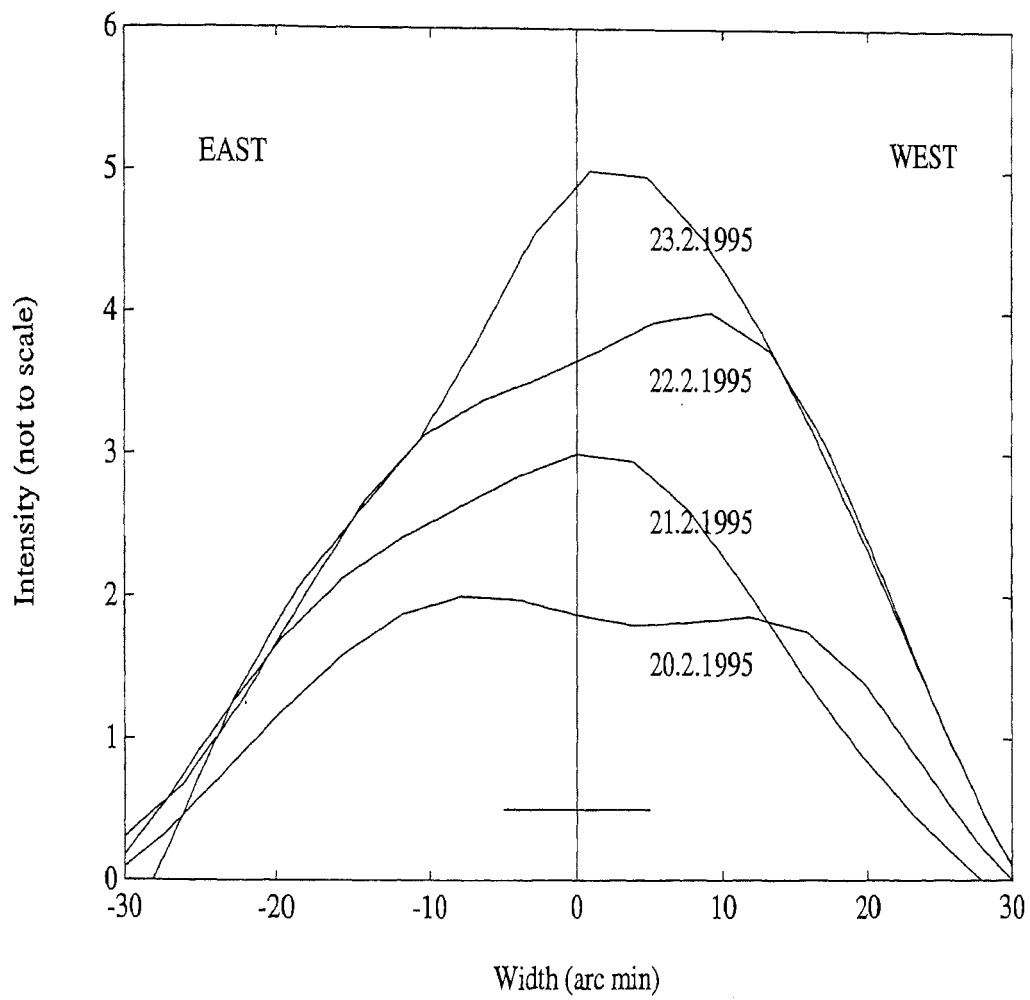


Figure 5.4: Observations of SVC at 51 MHz with the E-W arm of the GRH. The beam size is indicated by the horizontal line close to the abscissa.

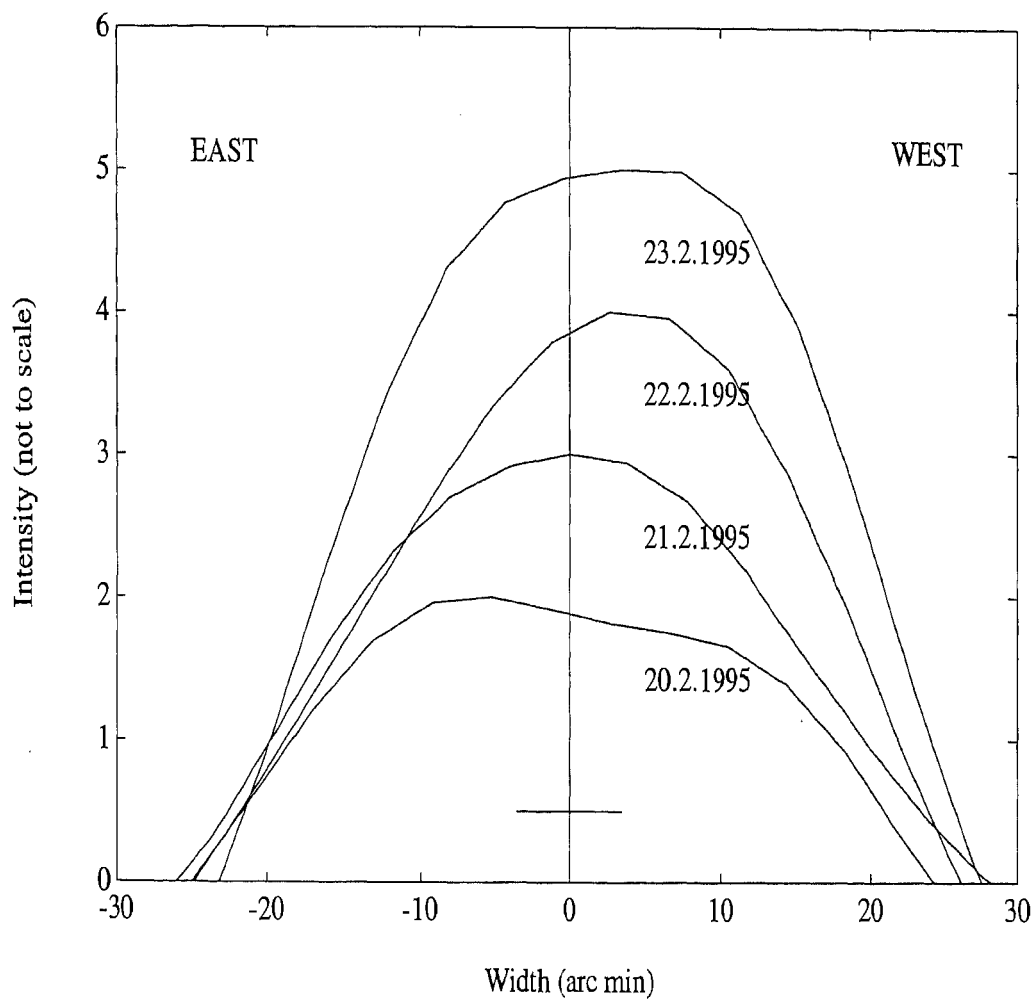


Figure 5.5: Observations of SVC at 77 MHz with the E-W arm of the GRH. The beam size is indicated by the horizontal line close to the abscissa.

Substituting for ρ in equation 5.3, the value of h estimated using equation 5.1, we get the same densities given by equation 5.2 only if we take the value of D as approximately 1.5 and 2 corresponding to 51 and 77 MHz. Therefore it is possible that the enhanced emission seen in our maps might be associated with the active regions seen in the SXR map.

Table 5.1 gives the integrated flux density (S) for each day at 51 and 77 MHz, and also the spectral index (γ) calculated using them. The errors in the estimation of the flux density are mainly due to: (1) the variation in the antenna gain with zenith angle, since the calibrator (3C144) and Sun were not at the same declination during our observational period. In the present case, this error was calculated to be approximately 10% based on the flux density measurements with the GRH of various point sources at different declinations; and (2) the uncertainty in the flux density of the calibrator which is approximately 5% (Nelson, Sheridan and Suzuki, 1985).

Date of observation	$S_{51 \text{ MHz}}$ (in Jy)	$S_{77 \text{ MHz}}$ (in Jy)	Spectral index γ
20.2.1995	4550	8325	1.47
21.2.1995	4490	11574	2.30
22.2.1995	4745	13135	2.47

Table - 5.1

5.4 Discussions and Conclusions

The present observations indicate the possibility of using multi-frequency radio imaging at meter-decameter wavelengths as an effective tool for estimating the electron density at various levels in the solar atmosphere independent of

any density models. In the past, several authors have established the association between meter wavelength sources with features such as weak noise storm sources lying above photospheric neutral line and streamers above $H\alpha$ filaments. But a regular rotation of the thermally emitting discrete sources that overlie active regions has not been reported so far at frequencies < 100 MHz. The GRH observations presented in this chapter seems to indicate that during quiet periods, it is possible to observe such sources provided no old/new sources appear on the disk in addition to the existing one under observation. As one can see from the map corresponding to Feb 23 in Figures 5.4 and 5.5, the regular movement of the existing region of enhanced emission suddenly disappears with the emergence from behind the limb of an old active region (Figure 5.2).

The possibility of non-thermal emission from weak noise storm sources, which is often suggested as being responsible for the slowly varying emission at meter-decameter wavelengths, can be ruled out in the present case because: (1) The emission from the noise storm sources is considered to be highly variable compared to the thermal sources (Alissandrakis and Lantos, 1996). From the quiet Sun observations at 34.5 MHz, it was pointed out by Sastry (1994) that in the presence of noise storm sources, the observed flux density varies by a factor of three from day to day. The constancy of the observed fluxes (within the error limits) in the present case indicate that there was not much of variability in the emission measure of the source region; and (2) No noise storms were observed during the above period with the Nancy radioheliograph at 164 MHz, except for a very weak one on Feb 20 (Solar Geophysical data, April 1995). The spectral indices shown in Table 5.1 also point to thermal emission. Except for a slightly smaller value on Feb 20, on the other days it remained approximately close to the value reported for thermal

emission from the solar atmosphere (Erickson et al. 1977; Subramanian and Sastry, 1988).

It has been suggested by many authors that streamers are the frequent sources of SVC at meter-decameter wavelengths. On the basis of Saito's (1972) density model for streamers and holes, Lantos et al. (1987), pointed out that the altitude of the streamer sources range from 1.1 to 2 R_{\odot} at 50 MHz and from 1.04 to 1.7 R_{\odot} at 73.8 MHz, depending on the density of the streamer. It is also well known that during sunspot minimum the streamers are mainly confined to the equatorial plane. But in the present case, the discrete source seen in our one dimensional maps are more likely to be associated with active regions rather than streamers because, (1) there is a close positional correspondence between the active regions in the SXR images and the peaks in the radio maps and (2) the streamer sources clearly stand out against the background corona in the low frequency (< 100 MHz) radio maps only if the density inside them is ≈ 10 times greater than that of the ambient (Schmahl, Gopalswamy and Kundu, 1994). Contrary to this, the value of the density enhancement factor derived from our observations is only ≈ 2 .

In this connection we would also like to point out that the possibility of observing the thermal counterparts of the sunspot associated active regions is generally more at decameter wavelengths than the meter or decimeter wavelengths since the contrast of the thermal sources w.r.t. the ambient medium will be more at longer wavelengths as pointed out earlier. We present further observational evidence for this by comparing the radio maps obtained with the GRH at 75 MHz, NRH at 164 MHz and the soft X-ray image obtained with the YOHKOH. Two-dimensional pictures bring out the positional correspondence between the features without any ambiguity. Figure 5.6 shows the map obtained with the GRH at 75 MHz on July 30, 1997 at 06:30 UT.

One can clearly see the existence of two discrete sources on either side of the central meridian. The measured T_b of both the sources were $\approx 0.5 \times 10^6$ K. This implies that the sources are thermal in nature. Also no non-thermal radio bursts were observed either prior to or after our observations (Solar Geophysical Data, September 1997). Figure 5.7 shows the map at obtained with the NRH at 09:37:22 UT on July 30, 1997 at 164 MHz. One can see that the features in the two radio maps (Figure 5.6 and 5.7) do not agree well with each other. But there is very good correspondence between the 75 MHz radio map and the soft X-ray image as one can see from Figure 5.8 where the radio map in Figure 5.6 has been overlaid on the YOHKOH soft X-ray image taken at 05:29:37 UT on the same day. On the basis of this and the observed T_b of the two sources from the GRH map, one can conclude that the lack of correlation between the 75 and 164 MHz maps is probably not due to the time difference between them or the height difference of the emissive regions (164 MHz corresponds to a critical density of $\approx 3.3 \times 10^8 \text{ cm}^{-3}$ while 75 MHz corresponds to $\approx 6.9 \times 10^7 \text{ cm}^{-3}$). It has also been pointed out earlier by Lantos and Alissandrakis (1994) that generally there is no thermal radio counterpart around 160 MHz of active regions with sunspots. These results show the importance of long wavelength observations in relation to the study of thermal radio emission from sunspot associated active regions.

GAURIBIDANUR RADIO HELIOGRAM - 75 MHz

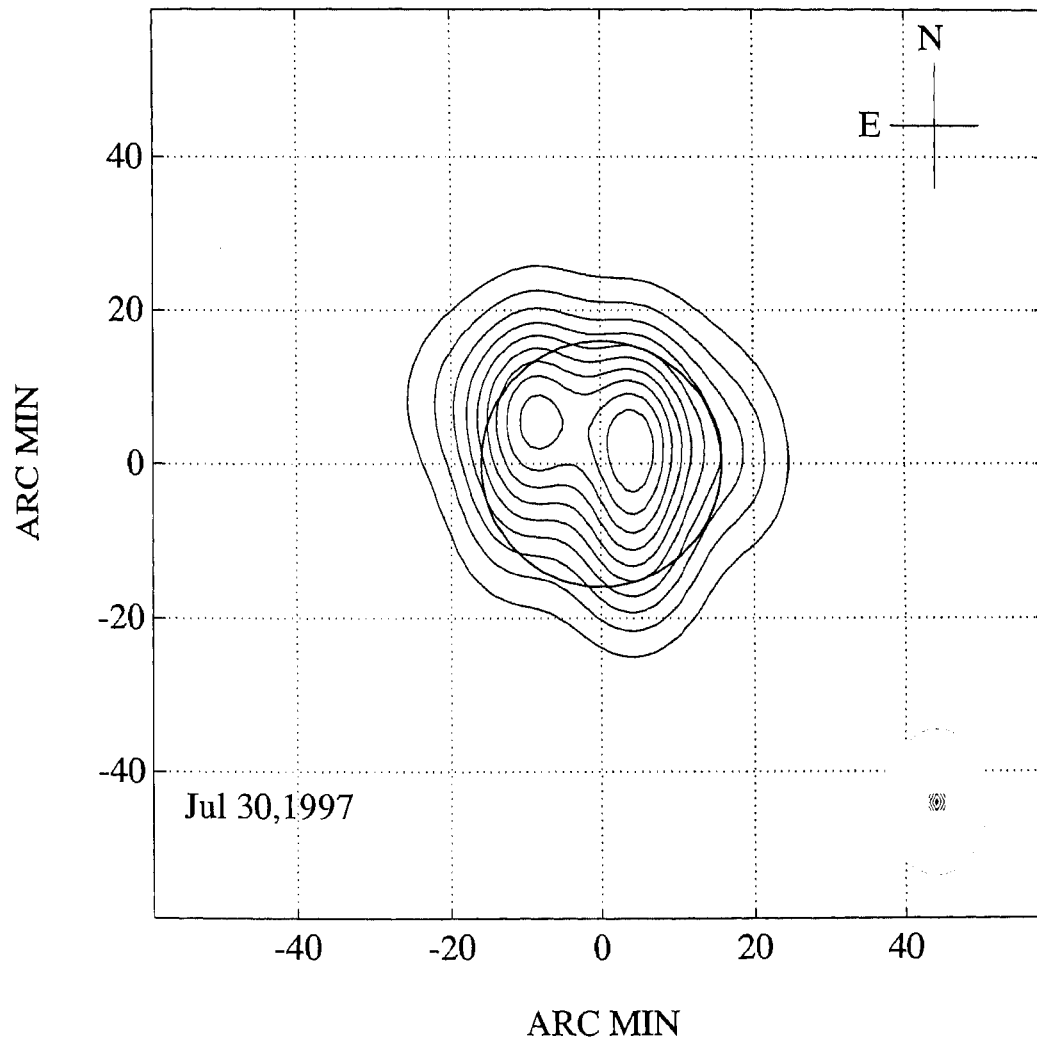


Figure 5.6: Map obtained with the GRH at 06:30 UT.

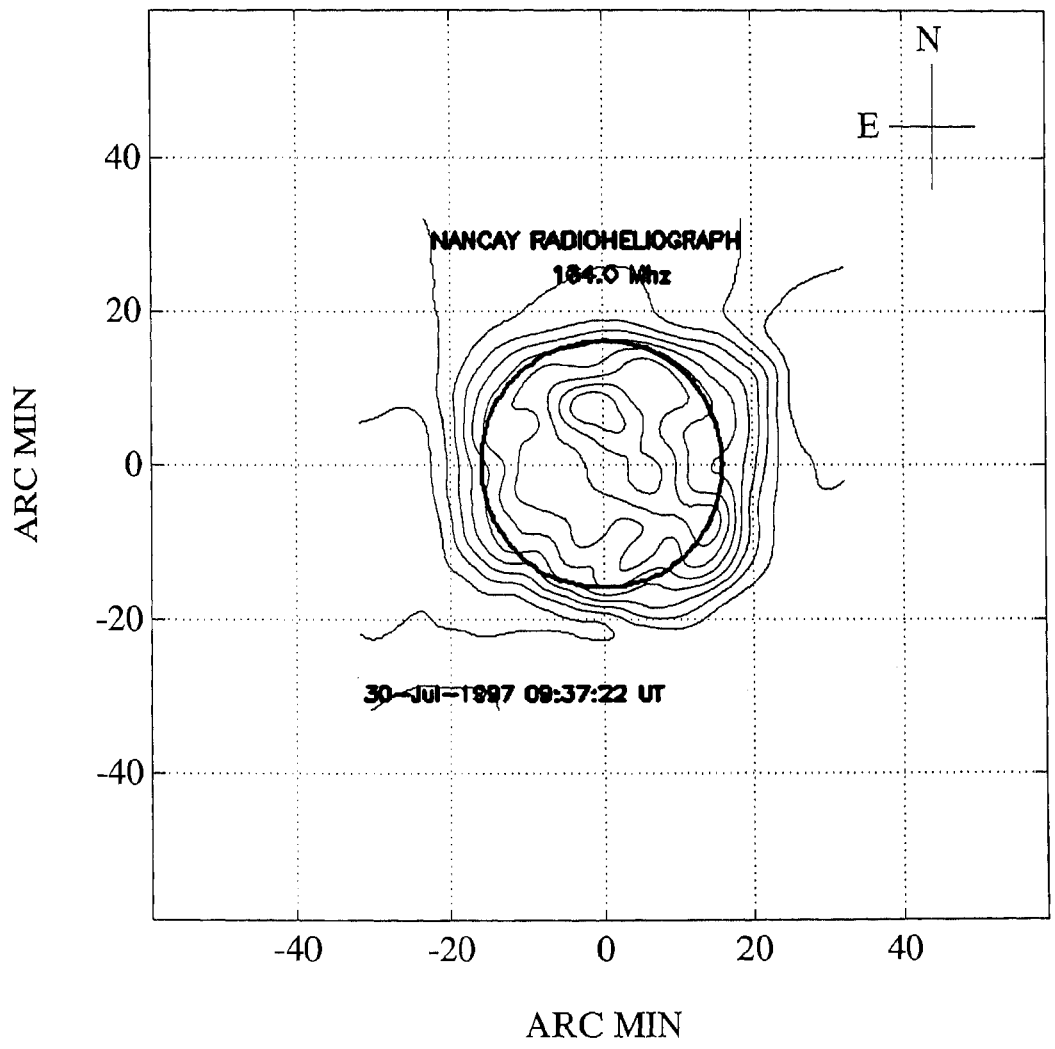
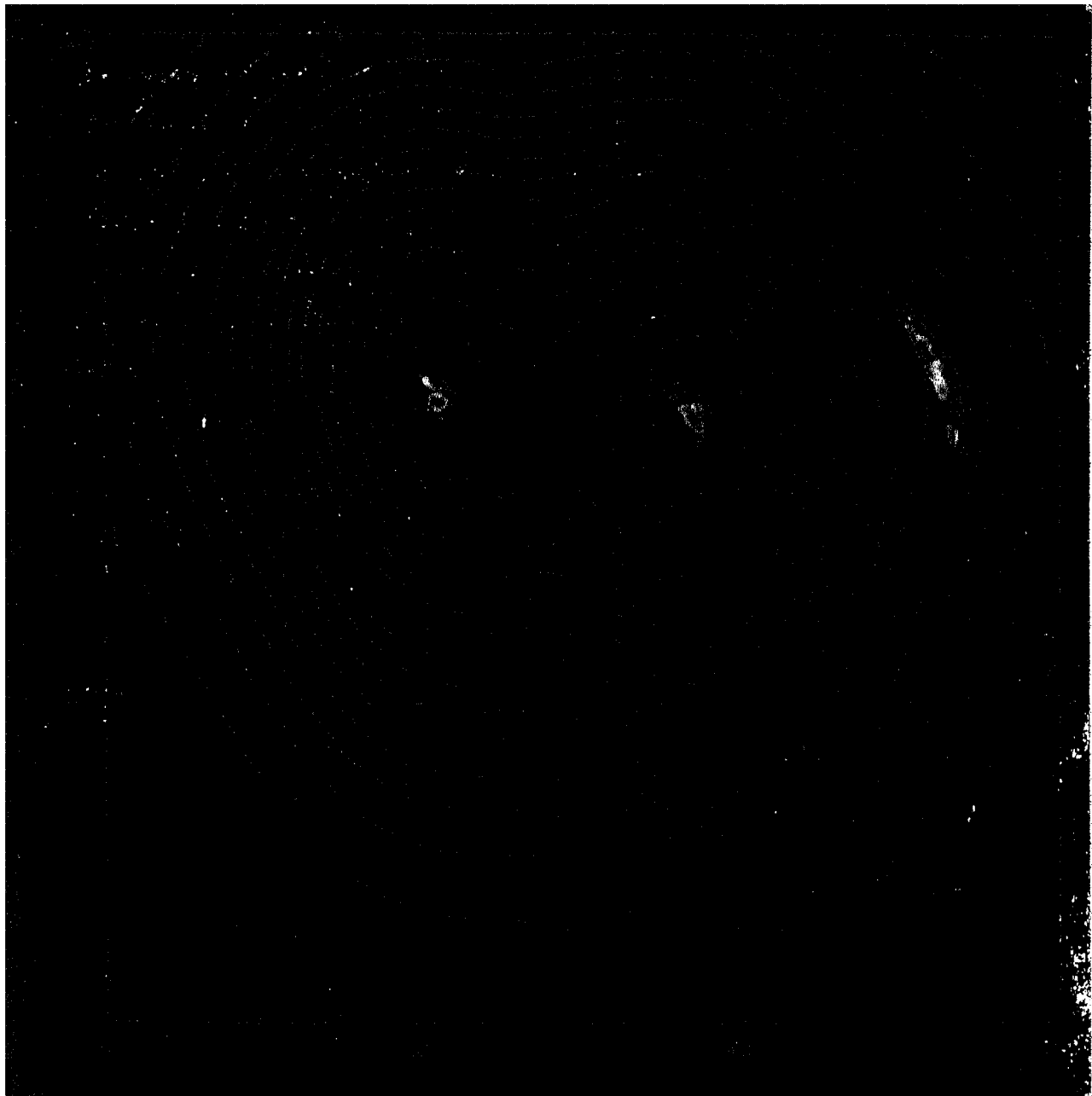


Figure 5.7: Map obtained with the NRH at 09:37:22 UT.

Figure 5.8: Radio map in Figure 5.6 overlaid on the YOHKOH soft X-ray map obtained on the same day at 05:29:37 UT. North is straight up and East is to the left.



Chapter 6

‘Quiet Sun’ at meter-decameter wavelengths

6.1 Introduction

The basic problems of solar physics are those that are connected with the structure of the solar atmosphere, the physical nature and origin of transient phenomena, and the relation of solar activity to terrestrial events. All these problems are mutually connected; none of them can be considered independent of others. As a matter of convenience, however, the problems under attack may be arranged roughly in the following three groups: (1) the structure of the interior, (2) the structure of the atmosphere, and (3) the nature and origin of transient solar phenomena and activity, including solar-terrestrial relationships. In this chapter, radio observations of the solar atmosphere in the altitude range $0.1 - 0.6 R_{\odot}$ above the photosphere, are presented.

The radiation from the solar atmosphere can be broadly classified into those that relate to the “undisturbed” and to the “disturbed” Sun. In the former, the Sun is viewed as a static, spherically symmetric ball of hot

gases, whose properties change only with radius and are uniform over any one spherical layer. At any given time, the state of Sun's atmosphere can be described by a set of average physical conditions, such as temperature and density. In contrast, the radiation from the "disturbed" Sun originates in discrete, localized regions that exhibit significant departures from the average conditions. These regions are grouped together under the heading of 'active centers'.

The radio emission from the undisturbed Sun consists of two components: (1) A steady background component or the *quiet Sun* component which occurs in the absence of any localized sources (sunspots, plages, active regions, filaments, prominences and transient disturbances such as flares) on the Sun and (2) The *slowly varying component* which originates from high density regions of the corona called 'coronal condensations'. These regions overlie sunspots and plages. The intensity of the radiation changes slowly from day to day and has a period of about 27 days.

The "quiet Sun" - the Sun without any visible active center - is well defined in optical astronomy. But its definition in radio astronomy is rather unclear. During minimum of the sunspot cycle, when no active center is present on the disk, the radio emission can be considered as that from the quiet Sun. But during sunspot maximum, one must separate the slowly varying emission of the active centers from the quiet Sun emission. At meter-decameter wavelengths one should also take care of the intense non-thermal emission from the active centers (noise storm and burst sources) which dominate that from the quiet Sun. Consequently, at these wavelengths the method of finding the basic component from observations of flux density consists in finding the level to which the flux density often falls and below which it never falls (Pawsey and Yabsley, 1949).

6.2 Thermal emission from the ‘quiet’ Sun

There are good reasons to believe that the radio emission from the quiet Sun is thermal. Outside of the active regions, the plasma frequency is much greater than the gyrofrequency and therefore, the radio brightness arises entirely from thermal bremsstrahlung due to electron-ion collisions in the ionized plasma. Gyroresonance emission requires fairly strong magnetic fields which are not likely to exist in quiet regions (Alissandrakis, 1994). Also, the observed variation of temperature with wavelength is consistent with thermal emission from free electrons in the solar atmosphere. Hence measurements of the radio emission from the quiet Sun can provide information on the kinetic temperature and shape of the corona; further, in combination with the optical data, they can provide information on the electron density in the solar atmosphere. It is well known that the radio waves from the solar atmosphere at any particular wavelength, can originate only above a certain critical altitude. For example, the millimeter wavelength radiation originates in the lower chromosphere, centimeter wavelengths in the middle and upper chromosphere, decimeter wavelengths in the transition region, meter wavelengths in the inner corona and decameter wavelengths in the outer corona. Thus, by carrying out observations at different wavelengths, one can obtain information on the density, temperature and magnetic field as a function of height in the solar atmosphere.

Though the brightness distribution of the continuum radio emission from the quiet Sun has been studied in great detail at millimeter and centimeter wavelengths with high resolution for several decades, at meter and decameter wavelengths, there have been only a very few measurements. The main reason for this is the lack of radio telescopes with sufficient resolution and sensitivity at long radio wavelengths. In addition, the observations of the quiet Sun at

these wavelengths are limited by the fact that the emission is much weaker in comparison with that due to the intermittent burst activity; this requires either an instrument with a very large dynamic range or observations during periods of reduced activity. It is ideal to observe the Sun during the minimum phase of the solar cycle when the effects of the past or the precursors of the future disturbances (active regions) are assumed not to affect the quiet Sun radio emission. Finally, the observations of coronal emission at wavelengths greater than approximately 2 m are of considerable importance, since they provide information on the outer corona/interplanetary medium.

The appearance of the corona changes with wavelength due to opacity and refraction effects. As one moves towards longer wavelengths, the optical depth increases due to the growth of the absorption coefficient which is proportional to the square of the wavelength. At the same time, the frequency gets closer the plasma frequency of the medium, the index of refraction approaches zero and the rays eventually suffer total reflection (Alissandrakis, 1994). Due to the radial and azimuthal variations of the electron density (consequently the radio refractive index) ray trajectories have to be computed to obtain the integrated optical depth in any direction (Smerd, 1950; Bracewell and Preston, 1956). According to Newkirk (1961), the electron density in the solar corona at a distance ρ from the center of the Sun is given by,

$$N(\rho) = 4.2 \times 10^4 D 10^{4.32/\rho}$$

where $D = 0.1$ to 0.5 for a coronal hole (CH), ≈ 2 for an active region, ≈ 10 for a dense streamer, and ≈ 1 for quiet corona. Figure 6.1 shows the variation of the optical depth and the brightness temperature (for the central ray) in the outer corona as a function of frequency.

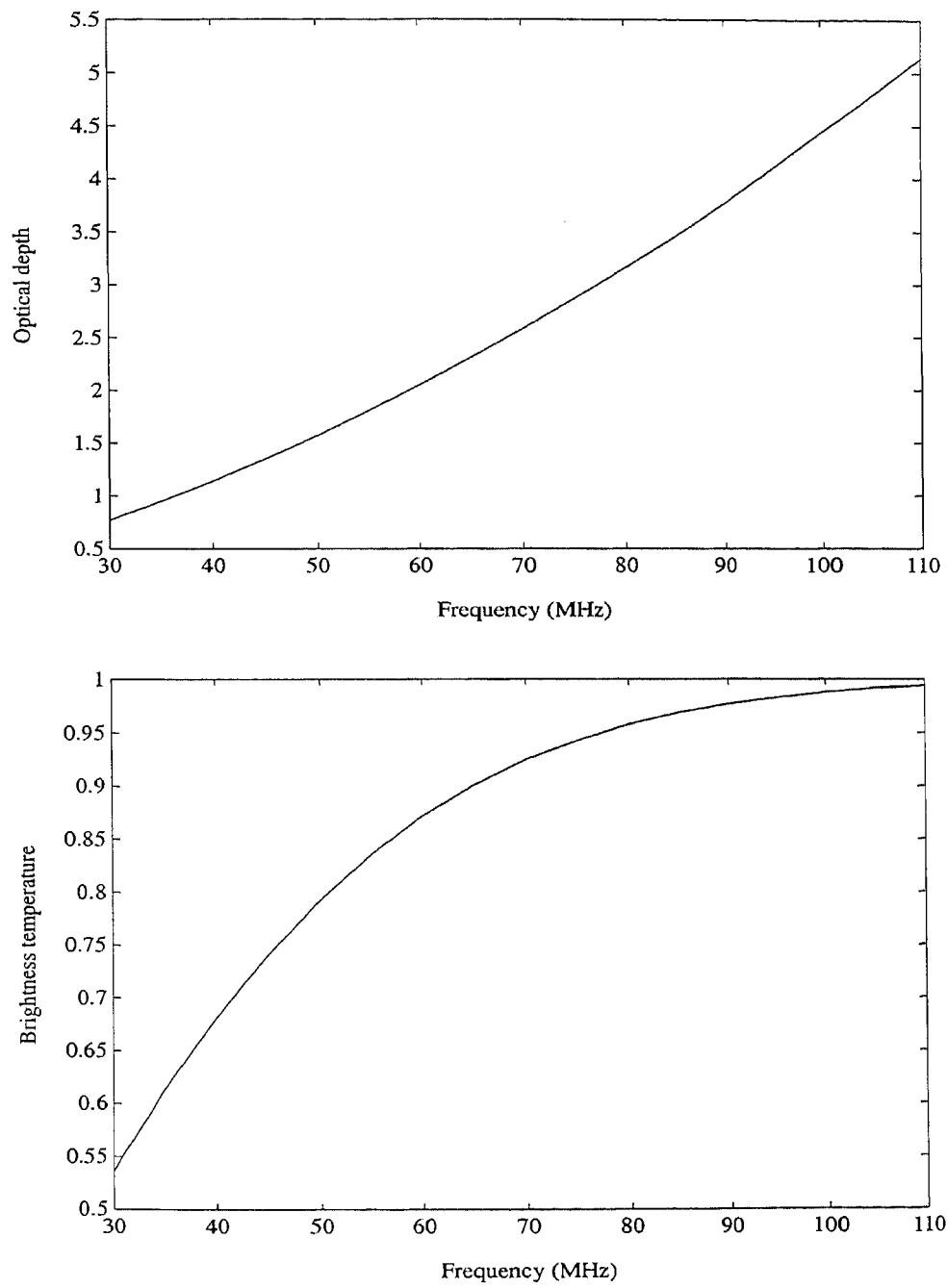


Figure 6.1: Variation of optical depth and brightness temperature with frequency, using Newkirk's density model with $D = 0.5$ and $T_e = 10^6$ K.

The brightness temperature (T_b) was calculated using the equation,

$$T_b = T_e (1 - e^{-\tau}) \quad (6.1)$$

and the optical depth τ using the equation,

$$\tau = \int_0^s K ds \quad (6.2)$$

The integration is carried over the total path length (s) travelled by the ray. The absorption coefficient (K) per cm of path length is (Thejappa and Kundu, 1992),

$$K = \frac{0.16 N_e^2}{n f^2 T_e^{3/2}} \quad (6.3)$$

where the refractive index n is given by,

$$n = 1 - \frac{f_p^2}{f^2} \quad (6.4)$$

Here f is the observing frequency and f_p is the plasma frequency of the medium. The ray tracing computations were performed for an uniform coronal temperature of $T_e = 10^6$ K. The value of D was taken as 0.5 since during sunspot minimum, the electron density of the corona is half of that during the maximum (Thejappa and Kundu, 1994). Our calculations and those of others (Sheridan and Dulk, 1980; Thejappa and Kundu, 1992), indicate that at wavelengths ≤ 7.5 m, the optical depth of the corona above the plasma level¹ corresponding to any particular wavelength is greater than unity. Therefore, the measured values of the brightness temperature should approach the electron temperature of the medium (equation 6.1). But the observed values of T_b in the last two decades at various wavelengths in the meter-decameter range have always been low (Sheridan, 1970; Aubier, Leblanc and

¹It is also called the critical level or critical layer, since the radiation originating below this level cannot reach the observer.

Boischot, 1971; Erickson et al. 1977; Sastry et al. 1981; Sastry, Shevgaonkar and Ramanuja 1983; Thejappa and Kundu, 1992). Also, the observed peak brightness temperature varies by a factor of more than three, even during periods when the Sun was quiet and free of any sunspots (Thejappa and Kundu, 1992; Sastry, 1994). To explain these observed results, several possibilities based on the effects of refraction on the radio wave propagation through the solar corona, have been suggested in the literature. These may be separated into various classes according to the scale size of the density structures involved.

6.2.1 Scattering

It is widely believed that small scale inhomogeneities (or ‘ripples’) in the electron density distribution in the solar corona cause scattering of radio waves with frequencies less than 100-200 MHz. By scattering we understand the process of random changes in direction which a ray suffers on passing through an inhomogeneous corona. According to Fokker (1965), the deviations in the ray path because of scattering, are much larger compared to that due to the regular variation because of the density gradient in the corona. Also due to scattering, the rays get reflected well above the critical level corresponding to the observing frequency. The optical depth is consequently reduced since most of the contribution to the absorption coefficient comes from regions very close to the critical level, where $f = f_p$ and $n = 0$ (Sheridan and McLean, 1985). Since the emissivity decreases with height, the observed flux also decreases in the presence of scattering (Aubier, Leblanc and Boischot, 1971). It is also obvious that the diameter of the radio Sun should depend on the amount of scattering. The effect of scattering by an irregular corona leads to a decrease in the observed flux density and an increase in

the size of the source, as compared to the values obtained without scattering (Steinberg et al. 1971; Aubier, Leblanc and Boischot, 1971). Consequently, the observed T_b should be reduced, since by Rayleigh-Jeans law,

$$T_b = \frac{S\lambda^2}{2k_B\Omega} \quad (6.5)$$

where S is the observed flux density, Ω is the solid angle subtended by the source and k_B is the Boltzmann constant. Therefore, if scattering is present, the observed values of flux density and the source diameter should be inversely related. On the other hand, if there is no scattering or if its effects are not much pronounced, the above two quantities should be directly proportional to each other, for constant T_b . The effect of scattering is controlled by the parameter (Steinberg et al. 1971),

$$\delta = \epsilon^2/h \quad (6.6)$$

where $\epsilon = \Delta N_e/N_e$ is the r.m.s. fluctuation of the electron density, and $h = 5 \times 10^{-5} R_\odot$ is the size of the inhomogeneities. Aubier, Leblanc and Boischot (1971) measured the quiet Sun brightness distribution with the Arecibo radiotelescope at three different frequencies (60, 36.9 and 29.3 MHz), and showed that the low values of T_b observed by them can be explained by invoking scattering of radiation by density inhomogeneities of 2% relative fluctuation level ($\epsilon = 0.02$). These observations were carried out during July-August, 1970 which was close to the sunspot maximum. The lowest ever values of T_b of the quiet Sun at long wavelengths have been reported by Thejappa and Kundu (1992). They estimated the T_b of quiet Sun during the period of sunspot minimum (September, 1986) using the observations carried out with the Clark Lake radioheliograph (CLRH) at 73.8, 50.0 and 38.5 MHz. The measured values were in the range, $0.6 \times 10^5 - 2.5 \times 10^5$ K at all the above three frequencies. According to them, ϵ should be in the range from 0.07 to 0.19, 0.1

to 0.25 and 0.15 to 0.35 respectively at 38.5, 50.0 and 73.8 MHz to explain the observed low brightness temperatures. Since these values of ϵ are much larger compared to that used by Aubier, Leblanc and Boischot (1971), they pointed out that the r.m.s. level of the density inhomogeneities in the corona may be more during sunspot minimum than maximum. Apart from the thermal radiation, some of the observed properties of the non-thermal emission from the corona has also been attributed to scattering. According to Steinberg et.al. (1971), the interpretation of center-limb behaviour of the type I and III bursts at meter wavelengths requires the use of non-spherical models for the electron density distribution and/or the distribution of inhomogeneities.

Though ray tracing models based on scattering theory satisfactorily explain the observed features of the radio emission from the solar corona, the importance of scattering has been questioned by several authors on various grounds. According to Trottet and Lantos (1978), it is not necessary to introduce scattering effects in order to explain the variations in the observed quiet Sun diameter. The expected enlargement of the Sun due to scattering, computed by McMullin and Helfer (1977), is of the same order or lesser than the half-power beam widths of the Culgoora and Clark Lake radioheliographs, which were in operation at that time. Subramanian and Sastry (1988) have pointed out that the amount of scattering ($\epsilon = 0.02$) used by Aubier, Leblanc and Boischot (1971) is not sufficient to explain the very low brightness temperatures of $< 0.2 \times 10^6$ K observed by Sastry, Shevgaonkar and Ramanuja (1983) and later by Wang, Schmahl and Kundu (1987). The use of higher values of ϵ has been questioned by Jackson, Sheridan and Dulk (1979); Sastry (1994). According to the computations of McMullin and Helfer (1977), an increase in the value of ϵ from 0.01 to 0.024 itself will lead to a 75% increase in the size of the radio Sun. Given this situation, the average

value of $\epsilon = 0.1$ used by Thejappa and Kundu (1992) should lead to a very large increase in the size of the radio Sun, which is obviously unrealistic. Also, since the variations in T_b are strongly correlated at all the three frequencies, they probably must have some other common origin. According to Sastry (1994), since scattering increases the size of the radio Sun, there must be a correlation between the variations in the T_b and the half-power widths of the brightness distribution, observed over a period of time (when the Sun is quiet). But, such a correlation was not present in the 34.5 MHz data obtained by him, using the large decameter-wave telescope at Gauribidanur. McMullin and Helfer (1977) also noted that the scattering models cannot explain some of the quiet Sun observations at frequencies < 200 MHz.

Though the scattering theory gives a plausible explanation for the apparent height and size of the sources, it fails to account for other observed effects like the directivity of Type I bursts (McLean and Melrose, 1985). Observations of point sources of sizes less than that predicted by the scattering theory have been reported by Kerdraon (1979). He has noted that, more than scattering, the sensitive parameters that are to be revised to explain the observations are the spherically symmetric density models and the altitude of the emitting regions. Some models of the corona (Bougeret and Steinberg, 1977; Duncan, 1979; Robinson, 1983) postulate a fibrous medium in which the radio emission can be ducted to higher levels than its point of generation before escaping. These models are successful in explaining the directivity, size and shape of the radio bursts. One has to see whether these models can be extended to the thermal emission from the quiet Sun. It is therefore clear that the consequences of scattering on the radio emission from the solar corona are not well understood at the present time.

6.2.2 Coronal streamers

It is generally believed that the shape of the solar corona depends on the phase of the solar cycle, i.e. near-circular during maximum with streamers extending outward radially from all latitudes, and elliptical during solar minimum, when the streamers are more concentrated along the equatorial plane (Sheridan, 1978; Sheridan and McLean, 1985). But according to Thejappa and Kundu (1994), the shape of the radio Sun at meter-decameter wavelengths is not a function of the phase of the solar cycle. The radio Sun can take elliptical as well as a spherical shape during a spotless minimum period itself, depending on the position of the streamers. Therefore, the E-W and N-S diameters can vary widely. Consequently there can be variations in the observed T_b also. Trotter and Lantos (1978) have shown that the observations of the Sun at decameter wavelengths are more likely to be interpreted in the frame of coronal structures such as streamers, holes, arches, etc., than by introducing scattering effects of coronal inhomogeneities. Since the density gradient in the solar atmosphere gets altered in the presence of these structures, the emergent radiation is critically dependant on the refraction effects. It was also pointed out by Borkowski (1982) that the large scale structures in the solar atmosphere possess different physical properties and they contribute in an unknown and variable proportion to the total radio flux of the quiet Sun. Sastry, Shevgaonkar and Ramanuja (1983) had shown that the low values of T_b ($\approx 0.3 \times 10^6$ K) at the disk center in their 34.5 MHz maps, can be explained in terms of thermal emission from regions of enhanced density and temperature located at distances of 1.5 to 2 R_\odot from the center of the Sun. A similar conclusion was reached by Thejappa and Kundu (1994) using the multi-frequency data obtained with CLRH. According to Alissandrakis (1994), density enhancements (streamers) will appear as regions of increased

brightness, provided the ambient corona is optically thin and/or the streamer has a higher temperature. They are better visible at longer wavelengths and far from the disk center. While the streamers at the center of the disk may be removed by the lower envelope method (Kundu, Gergely and Erickson, 1977), it is difficult to remove their contribution when they are at the limb. Theoretical computations (Riddle, 1974) without scattering show that at 40 MHz, the enlargement of the diameter of the Sun due to streamers, when they are at the limb, may be as large as one solar radius. So, it is probable that the meter-decameter wavelength radio emission is considerably influenced by the presence of streamers.

6.2.3 Coronal holes

Till 1970, the picture of the quiet corona was that of a single region with density and temperature varying with the solar cycle. But the discovery of the CHs in the early 70's lead to a complete revision of the classical picture of the corona. The first radio identification of CHs was obtained by Dulk and Sheridan (1974). In the two dimensional radio maps obtained at 80 and 160 MHz with the Culgoora radioheliograph, the holes appeared as regions of reduced brightness ($\approx 20\%$) compared to the average regions outside. It was argued that the turning point for the rays inside the hole is located at the chromospheric level and consequently the observed T_b of the hole is less than the ambient corona. They estimated the T_b inside the hole at 80 MHz to be $\approx 0.8 \times 10^6$ K. A similar value was obtained by Lantos and Avignon (1975) for the central brightness temperature of the truly quiet Sun at 169 MHz. They had taken the lower envelope of the Nancay E-W one-dimensional scans, for each year, during the period 1957-70, and showed that the measured T_b of the Sun does not vary with the sunspot cycle and the

average value is approximately 0.75×10^6 K. It was concluded that the T_b corresponding to the lowest envelope of all the scans in a year may actually correspond to the T_b of a hole. In other words, the identification of the radio quiet Sun with the CHs gives an estimation of the brightness temperature of the holes (Avignon et al. 1975; Borkowski, 1982). Dulk et al. (1977) tried to derive the density and temperature distributions in the transition region and inner corona using the EUV and radio observations of a CH at four different frequencies (80 MHz, 160 MHz, 1.42 GHz and 10.7 GHz). They pointed out that the electron density derived from the EUV data is about three times that inferred from the radio data. The discrepancy between the EUV and radio densities increases if one goes to the decameter wavelengths. Wang, Schmahl and Kundu (1987) on the basis of the data obtained with the CLRH pointed out that the discrepancy between the density values obtained by the EUV data and radio maps is much larger compared to that of Dulk et al. (1977). A similar discrepancy was reported by Jackson, Sheridan and Dulk (1979), when they compared the brightness of the streamer seen in their 80 MHz map with that in the white light picture. Therefore it is possible that the density models of the solar corona which are presently used may not be accurate.

6.2.4 Other possibilities

Apart from the refraction effects, several other scenarios have also been put forward by various workers, to explain the behaviour of the radio Sun at meter-decameter wavelengths. According to Subramanian and Sastry (1988), the observed low T_b at decameter wavelengths can be explained if one assumes that the entire corona is not at an uniform temperature and there is a gradient in the temperature. They calculated the radio spectrum of the continuum

emission from the undisturbed Sun at decameter wavelengths from their observations and found that the spectral index varied from +1.6 to +3.6, during the period of sunspot minimum. According to them, it was not possible to increase the spectral index to values $\geq +3$, either by varying the density gradient or by uniformly increasing the temperature and density over the corona. Golap and Sastry (1994) pointed out that the observations of the undisturbed Sun at the decameter wavelengths can be explained, if one takes into consideration the effects of the magnetic field on the propagation of radio waves in the corona. By including a radial magnetic field in their ray tracing calculations, they showed that the observed T_b at a height of $1.5 R_\odot$ from the center of the Sun can reach a maximum of 10^6 K, only if the field strength is approximately 2 G. Also according to them, at least part of the variations in the observed values of the T_b at low frequencies, can be explained on the basis of the variations in the strength of the magnetic field.

6.3 Observations with the GRH

In this section, the observations carried out with the GRH at 75 MHz during April 11-28, July 1-24 and August 1-9, 1997, are described. These particular periods were selected to study the emission from the undisturbed Sun, as it was close to sunspot minimum. Also no strong radio bursts were seen in our data during the above period. The radio maps were reasonably symmetric (Figure 6.2 - 6.5) and the position of radio and optical centroids were within $10'$ of each other on most days, even in the presence of streamers. These differences are small compared to the half-power beamwidths of GRH at 75 MHz, which is about $13' \times 19'$ (RA \times DEC). The errors in the position of the centroid are mainly due to the refraction effects in the ionosphere. Therefore it

is possible that the contribution from active regions to the observed brightness temperature, if any, is not significant. The GRH is a transit instrument and the beam can be pointed anywhere along the meridian in the zenith angle range $\pm 45^\circ$ using remotely controlled phase shifters (see Chapter 2). On each day, the observations were started approximately 15 minutes before the expected transit time of the source and the observing run lasted for about 30 minutes. But due to primary beam attenuation (along hour angle), only 8 minutes of data (± 4 minutes on either side of the transit) was used for map making (see Chapter 4 for details of map making). The time resolution used was 4.64 seconds. The flux densities were calculated by summing the values of the various contours upto the half-power level (Sastry, 1994). They were then calibrated using the radio sources 3C144 and 3C274. In the present work we have used the integrated flux densities since the measurement of peak flux values can be misleading for extended sources like Sun, contrary to what occurs with the calibration sources (Lantos and Avignon, 1975). The brightness temperature ($^\circ\text{K}$) was calculated using the formula,

$$T_b = \frac{4283 S \lambda^2}{\theta_{EW} \theta_{NS}}$$

where λ (m) is the wavelength of observation, S (Jy) is the observed integrated flux density and θ_{EW} , θ_{NS} (arc min) are the E-W and the N-S half-power diameters respectively. The errors in the observed brightness temperatures are mainly due to the uncertainty in the flux densities of the calibrators which is approximately 5% (Nelson, Sheridan and Suzuki, 1985). The average values of the integrated flux density and the brightness temperature are 15675 Jy and 0.85×10^6 K for April, 1997 ; 11920 Jy and 0.55×10^6 K for July-August, 1997. The corresponding values for the E-W and the N-S diameters (full width at half maximum), after correcting for the effects of the beam, are $37'$ and $34'$ for April, 1997 ; $46'$ and $32'$ for July-August, 1997. These values are within

the range of previous measurements made by various workers and compiled by Sheridan and McLean (1985). The eccentricity, i.e., the ratio of the N-S to the E-W diameters was also calculated and their average values are 0.92 and 0.69, respectively for the above two periods. Table 6.1 and 6.2 shows the minimum and maximum values of the various measured parameters.

APRIL, 1997 (Frequency : 75 MHz)		
Parameter	Minimum	Maximum
Integrated flux density	12243 Jy	19283 Jy
Brightness temperature	0.68×10^6 K	1.09×10^6 K
E-W diameter	32'	42'
N-S diameter	33'	36'

Table - 6.1

JULY-AUGUST, 1997 (Frequency : 75 MHz)		
Parameter	Minimum	Maximum
Integrated flux density	7576 Jy	18494 Jy
Brightness temperature	0.25×10^6 K	0.93×10^6 K
E-W diameter	39'	51'
N-S diameter	31'	34'

Table - 6.2

One can see that there was not much of variation in the values of the N-S diameter during the months of April and July-August, 1997. The variations in the other observed values cannot be due to the gain variation in the primary beam (along declination) of the array, since in the present case, both the

calibrator and Sun were close to the instrumental zenith (14.1° N) during the above observational period. It should however be noted that similar variations have been reported earlier in the literature (Sastry, 1994; Thejappa and Kundu, 1992).

6.4 Discussions and Conclusions

As scattering by small-scale density inhomogeneities is one of the major reasons attributed for the low values of the observed T_b and the variations in it, one should expect an inverse correlation between the observed flux densities and the half-power widths. Figures 6.6 and 6.7 show the variation of the integrated flux density with the E-W diameter for the observational periods mentioned in the last section. One can see that for the period April 11-28, 1997, the variations in the integrated flux density and the half-power diameters are positively correlated. On the other hand, for the period July 1-24 and August 1-9, 1997, there seems to be a weak negative correlation between them. The measured correlation coefficients in both the above cases are very small. This implies that the low values of the observed T_b cannot be explained purely on the basis of scattering. Another possible observational evidence against scattering is the appearance of discrete sources in our maps. According to Riddle (1974), in the presence of scattering, discrete sources crossing the solar disk should appear as brightness enhancements close to the limb and as brightness depression near the center. For a CH, the situation is reversed. But in the present case, discrete sources in the corona always appear as brightness enhancements, irrespective of whether they are close to the limb or at the disk center (Figure 6.8 and 6.9). Again, even near the disk center, a CH appears as a region of reduced brightness (Figure 6.10).

GAURIBIDANUR RADIO HELIOGRAM - 75 MHz

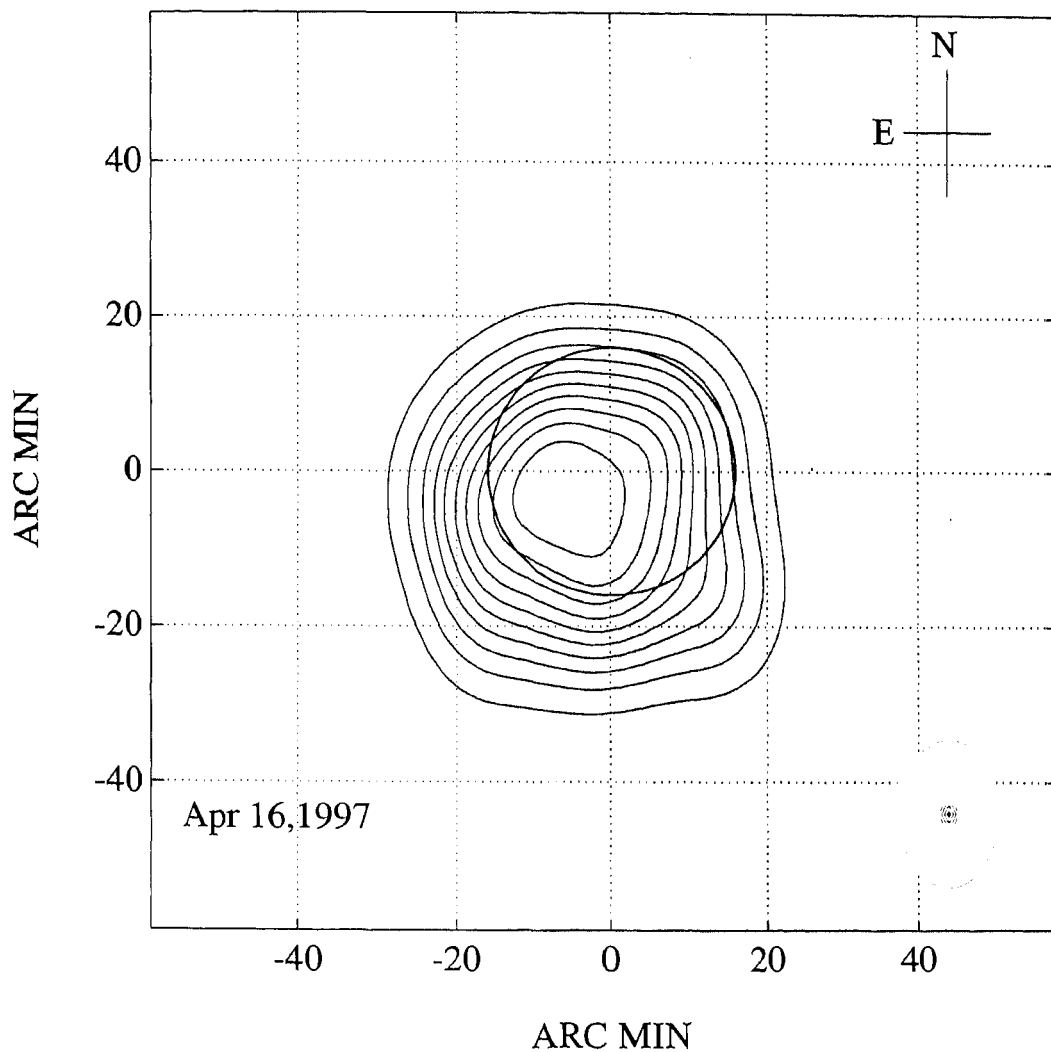


Figure 6.2: The open circle at the center is the optical Sun and the filled circle at the bottom right is the beam of the instrument. $T_b = 0.77 \times 10^6$ K, contour interval = 0.07×10^6 K.

GAURIBIDANUR RADIO HELIOGRAM - 75 MHz

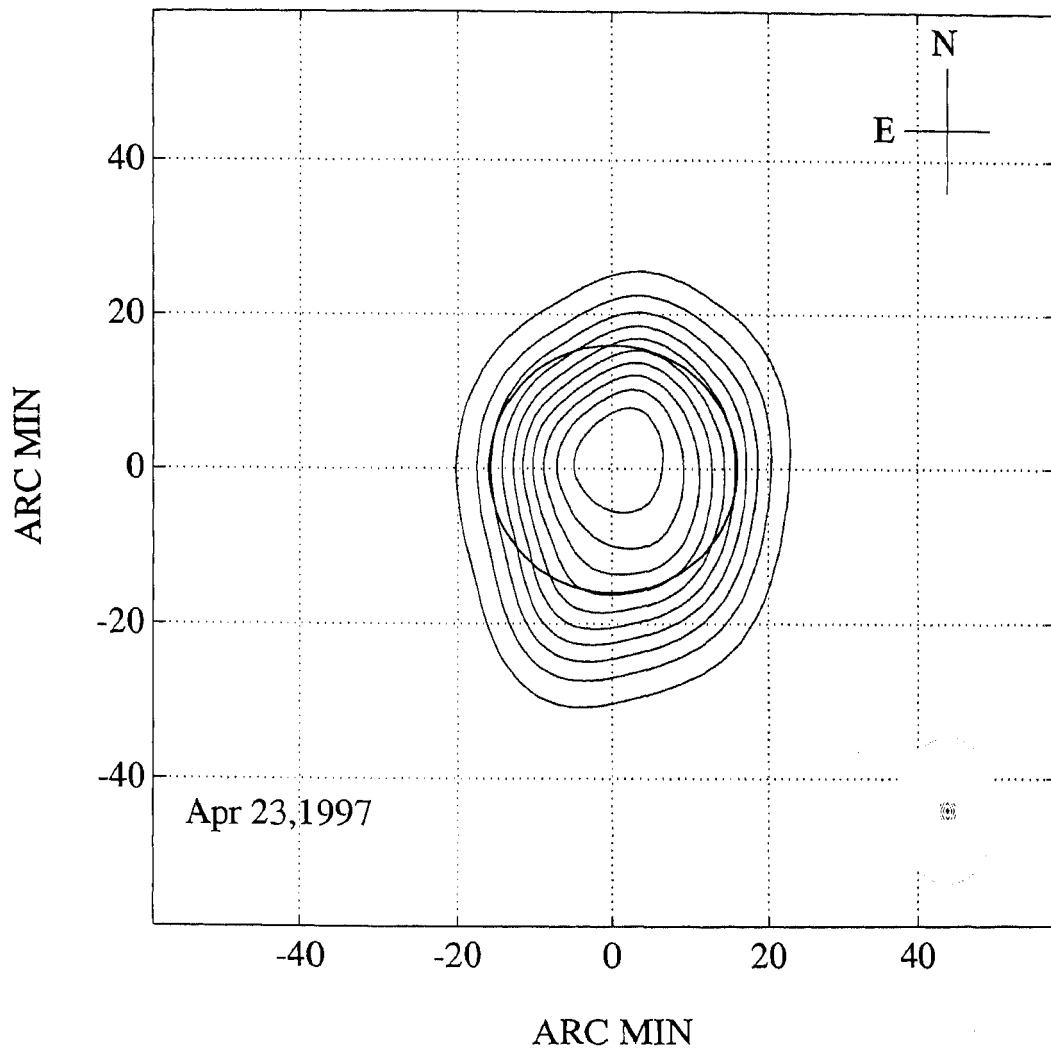


Figure 6.3: $T_b = 0.97 \times 10^6$ K, contour interval = 0.09×10^6 K.

GAURIBIDANUR RADIO HELIOGRAM - 75 MHz

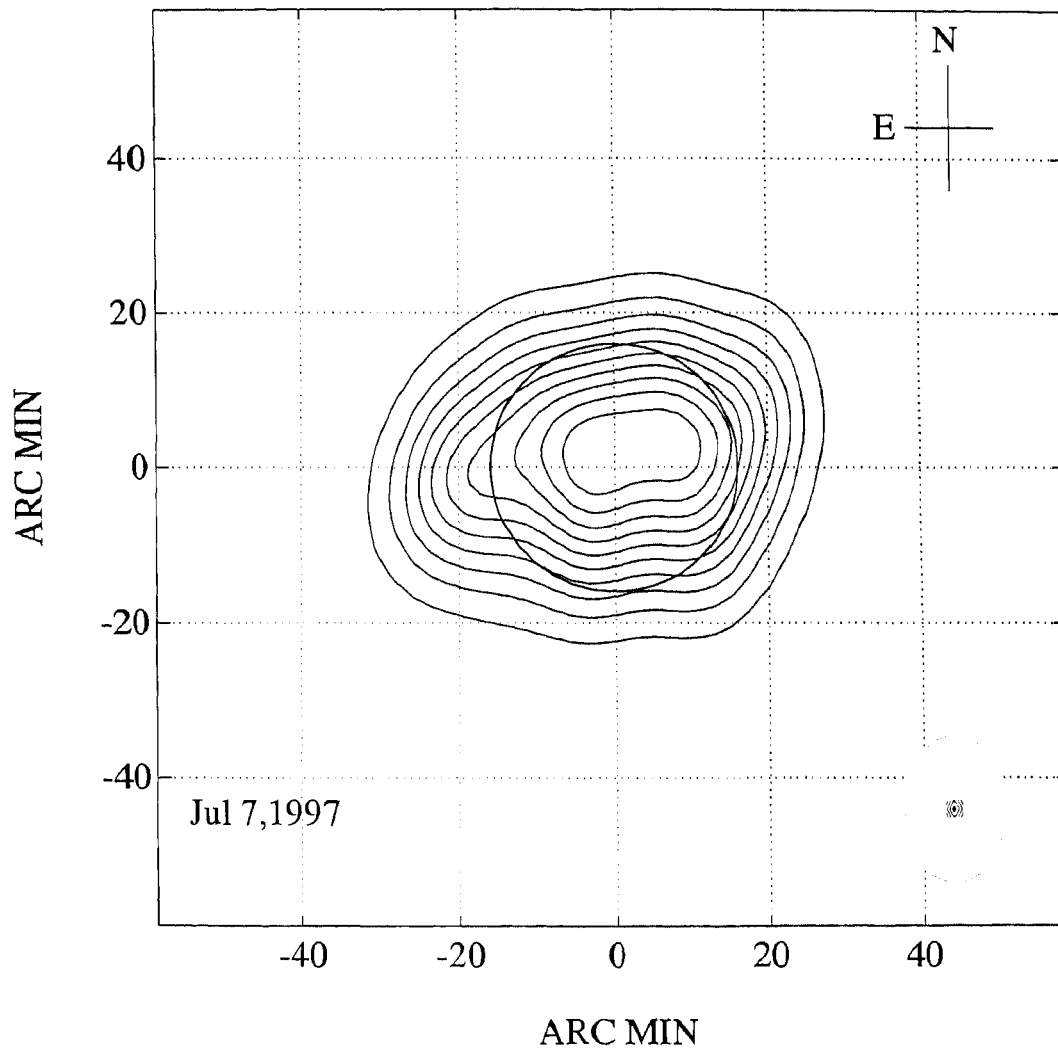


Figure 6.4: $T_b = 0.65 \times 10^6$ K and the contour interval = 0.06×10^6 K.

GAURIBIDANUR RADIO HELIOGRAM - 75 MHz

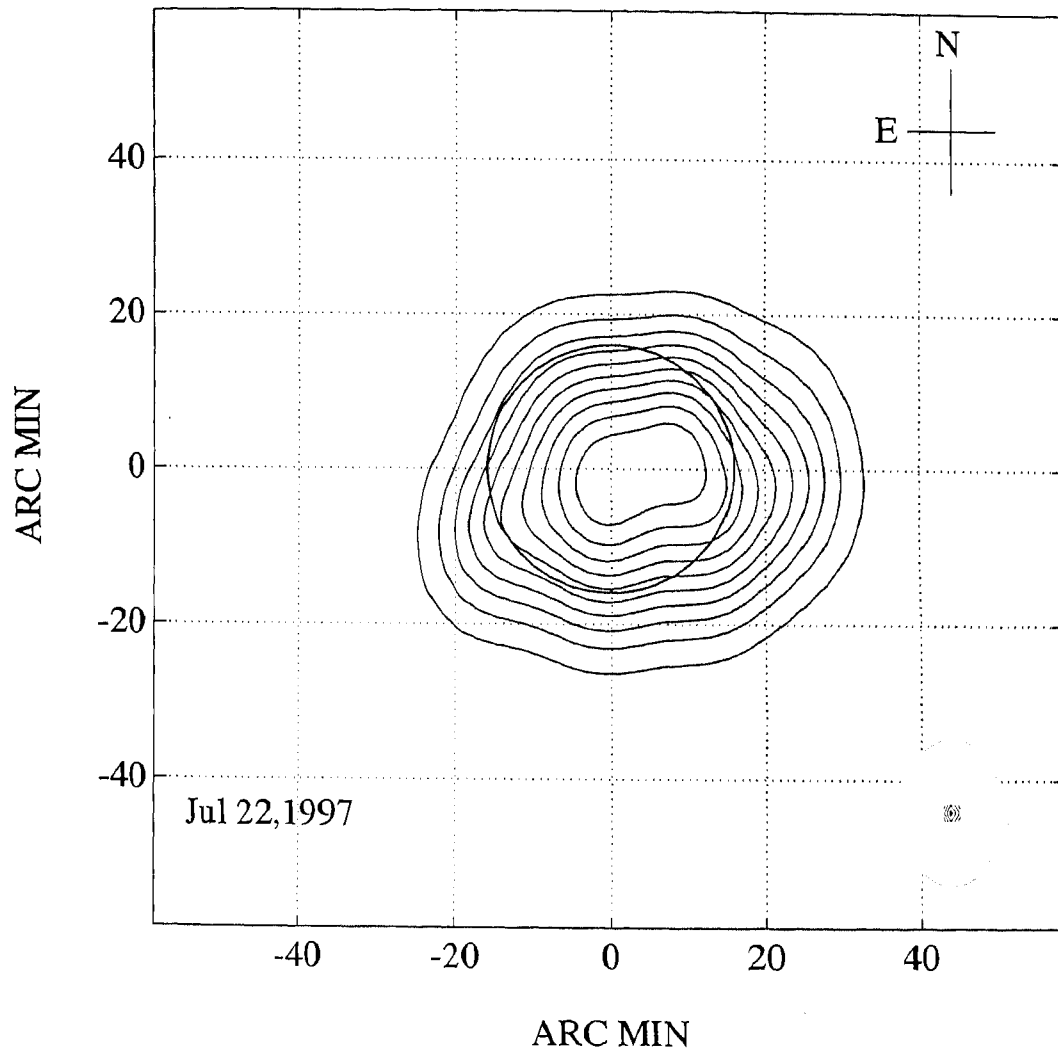


Figure 6.5: $T_b = 0.38 \times 10^6$ K and the contour interval = 0.035×10^6 K

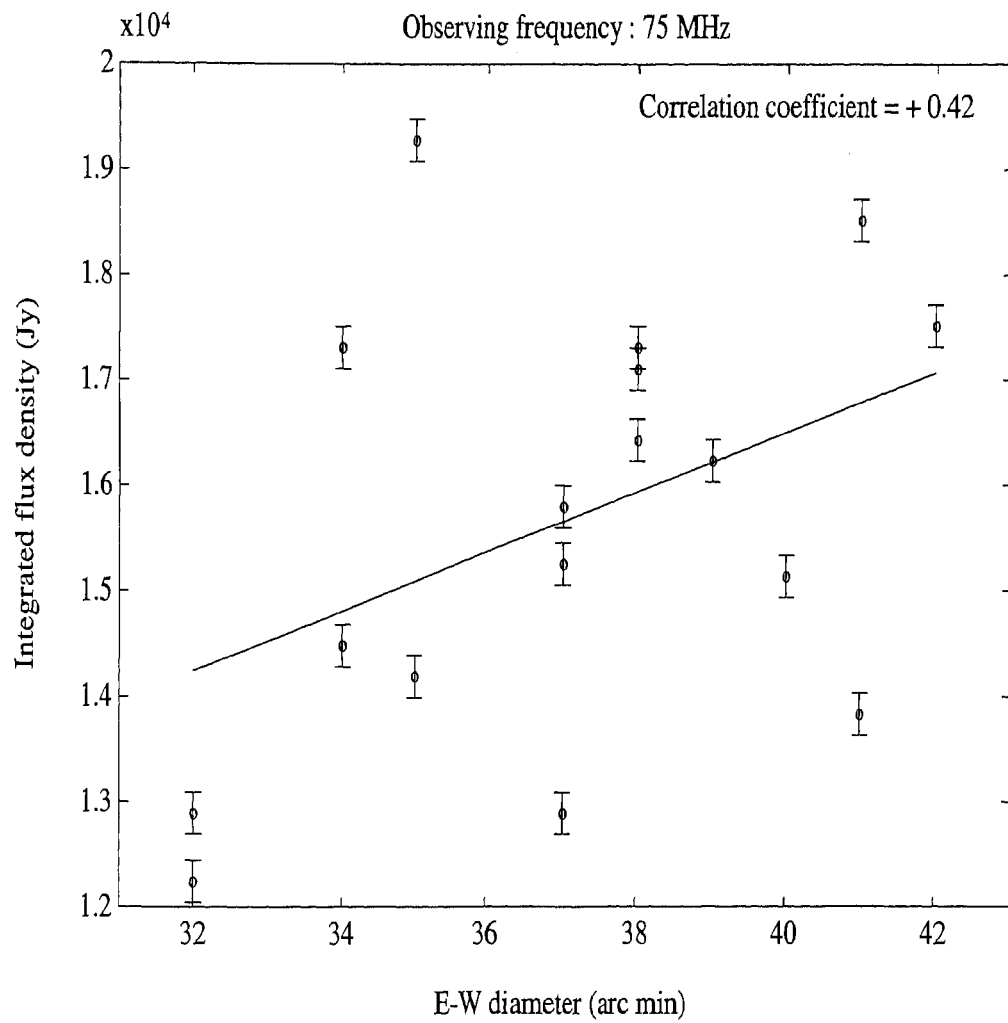


Figure 6.6: Variation of integrated flux density with E-W diameter during the period April 11-28, 1997

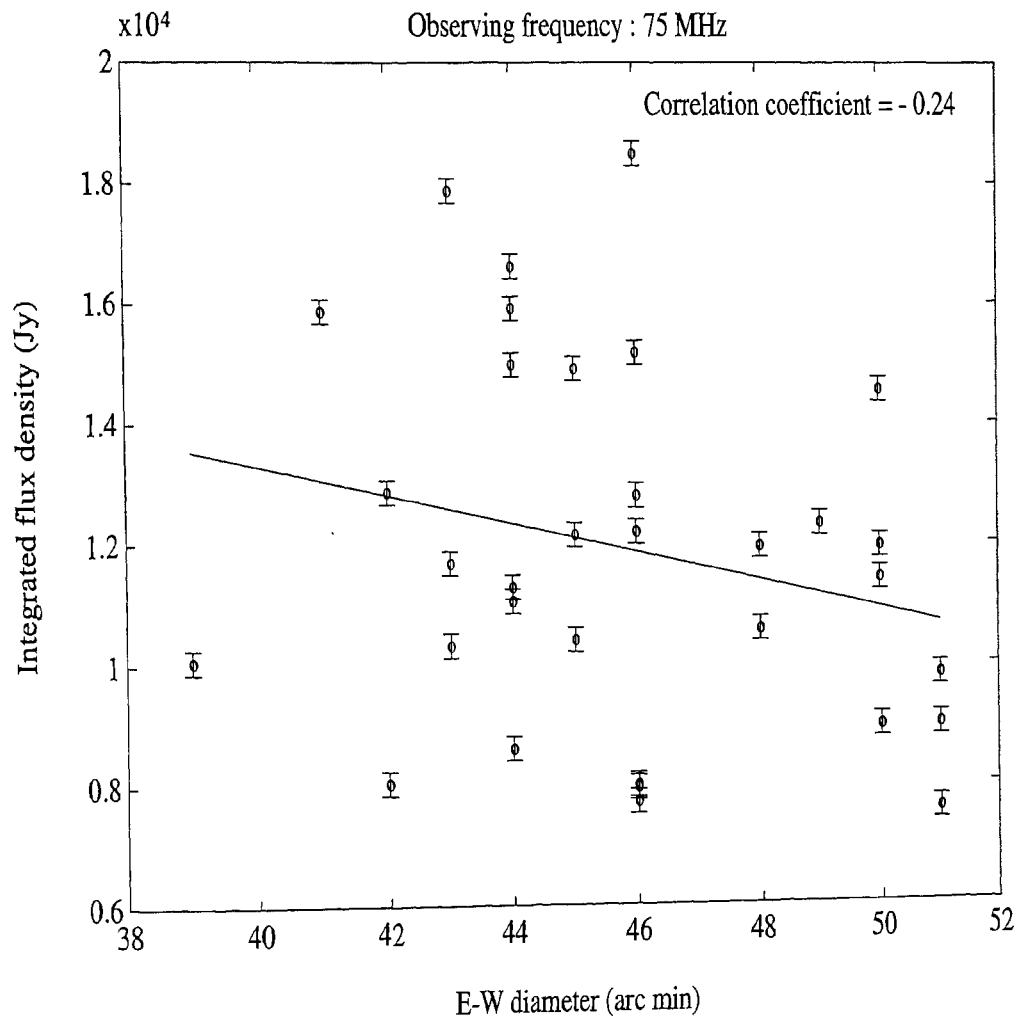


Figure 6.7: Variation of integrated flux density with E-W diameter during the period July 1-24 and August 1-9, 1997

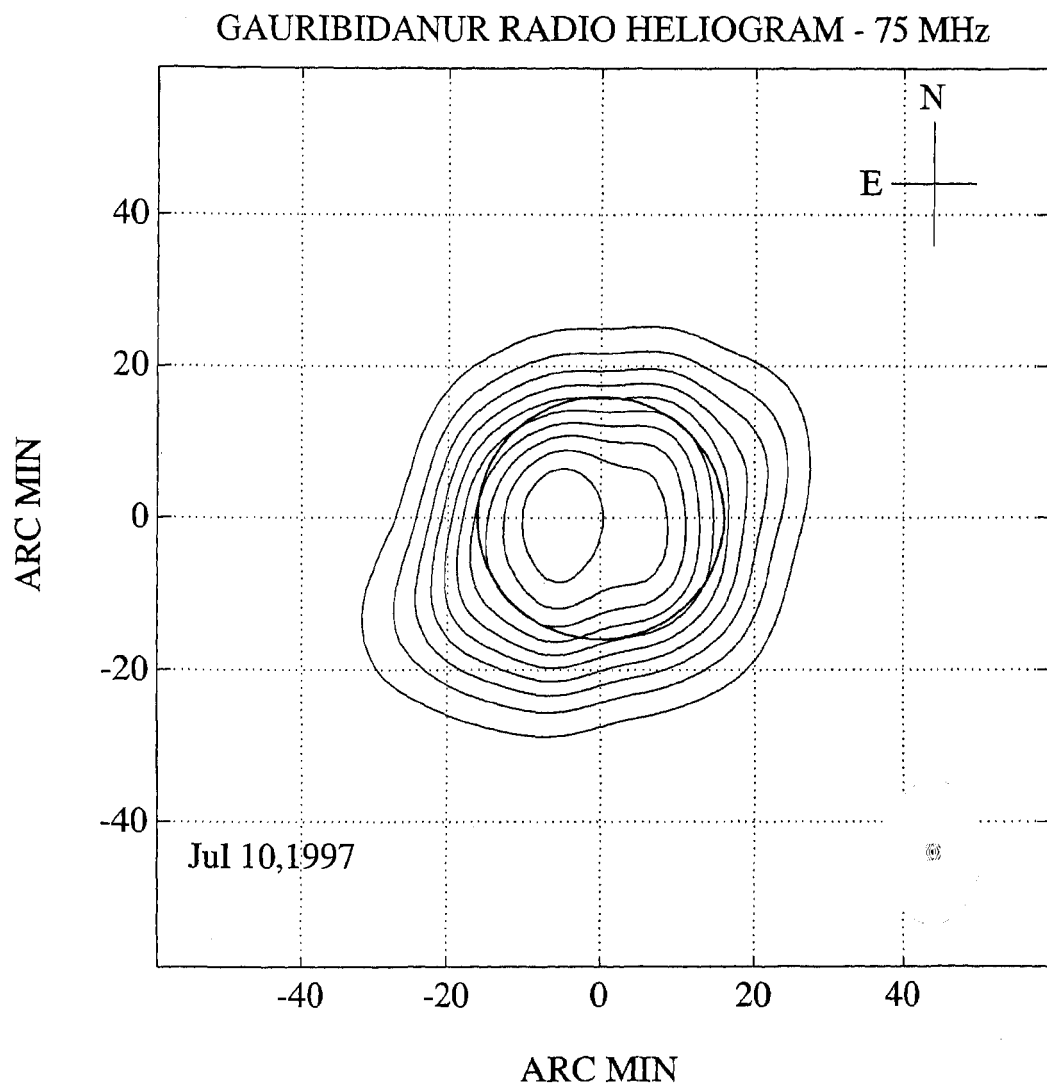


Figure 6.8: Radio map obtained with the GRH at 06:30 UT. $T_b = 0.55 \times 10^6$ K, contour interval = 0.06×10^6 K.

GAURIBIDANUR RADIO HELIOGRAM - 75 MHz

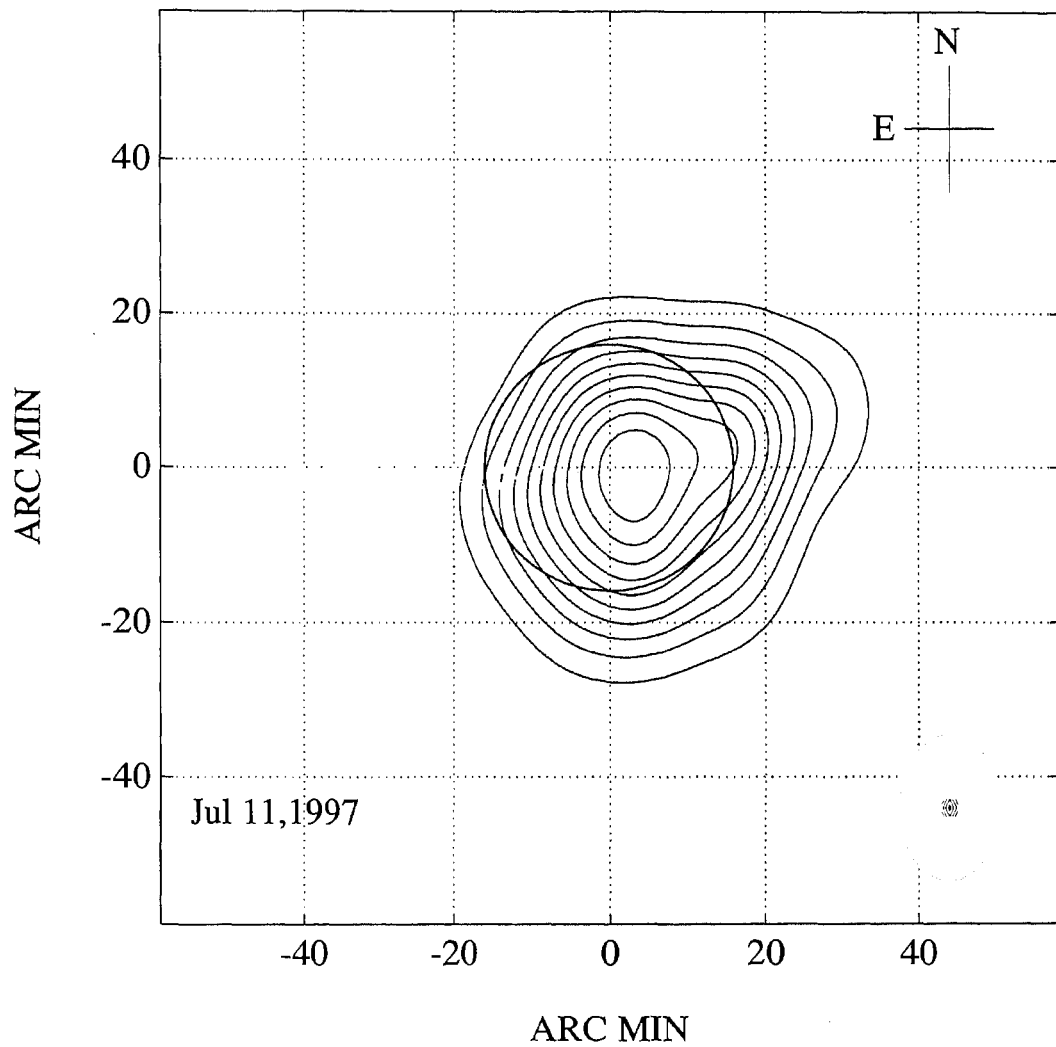


Figure 6.9: Radio map obtained with the GRH, the following day at 06:30 UT. $T_b = 0.34 \times 10^6$ K, contour interval = 0.03×10^6 K.

GAURIBIDANUR RADIO HELIOGRAM - 75 MHz

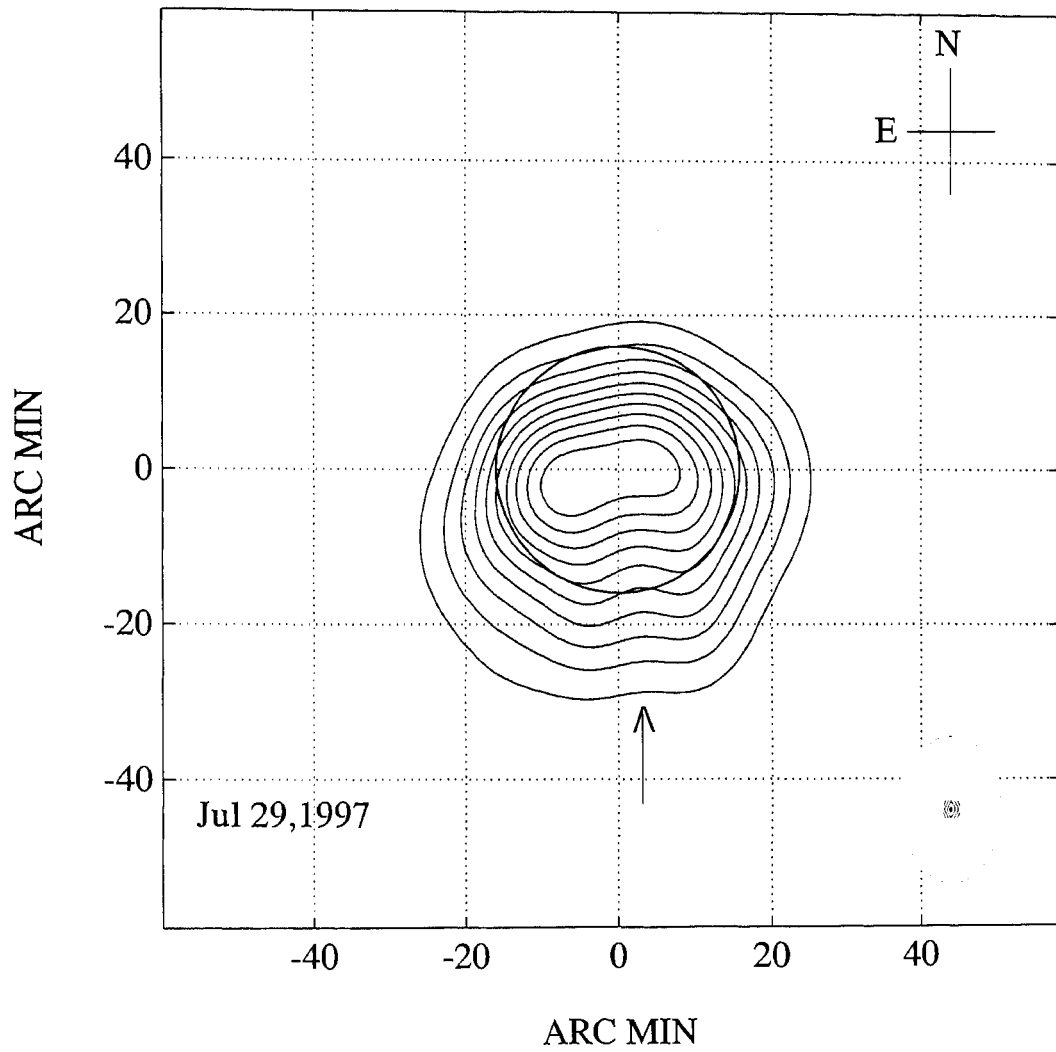


Figure 6.10: Radio map obtained with the GRH at 06:30 UT, showing the presence of a CH (indicated by the arrow mark) at the southern limb. $T_b = 0.54 \times 10^6$ K, contour interval = 0.05×10^6 K.

One important thing to be noticed in the maps shown in Figures 6.4 and 6.5 is the bulgings in the contours along the equatorial plane, compared to Figures 6.2 and 6.3. These are probably the radio manifestations of coronal streamers (Kundu et al., 1987). In order to compare the large-scale structure seen in the radio map (Figure 6.8) with those seen in the optical pictures, the intensity profiles obtained with Mauna Loa K-coronameter and the Sacramento Peak three-line (Fe XIV 5303 Å, Fe X 6374 Å) coronal photometer at $1.15 R_{\odot}$ are shown in Figures 6.11 and 6.12. The discrepancy between the latitudes of the enhancements seen in the optical and radio pictures may be partly due to refraction effects (Lantos and Alissandrakis, 1996) and partly due to the difference in the coronal heights at which these pictures are made. It is to be noted that the radio emission at 75 MHz originates at a height of $0.4 R_{\odot}$ above the photosphere (Thejappa and Kundu, 1994).

It is well known that the solar corona during the sunspot minimum is dominated by streamers at low latitudes. Therefore, it is quite possible that the low values of T_b observed by us during the months of July and August are due to the increased E-W diameter (see the tabular column in the earlier section) caused by the presence of these weak streamer sources. It is well known that in the presence of streamers, the density gradient becomes more steep thereby refracting the rays much above the critical level. The presence of extended structures along the E-W direction during this period is also reflected in the eccentricity values quoted in the last section.

One possible reason for the absence of a similar increase in the E-W diameter during the month of April, 1997 though streamers were seen in the MLSO pictures, might be the presence of weak noise storm sources, observed with the Nancay radioheliograph at 164 MHz during that period (Solar Geophysical data, June 1997). It is well known that these sources produce faint

non-thermal continuum without the usually associated Type I bursts. According to Alissandrakis, Lantos and Nicolaidis (1985), the measured T_b of these sources at 169 MHz is $\sim 1.2 \times 10^6$ K. It is also known that storm sources tend to occur on the solar disk (Kai, Melrose and Suzuki, 1985) and their sizes at frequencies around 75 MHz can be $\sim 1 R_\odot$ (Kundu and Gopalswamy, 1990). It is therefore possible that the lower values of the observed half-power widths and higher T_b during April 1997 compared to July-August, 1997 is an indication of the presence of the noise storm sources.

It is well known that during sunspot minimum the surface of the Sun is dominated by extended CHs and they are more prominently seen near the poles (Broussard et al. 1978). For an investigation of the variations in the quiet Sun diameter, Leblanc and le Squeren (1969) used fan-beam observations made over the years 1957-1965 at 169 MHz with the Nancay E-W interferometer and concluded that though the equatorial diameter varied between $38'$ and $47'$, the polar diameter remained constant at $32'$. The lower values of the N-S diameter compared to the E-W diameter and their constancy in the GRH data presented in this chapter are similar to the observations of Leblanc and le Squeren (1969). It is also well known that lifetimes of the CHs can span several solar rotations (Ferguson, 1981). Therefore it remains to be seen whether the low values of the observed T_b at frequencies < 100 MHz can also be attributed to the presence of CHs.

The present observations imply that the low values and the variations of the observed quiet Sun T_b at meter-decameter wavelengths seems to be due to a combination of different effects. One has to carry out high resolution observations so that the effects of the noise storm sources, CHs and streamers can be separated out and the quiet Sun emission can be studied in isolation.

Figure 6.11: White light picture of the corona obtained with the Mauna Loa MKIII K-Coronameter. The occulting disk is at a height of $1.122 R_{\odot}$ from the center of the Sun.

WLSO-MK3 Coronameter

Jul 10, 1997

DOY 191

7:45UT



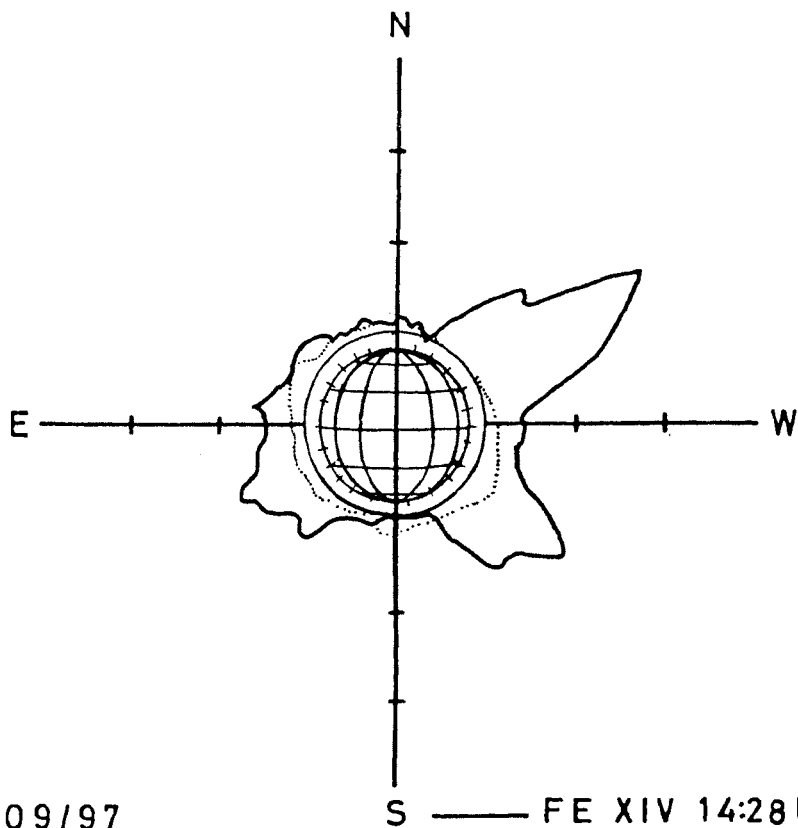
11 images

18:51UT to 19:31UT

Scaling: -400 to 3400

North is straight up

Figure 6.12: Intensity profiles of the solar corona at a height of $1.15 R_{\odot}$ from the center of the Sun. These profiles were obtained with the Sacramento Peak three-line (Fe XIV 5303 Å, Fe X 6374 Å) coronal photometer.



07/09/97
(DOY 190)

S ——— FE XIV 14:28 UT 1.15 R_⊙
..... FE X 14:55 UT 1.15 R_⊙

Chapter 7

Radio signatures of Coronal Mass Ejections

7.1 Introduction

Coronal mass ejections (CMEs) are an important aspect of evolution of the corona, involving the disruption of large scale structures of plasma and magnetic fields, and their expulsion into the heliosphere. CMEs are now considered the key causal link between the solar activity and major transient interplanetary and geomagnetic disturbances (Kahler, 1992). Though flares, eruptive prominences and non-equilibrium magnetic configurations are among the postulated origins of CMEs, the relationship of CMEs to flares and prominence eruptions still remains a source of debate. While 10-17% of the CMEs are associated with flares and 30-34% with eruptive prominences, the largest fraction of 30-48% is unrelated to near-surface events on the Sun (Wagner, 1984). Evidently CMEs must be generated either by different mechanisms, or by some fundamental process which, under suitable conditions, can also trigger flares or erupting prominences (Hewish and Bravo, 1986). The

relationship between CMEs, flares, prominence eruptions, coronal and interplanetary shocks, and various kinds of radio bursts is an extremely active area of research. In view of the recent ‘Solar Flare Myth’ (Gosling, 1993) which suggests that the launching of the geoeffective CMEs is independent of flare occurrence, the interest in the causes and consequences of the CMEs has been renewed further. The physical characteristics of CMEs have been derived primarily from ground and space-based white light coronagraph observations (Hundhausen, 1993). They can also be estimated from low frequency (< 100 MHz) radio observations (Gopalswamy and Kundu, 1992). In this chapter, we describe some of the coronal structures like noise storms, coronal holes and type III bursts that were observed with the Gauribidanur radioheliograph (GRH) in association with the CMEs. Calculation on the mass released from the corona in the aftermath of a possible halo¹ CME event observed with the GRH is also presented.

7.2 CME event of April 13, 1997 and its association with radio noise storm

Ever since its discovery in 1946 (Hey, 1946), the solar noise storm (or Type I emission) has been one of the longest studied phenomena by solar radio astronomers. It consists of several short-lived, narrow band bursts which are superimposed on a background of continuum emission. Elgaroy (1977) has given a detailed review of the observational properties of noise storms. According to Kai et al. (1985), the storm sources are believed to be located in large-scale magnetic structures above active regions, sometimes in regions

¹CMEs that occur near the center of the solar disk (as viewed from Earth) look like ‘halos’ in whitelight coronagraph images and hence the name.

interconnecting active regions. Mercier et al. (1984) on the basis of their observations of a noise storm during 8 consecutive days, have reported that the emission originated from the leg of a magnetic arch. According to the current models, the emission is due to plasma mechanisms and takes place close to the plasma frequency (Elgaroy, 1977; Thejappa, 1991). The emission originates in the lower solar corona at altitudes between 0.1 and $0.5 R_{\odot}$ above the photosphere (Lang and Willson, 1987). At lower frequencies, below $40 - 60$ MHz, the character of noise storms changes. The continuum becomes weaker with $T_b < 10^7$ K and type I bursts tend to disappear (Kai et al., 1985; Kundu and Gopalswamy, 1990).

Elgaroy (1977) has given an overall review of the optically observed phenomena in association with the noise storms. Several cases of positive associations of $H\alpha$ flares with type I storms have been reported (Takakura, 1967). But, storms last for several days and also some storms occur without associated $H\alpha$ flares. So the results are not conclusive. On the basis of type I noise storms observed during the Skylab period, Brueckner (1982) has concluded that the occurrence of major type I storms are associated with strong changes in the loop structure of the corona. On the disk, these coronal changes are correlated to the emergence of new magnetic flux in the vicinity of existing large active regions. According to Kundu (1996b), noise storms are born in evolving systems of large-scale magnetic loops, when the coronal magnetic field restructures itself in response to a perturbation of the underlying active region. Since the onset of CMEs is also associated with newly emerging flux from sub-photospheric levels (Feynmann and Martin, 1995), there could be a possible relationship between all the three, i.e. the emergence of new magnetic flux, noise storms and CMEs. Some evidence exists for a correspondence between noise storms and CMEs from observations carried out with

the Nancay radioheliograph (NRH) at 169 MHz (Lantos et al. 1981; Kerdraon et al. 1983 and Pick, 1996) and the VLA at 327 MHz (Habbal et al. 1996). However there is no such observational evidence at low frequencies, particularly linking a noise storm source with the onset of a CME.

7.2.1 Observations

The CME event of April 13, 1997 was observed by the Large Angle and Spectrometric Coronagraph (LASCO) on the Solar and Heliospheric Observatory (SOHO) spacecraft at 16:36 UT on April 13, 1997. The event took place close to the limb in the south-west quadrant of the Sun (Figure 7.1) and the estimated initial velocity was about 50 km s^{-1} (Chen et al. 1997). Apart from a weak flare around 04:00 UT (Solar Geophysical data, May 1997), no significant X-ray events were indicated either by the GOES data or the YOHKOH images. No $\text{H}\alpha$ filament disappearance that can be associated with the CME was also observed. But the data obtained with Extreme Ultraviolet Imaging Telescope (EIT) on board SOHO indicate magnetic activity in the south-west quadrant of the Sun throughout April 13, 1997 (Chen et al. 1997). Figure 7.2 shows the radio map obtained with the GRH at 75 MHz around 06:30 UT on April 13, 1997 overlaid on the YOHKOH SXR image obtained at 06:14 UT, the same day. The measured peak brightness temperature of the radio map was approximately $0.91 \times 10^6 \text{ K}$. Figure 7.3 shows the radio map obtained with the NRH at 164 MHz on the same day around 09:03:30 UT. According to the Solar Geophysical Data (June, 1997), the bright region close to the south-west limb in the NRH map is due to a noise storm source. Because of the close spatial correspondence between the radio maps in Figure 7.2 and 7.3, and since Type I bursts were also observed on that day by the radio spectrograph at Potsdam (Solar Geophysical Data, June 1997), it is possible

Figure 7.1: CME event observed close to the limb in the S-W quadrant of the Sun with LASCO on board SOHO on April 13, 1997 around 16:36 UT. North is straight up and East is to the left (landscape view).

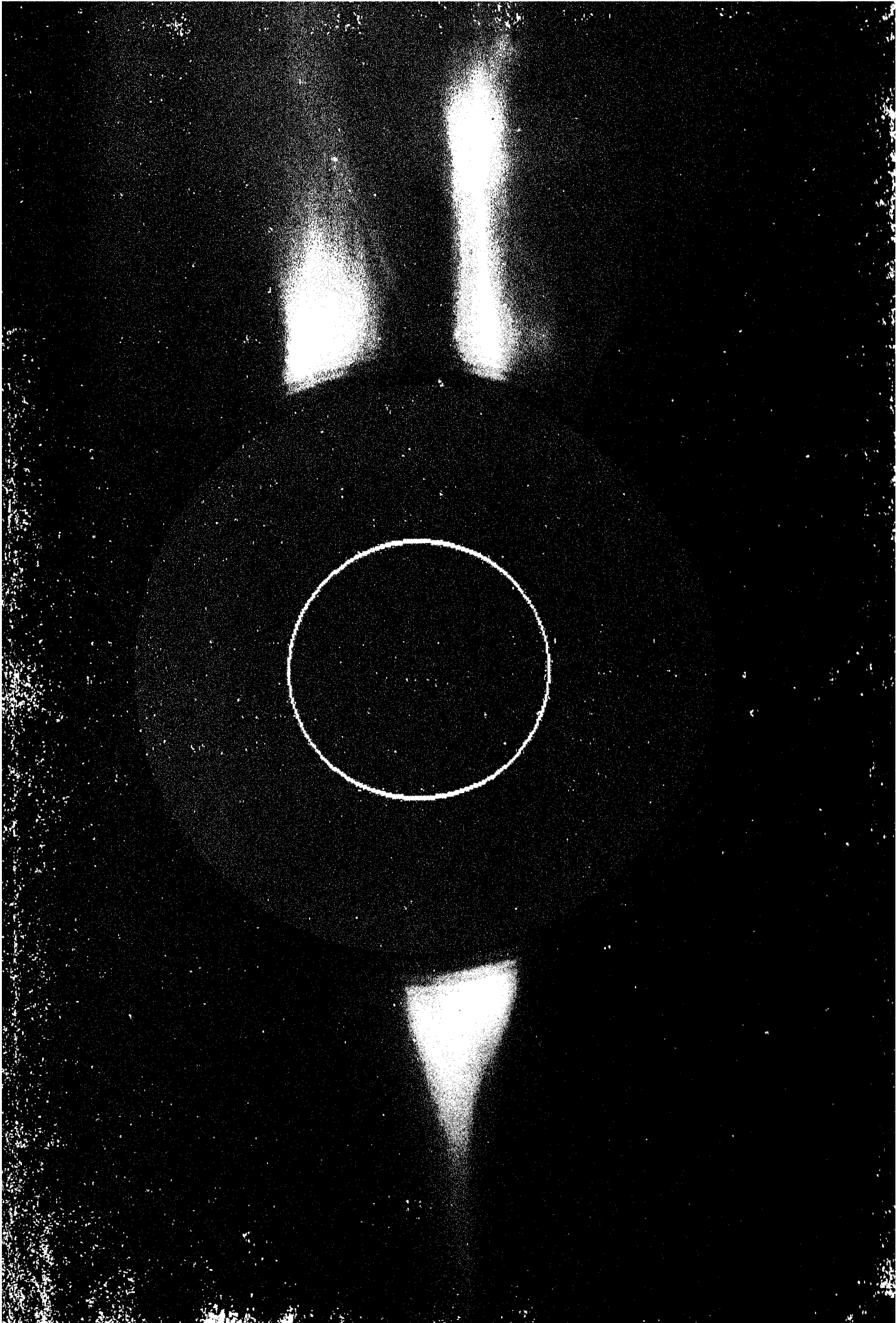
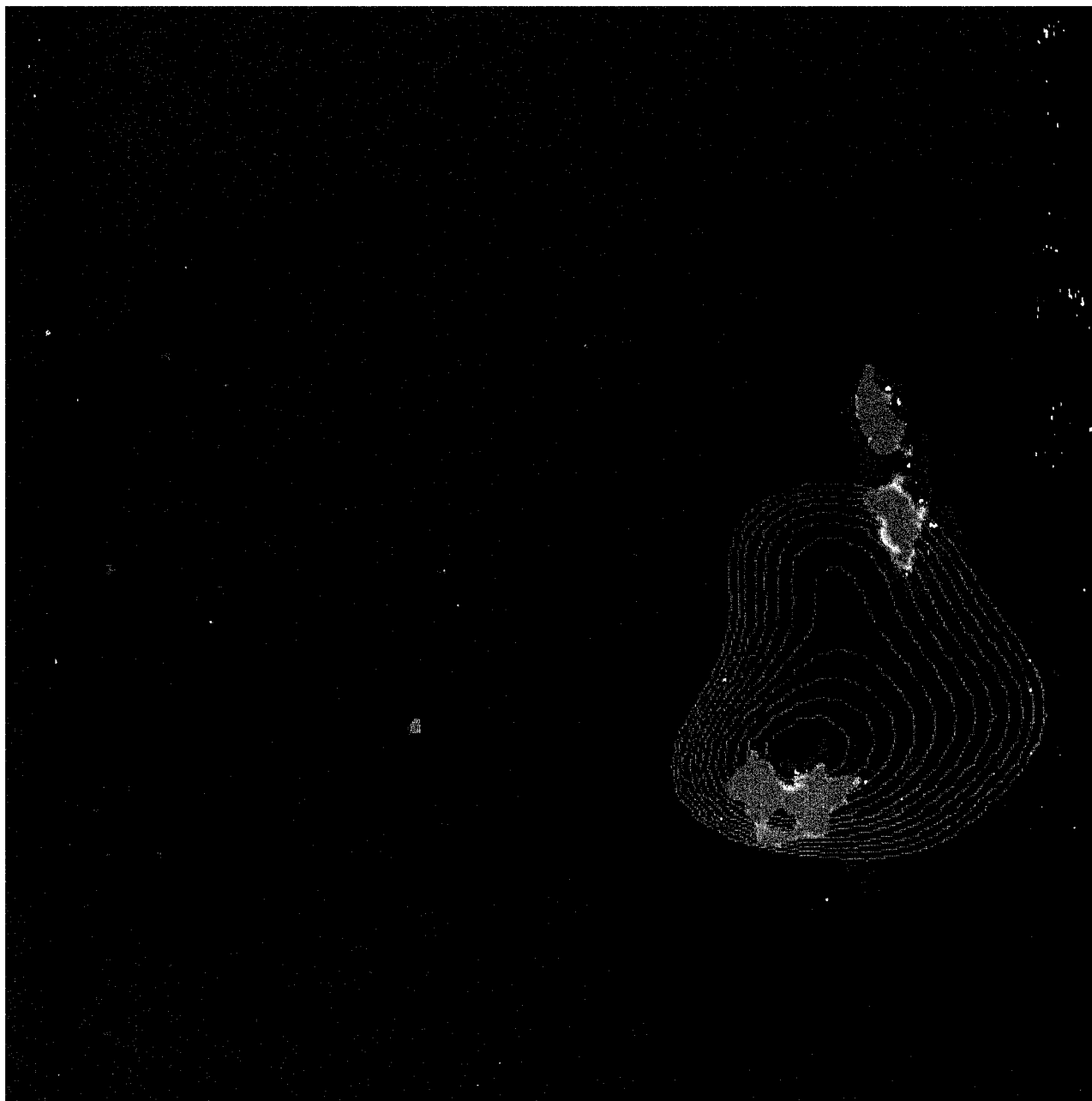


Figure 7.2: Noise storm continuum observed with the GRH on April 13, 1997 around 06:30 UT overlaid on the YOHKOH SXR image obtained at 06:14 UT. North is straight up and East is to the left.



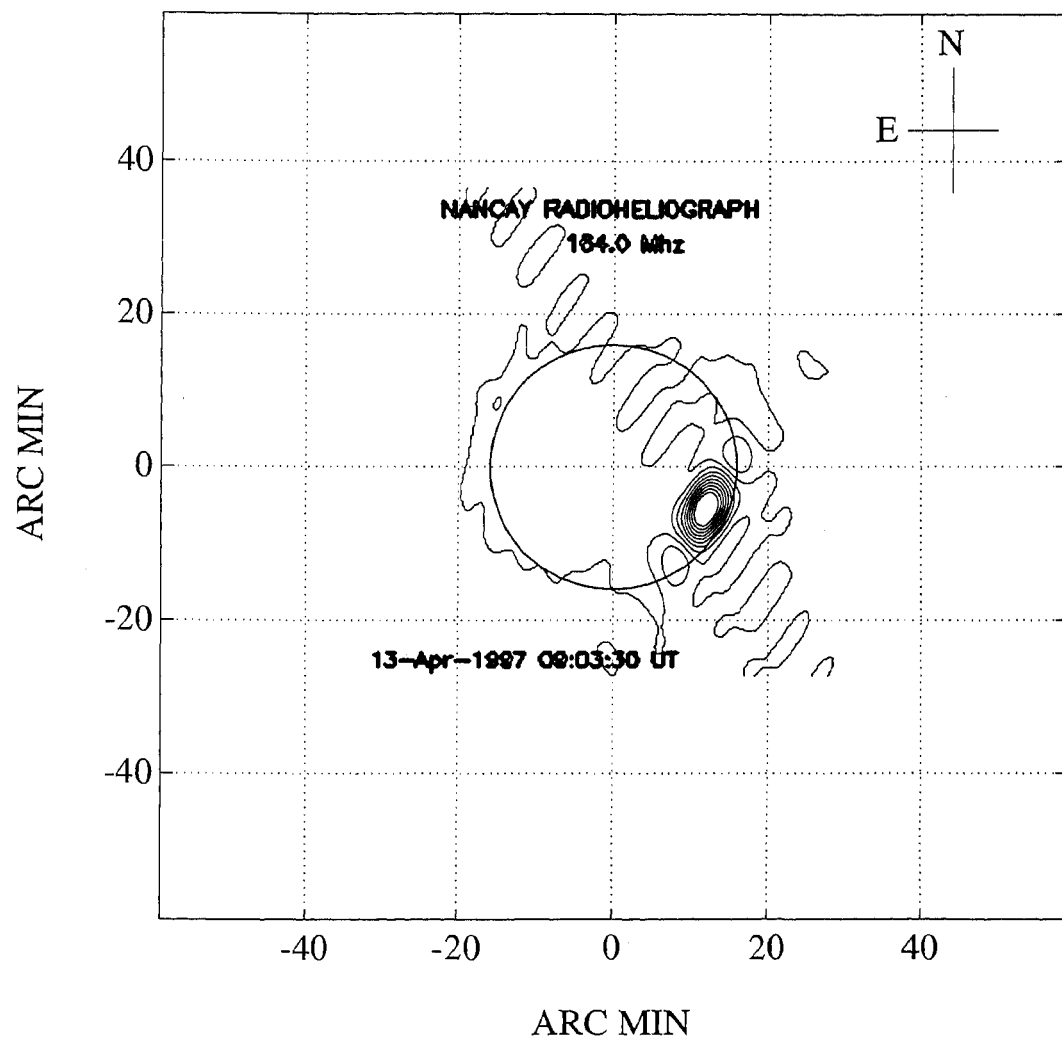


Figure 7.3: Noise storm continuum observed with the NRH around 09:03:30 UT.

that the bright region (towards the South) seen in the GRH map in Figure 7.2 corresponds to the same noise storm source seen in the NRH map in Figure 7.3. Both at 75 and 164 MHz, the source was seen at the same location the next day also. It would therefore appear that there is no appreciable shift in the position of the source centroid due to ionospheric refraction effects in the 75 MHz GRH image.

7.2.2 Discussions and Conclusions

The present set of radio observations are consistent with the earlier findings by Kerdraon et al. (1983), that metric noise storm onsets or enhancements are systematically associated with appearance of additional material in the corona. Also it confirms the recent finding by Habbal et al. (1996) that noise storm sources at the location of the CME, precede and outlive it. McLean (1973), pointed out that some type I storms may be due to a slowly ($\sim 100 \text{ km s}^{-1}$) rising column of gas interacting with the stationary corona around it. A similar result was obtained by Lang and Willson (1987) on the basis of VLA observations at 327 MHz. They pointed out that the noise storm source observed by them might have been triggered by a disturbance moving outward from the surface of the Sun at a speed of 78 km s^{-1} . On the basis of these results and the estimated initial velocity of the CME in the present case (50 km s^{-1}), it is possible that the noise storm source seen in both the GRH and NRH images may be closely related to the mass ejection event.

According to Feynmann and Martin (1995), eruptions of quiescent filaments and CMEs occur as a consequence of the destabilization of large-scale coronal arcades due to the interactions between these structures and new and growing active regions. Also it is well known that metric noise storms are associated with magnetic activity in the neighbourhood of active

regions. Therefore it is quite possible all the three observations in the present case, i.e., the magnetic activity in the active regions, radio emission from the noise storm and the CME might have taken place in a sequential manner. Chen et al. (1997) has described the geometry of this particular CME event as that of a magnetic flux rope with the foot points remaining connected to the Sun. Based on this and the earlier results obtained by Dulk et al. (1976) and Lantos et al. (1981), it appears possible that the storm source observed by us and at Nancay might have been located in one of the footpoints of the CME. According to Gopalswamy et al. (1997), radio bursts of spectral class type II, III and IV are generally associated with CME's due to eruptive prominences. Since the event of April 13, 1997 was not associated with any of the above except for noise storm emission, the onset of storm continuum at meter-decameter wavelengths can be offered as a harbinger of CME's. Such a possibility has already been noted in the literature by Wagner (1984).

7.3 CME event of September 23, 1997 and its association with Coronal holes, Type radio III bursts

Coronal holes (CHs) are defined as regions of low electron density and temperature (compared to the ambient) in the corona where the magnetic field (and flux) lines are open and extend into the interplanetary space. It is well established that geomagnetic activity is related to the appearance of CHs on the Sun (Hewish and Bravo, 1986). It has also been reported that there is an increase in the hole area, a day prior to the occurrence of the CME (Watanabe et al., 1992; Gonzalez et al., 1996). Srivastava et al. (1997), in a study of the

CMEs observed by the Solar Maximum Mission (SMM) satellite during the period March-September, 1980, found that the solar sources for most of the observed CMEs lay near the CH location, with an average distance ranging between $0^\circ - 20^\circ$.

Another important energetic event in the solar corona which is closely associated with the open field magnetic lines, are the low frequency Type III radio bursts. It is generally believed that a stream of sub-relativistic electrons accelerated low in the corona is responsible for type III radio bursts. According to Leblanc, Kuiper and Hansen (1974), most type III bursts observed at decameter wavelengths seemed to avoid the core of dense structures in the corona. In a comparison of type III radio bursts observed at 169 MHz with the pictures of the K-corona, Leblanc and De la noë (1976) have concluded that 75% of the active regions over which type III bursts occur are associated with low density coronal structures. These regions were found to correlate spatially with low intensity regions seen in the maps obtained by OSO-5 satellite. Recently, with the NRH, Kundu et al. (1994) observed type III bursts in conjunction with a X-ray bright point flare observed by the YOHKOH SXR telescope near a coronal hole. Therefore it is very important to know the type of coronal structures associated with individual type III burst sources. In the following section, we present evidence for possible association between the CHs, CMEs and type III radio bursts.

7.3.1 Observations

A large CME was observed in the south-eastern quadrant of the Sun by the LASCO on board SOHO on September 23, 1997 at around 23:48 UT (NASA/NOAA press report). This event which was associated with the active region NOAA 8088, was also related to a long duration C-class X-ray flare

of importance 1.5 reported in the Solar Geophysical Data (November, 1997). According to Bougeret, type III bursts were noticed by instruments aboard the WIND spacecraft as early as 01:30 UT on September 24, 1997. Also, a strong type III storm re-appeared on September 25 (NASA/NOAA press release). These type III bursts were also observed by the radio spectrograph at Potsdam (Solar Geophysical Data, November 1997). From the Sacramento Peak Fe XIV data published in the Solar Geophysical Data (December, 1997), an increase in the size of the CH located near the southern limb was noticed on September 23, the day prior to the CME event. Observations carried out with the GRH on September 23 at 109 MHz around 06:30 UT indicate the presence of a CH, which appears as region of reduced brightness near the southern limb and extends inwards towards the center (Figure 7.4). The observed brightness temperature was 0.54×10^6 K. On September 24 and September 25, only type III bursts were noticed. Their peak brightness temperatures were 1.82×10^7 K and 0.79×10^7 K respectively (Figures 7.5 and 7.6).

7.3.2 Discussion and Conclusions

It has been speculated that X-ray flares are triggered by a re-arrangement of the chromospheric and coronal field structure due to the emergence of sub-photospheric material carrying fresh magnetic field. A re-connection with the pre-existing field will take place if the emerging field is of opposite polarity. If in the process open field lines are generated above the flaring region, then one should see type-III like emission at metric wavelengths since the electrons which are accelerated at the lower levels gain access to open field lines and propagate well out into the corona (Kundu, 1996a). In the present case, the exact onset time of the CME is not known since the LASCO can image the

GAURIBIDANUR RADIO HELIOGRAM - 109 MHz

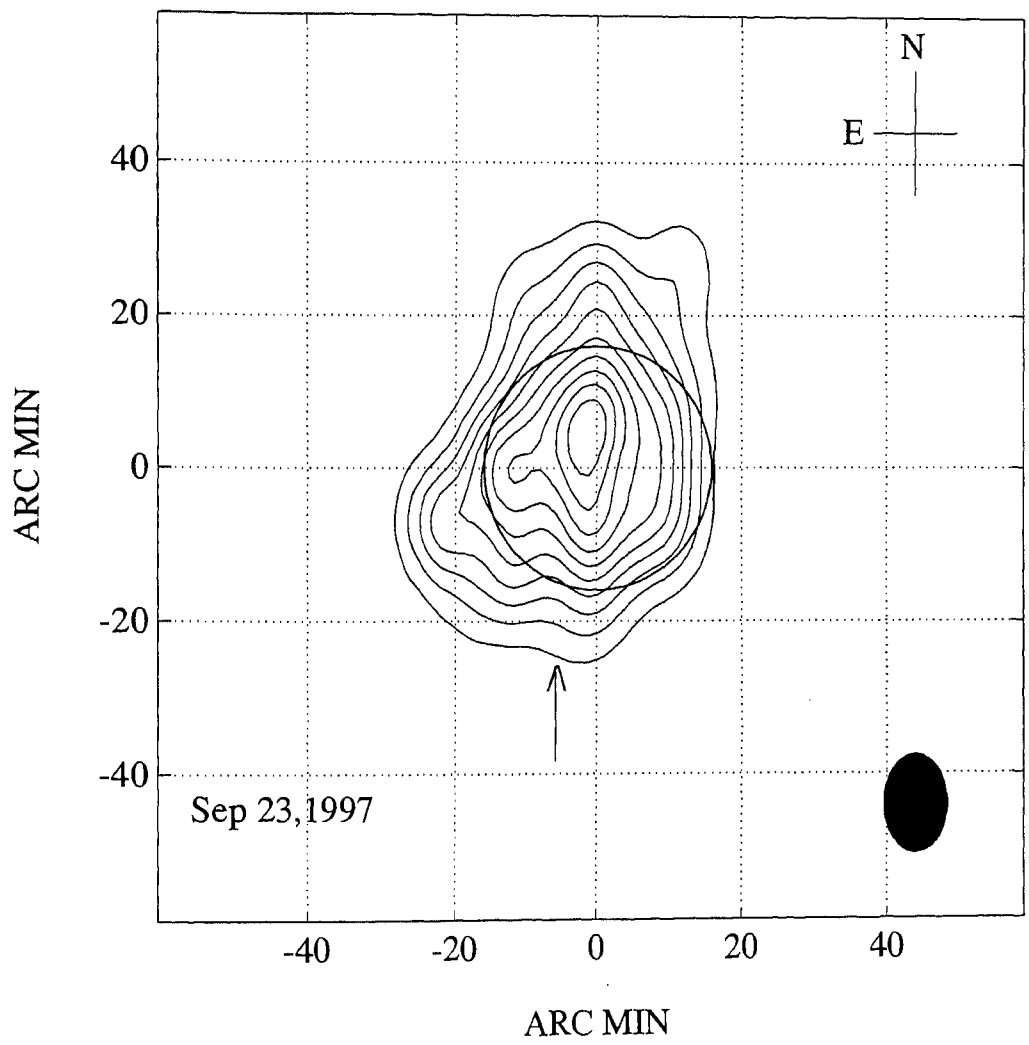


Figure 7.4: Coronal hole (indicated by the arrow mark) observed with the GRH at 109 MHz.

GAURIBIDANUR RADIO HELIOGRAM - 109 MHz

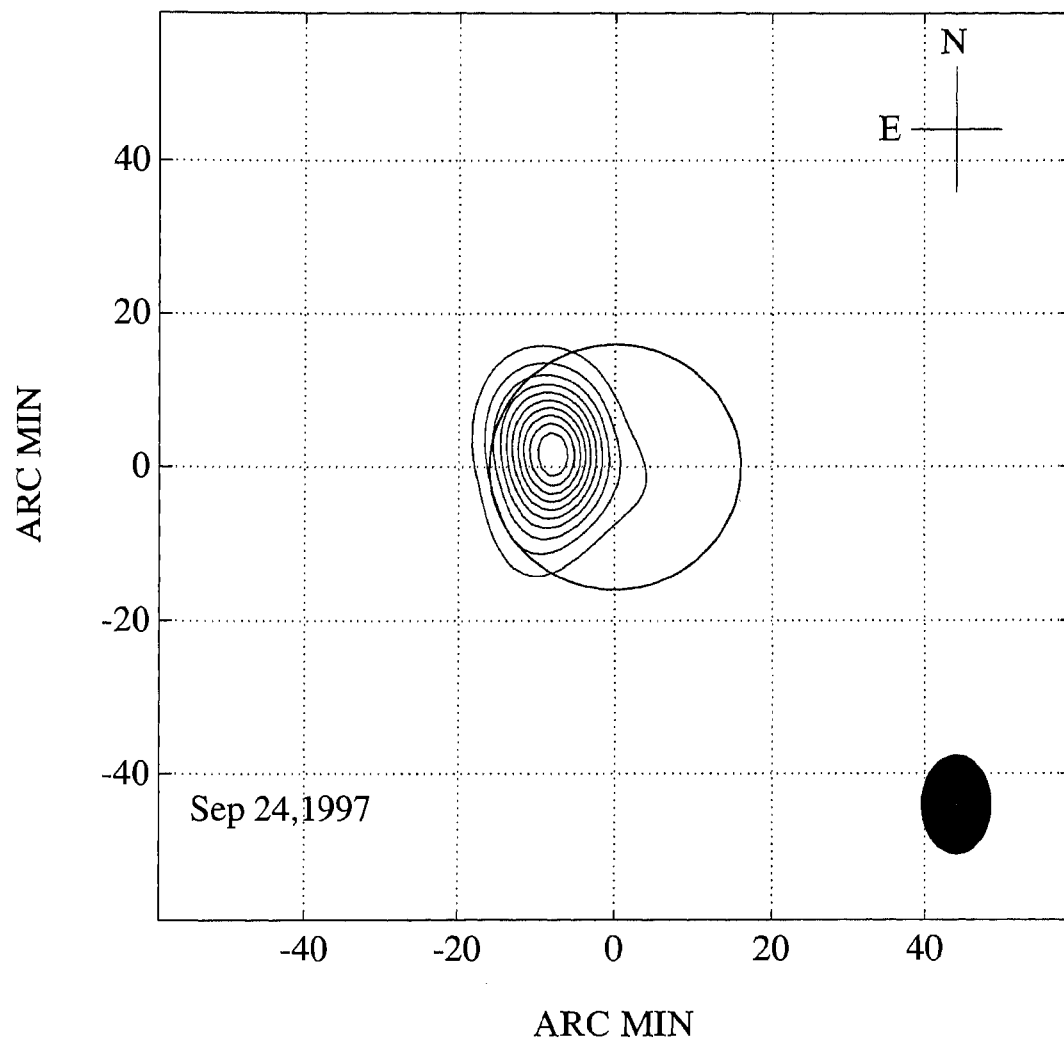


Figure 7.5: Type III burst observed with the GRH.

GAURIBIDANUR RADIO HELIOGRAM - 109 MHz

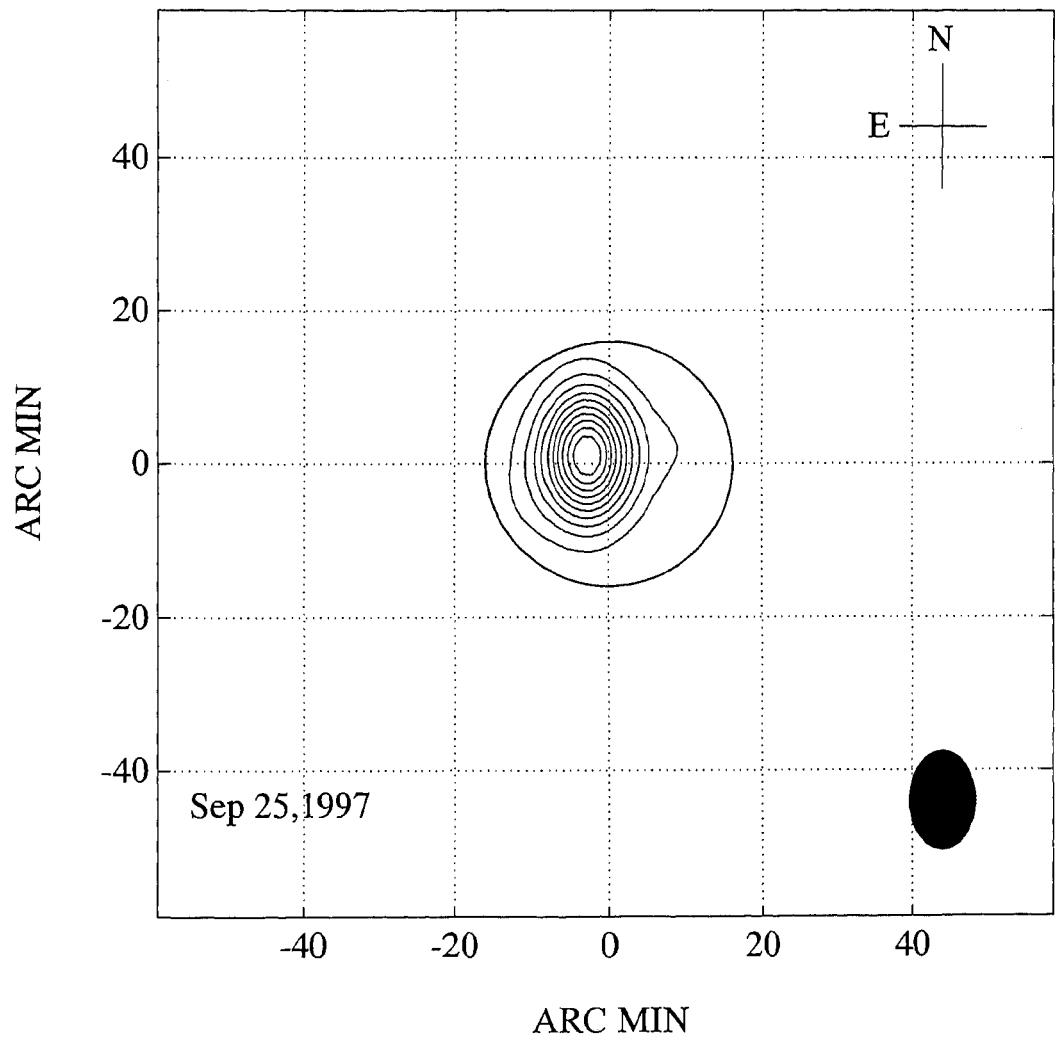


Figure 7.6: Type III burst observed the following day.

corona only above $1.1 R_{\odot}$ (Brueckner et al. 1992), but it is clear that the event must have taken place definitely prior to 23:48 UT. Comparing this with timings of the type III bursts, we can conclude that in the present case type III activity was certainly not a precursor to the CME, i.e. the CME was not driven by the flare. In other words, the non-thermal emission at a given frequency occurs after the CME has passed the corresponding plasma level. A similar conclusion has been reached earlier by Gopalswamy and Kundu (1993) using radio and white-light observations. The observations of radio burst by us at 06.30 UT, much after the event has taken place, suggests continuous outflow of the CME material. It is possible that the X-ray flare might have been generated due to the reconnection of the newly emerged magnetic field structure connected to the CME, with the open field lines (of opposite polarity) of the pre-existing CH. This evidence supports the idea that the open magnetic field lines in the CH facilitate the release of a CME (Hewish and Bravo, 1986).

7.4 CME event of October 24, 1997 and mass estimation

Estimates of CME masses are important in understanding the energetics of the CME as well its mass flux contribution to the solar wind. During a CME, a mass of about $10^{14} - 10^{16}$ g is added to the solar wind. In this context, observations of CMEs at radio wavelengths offer several advantages over those in other wavelength regimes. Because there is no occulting disk, CMEs can, in principle, be imaged against the disk of the Sun in a manner similar to the SXR detection. However, radio observations of thermal plasma are sensitive to a broad range of temperature, from chromospheric to coronal, by

virtue of the $T^{-1/2}$ dependence of the thermal free-free emissivity (optically thin case). SXR's are insensitive to sub-coronal temperatures (Bastian and Gary, 1997). Moreover, since the thermal electrons contained in a CME emit detectable bremsstrahlung radiation at radio wavelengths, one can estimate the mass released during a CME by observing the change in the thermal emission (Sheridan et al. 1978; Gopalswamy and Kundu, 1992). Finally, radio observations can be carried out using ground based instruments. In this section, we report the mass estimate of a halo CME observed with the GRH. Though measurements of the CME mass using the radio data have been reported earlier, none of them were using halo CMEs. The halo CMEs are of great interest for their potential geomagnetic effects and their influence on the near-Earth space environment. A study of such events will be of great benefit in space weather analysis (Bastian and Gary, 1997).

7.4.1 Observations

A halo CME originating near the central meridian was observed on October 23, 1997 with the instruments LASCO and EIT on board SOHO. According to the 1997 SOHO LASCO CME list, the onset of this event was coincident with a filament disappearance around 13:58 UT. A transient CH and coronal dimming was noticed in the YOHKOH SXR images. In the GRH image taken in the aftermath of the CME, there was only a massive restructuring of the corona. In Figure 7.8, one can clearly notice this from the prominent bulges seen near the north and south limbs. These bulges are not there in the pre-event map (Figure 7.7) obtained on October 23, 1997. Unlike the events reported in the previous two sections, this particular CME was not accompanied by any non-thermal radio bursts (Solar Geophysical Data, December 1997). The SXR images obtained with the YOHKOH on October 23, 1997

and October 24, 1997 is shown in Figures 7.9 and 7.10. One can see that the active region that was there close to the center in Figure 7.9 is not present in Figure 7.10. So it is possible that the halo CME event of October 23, 1997 might be closely associated with this active region.

7.4.2 Mass estimation

According to Jackson (1985), in the aftermath of a CME, material gets continuously expelled from the inner corona in the region between the leading edge of the CME and the solar surface, even after the white-light CME had moved to larger heights in the corona. In one case study with the HELIOS B photometer, they found that even 1.5 days after the event had taken place, coronal material continued to flow past the field of view of the photometer. So it is possible that the bulgings seen in the radio map in Figure 7.8 might be due to the CME material. One can make an order-of-magnitude estimate of the density and mass of the CME from this. Since it well known that the emission from the CMEs is optically thin (Bastian and Gary, 1997), the brightness temperature due to the thermal emission from a CME is (Sheridan et al. 1978):

$$T_{bCME} = T_e(1 - e^{-\tau}) \approx T_e\tau \quad (7.1)$$

where T_e is the coronal electron temperature. It is assumed that the CME material is at the coronal temperature (Wagner, 1984). The optical depth (τ) of the corona is given by:

$$\tau = 0.2T_e^{-3/2}f^{-2} \int_0^\infty n_{CME}^2(s)ds \quad (7.2)$$

where n_{CME} is the density of the CME in cm^{-3} and f is the frequency of observation in Hz. Since the CME is of finite depth along the line of sight, one can replace $\int_0^\infty n_{CME}^2 ds$ in the above equation by $\langle n_{CME}^2 \rangle L$, where L (cm) is

the thickness (depth) of the CME along the line of sight (Sheridan et al. 1978).

Therefore we have,

$$T_{bCME} = 0.2T_e^{-1/2}f^{-2} \langle n_{CME}^2 \rangle L \quad \text{°K} \quad (7.3)$$

i.e.

$$\langle n_{CME} \rangle = \left(5L^{-1}T_{bCME}T_e^{1/2}f^2 \right)^{1/2} \text{ cm}^{-3} \quad (7.4)$$

In the present case, $T_{bCME} \approx 3.5 \times 10^5$ K and $f = 109$ MHz. We have assumed the depth (L) of the CME to be the same as the observed radial width (Gopalswamy and Kundu, 1992), which is $1.8 R_\odot$ in the present case. Therefore we have $\langle n_{CME} \rangle = 1.28 \times 10^7 \text{ cm}^{-3}$. Assuming that the corona consists of fully ionized hydrogen and helium with helium being 10% as abundant as hydrogen (Athay, 1976), one finds that each electron is associated with approximately 2×10^{-24} gm of material². Therefore the mass of the CME is given by,

$$M_{CME} = 2 \times 10^{-24} \left[5L^{-1}T_{bCME}T_e^{1/2}f^2 \right]^{1/2} V \quad \text{gm} \quad (7.5)$$

where V is the volume of the CME. In the present case, the volume was determined by multiplying the radial and lateral widths ($1.8 R_\odot$ and $2 R_\odot$) of the difference image in Figure 7.11 with the assumed depth ($1.8 R_\odot$) and the value is $\approx 2.2 \times 10^{33} \text{ cm}^3$. Substituting all the values in equation (7.5), we get $M_{CME} \approx 5.7 \times 10^{16}$ g. A similar mass value (2.1×10^{16} g) was obtained by Howard et al. (1984) for the halo CMEs observed by the SOLWIND coronagraph during the period 1979-81.

²Since there is 10% helium abundance, in every 100 electrons in the solar atmosphere, the contribution from hydrogen will be 80 and that of helium will be 20. At the same time, for every 100 electrons, there will be 120 nucleons, i.e. 80 protons from hydrogen and 20 protons + 20 neutrons from helium. Thus with each electron, 1.2 nucleons are associated. This implies that the mass associated with each electron is $1.2 \times 1.692 \times 10^{-24} \approx 2 \times 10^{-24}$ gm.

GAURIBIDANUR RADIO HELIOGRAM - 109 MHz

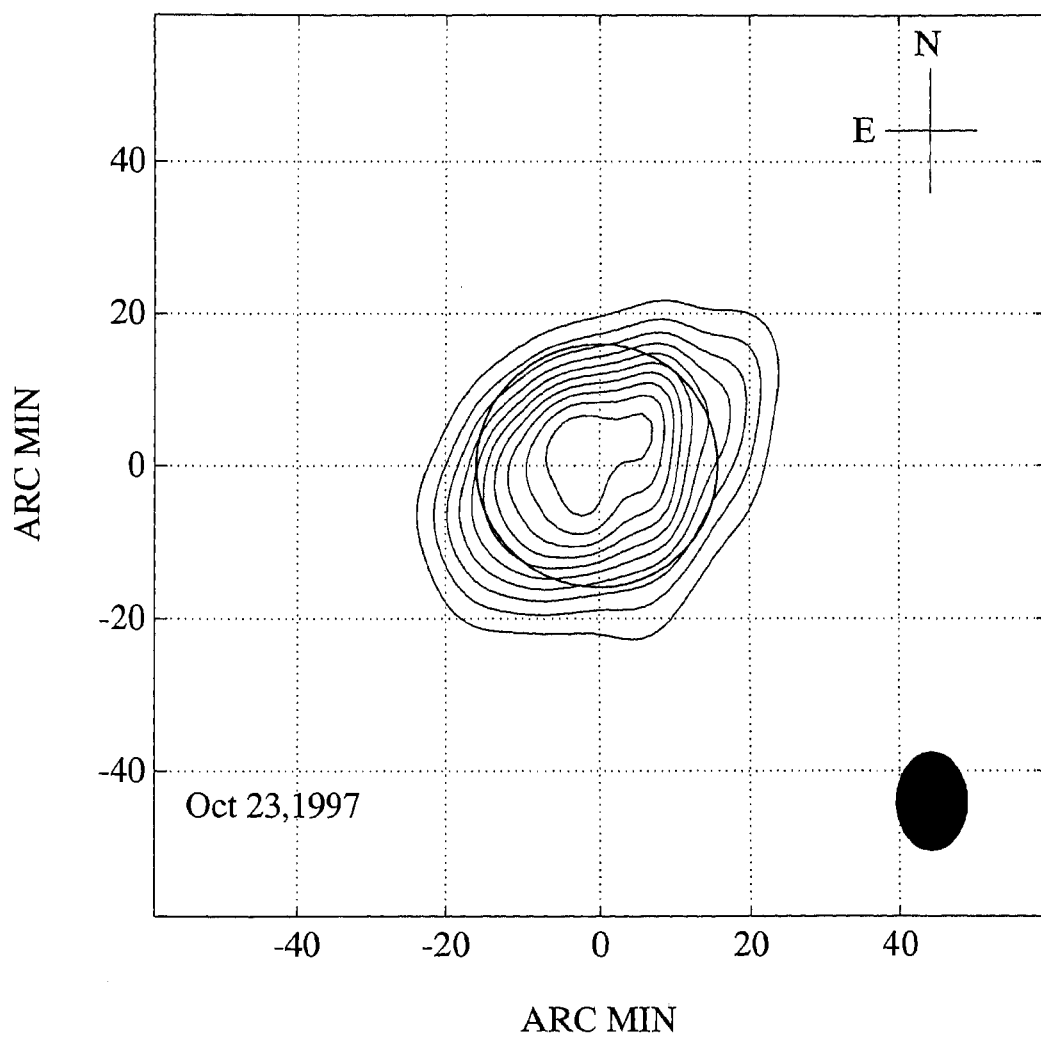


Figure 7.7: Radio map prior to the CME. $T_b = 0.636 \times 10^6$ K and the contour interval is 0.6×10^5 K.

GAURIBIDANUR RADIO HELIOGRAM - 109 MHz

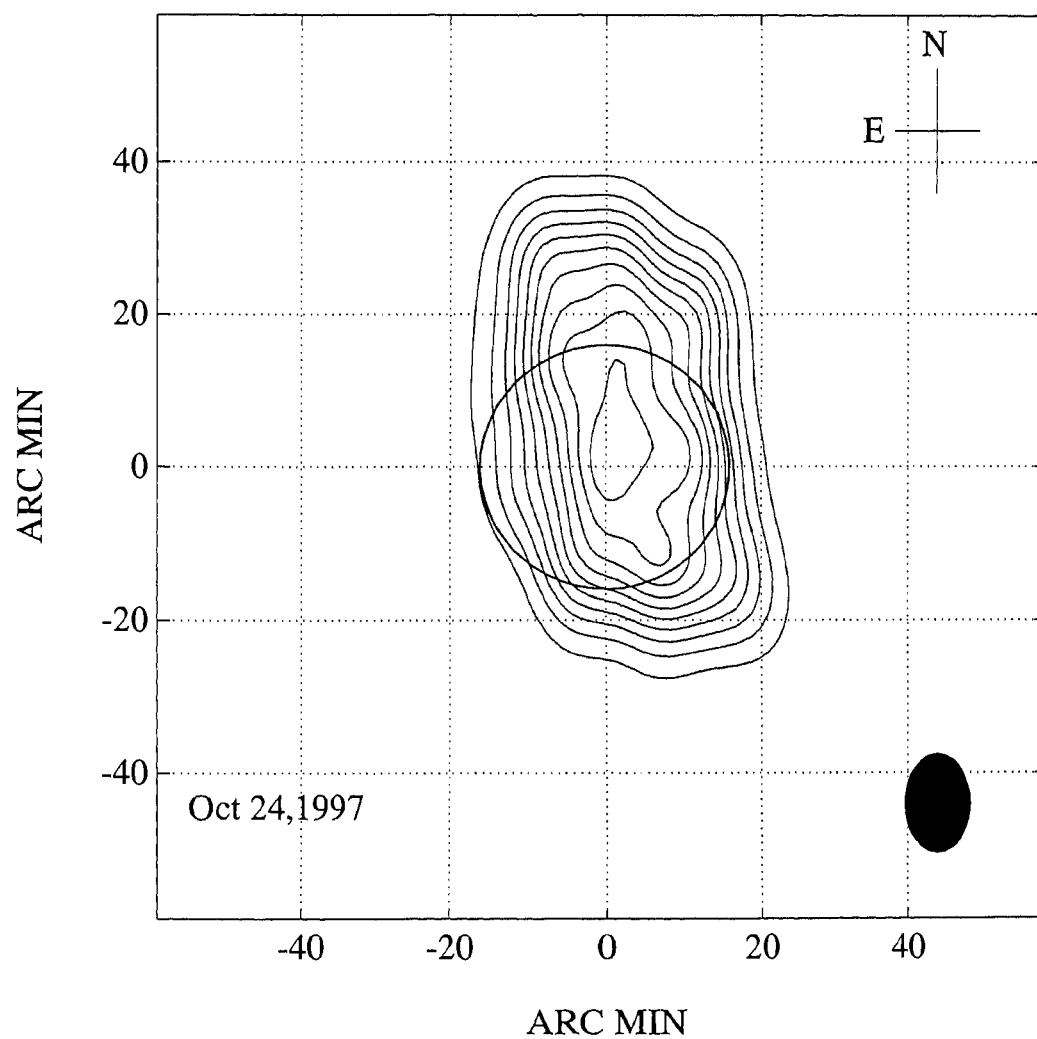


Figure 7.8: Radio map after the CME has taken place. $T_b = 0.497 \times 10^6$ K and the contour interval is 0.5×10^5 K.

Figure 7.9: SXR image obtained with the YOHKOH on October 23, 1997 at 18:53:38 UT. North is straight up and East is to the left.

7-23-OCT-97 08:53:39 QT/H Open /
AIMg Half Norm C 30 30208.0 512x512

Figure 7.10: SXR image obtained with the YOHKOH on October 24, 1997 at 13:55:56 UT. North is straight up and East is to the left. One can clearly notice the absence of the active region (close to the center) which was there in Figure 7.9.



1 24-OCT-97 13:55:56 QT/H Open /
AlMg Half Norm C 30 30208.0 512x512

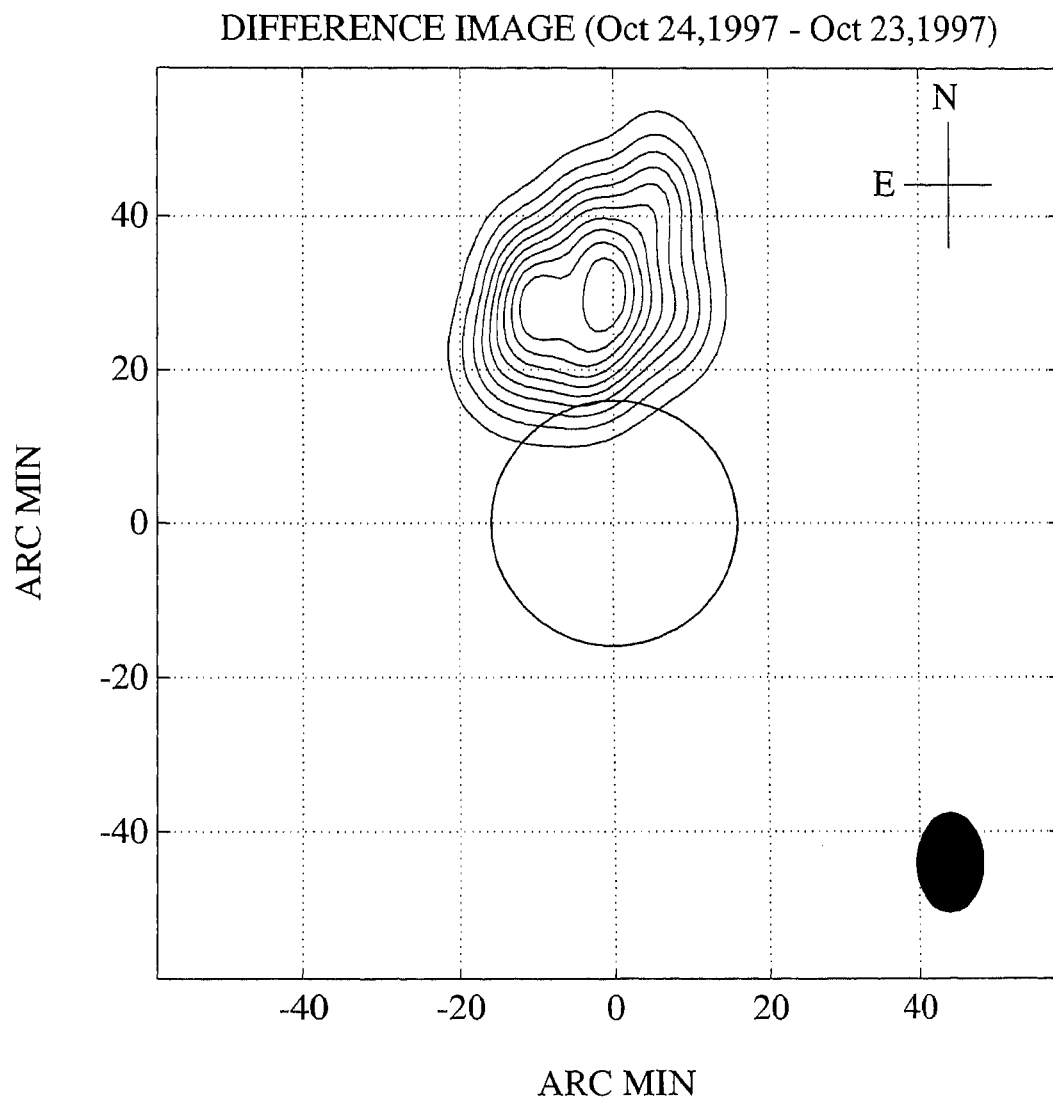


Figure 7.11: Difference map obtained by subtracting pre-event map (Figure 7.7) from the post-event map (Figure 7.8). Peak T_b is 3.5×10^5 K and the contour interval is 0.4×10^4 K.

Because of the time difference between the occurrence of the CME and the radio observations, and a close agreement of the mass value in the present case with that ($\sim 5 \times 10^{16}$ g) reported for the slower-moving persistent features of the CMEs observed by the HELIOS B spacecraft (Jackson, 1985), it is possible that the estimated mass in the present case might not correspond to material ejected during the initial phase of the CME.

The GRH observations presented in this chapter show possible association of CMEs with noise storms, coronal holes and type III radio bursts. Since the duration of the observations are limited to the transit of the source over the local meridian at Gauribidanur, detailed temporal and spatial correlation studies could not be carried out. A tracking system which would enable us to observe atleast ± 2 hrs around meridian transit will be installed in the GRH in the near future. It would then be possible to study in detail radio emission from CMEs at large distances from the Sun.

Chapter 8

Summary and comments

We have built a new radioheliograph for obtaining two-dimensional pictures of the solar corona at distances of about $1.1 - 1.6 R_{\odot}$ from the center of the Sun. The basic receiving element used in the heliograph is a Log periodic dipole (LPD), which enables in carrying out observations over a wide range of frequencies. The heliograph is a T-shaped array with 16 group of LPDs along a E-W arm and another 16 group of LPDs along a South arm. The signals from these 32 groups are correlated in a 1024 channel digital correlator receiver, which outputs the complex visibilities pertaining to all the 512 different baselines. Walsh switching technique is used for removing DC offsets in the A/D convertor and coupling between the input signal channels to the correlator.

A calibration scheme, which is a hybrid of the principles of closure and redundant baseline techniques, is described for removing the phase errors from the complex visibilities observed with the heliograph. It is shown that the maps produced using this scheme closely agree with those made at other wavelengths as well as using other techniques. The dynamic range of the images is not optimum since the aspect of signal-to-noise ratio has not been

included in our scheme. It should be possible to combine the present scheme with that of self-calibration to improve the dynamic range. The idea is to get the position of the structures basically correct using the present scheme and then use the self-calibration to improve the dynamic range.

One-dimensional observations carried out with the E-W arm of the heliograph during the period Feb 20-22, 1995 revealed the presence of a discrete source in the corona, which showed regular movement across the solar disk. These observations made simultaneously at two different frequencies, viz. 51 and 77 MHz were used to estimate the altitude of the plasma levels corresponding to the above two frequencies, independent of any density models. The close positional correspondence between the active regions in the soft X-ray pictures obtained with YOHKOH and the discrete source in the radio map is also shown.

A detailed discussion of the existing literature on the possible reasons for the low values of the observed T_b of the quiet Sun at frequencies < 100 MHz is presented. Some of the suggested possibilities were checked using the data obtained with the GRH on days when no non-thermal burst activity was seen in our records. The present observations imply that scattering alone may not be responsible for the low values of the observed T_b and the variations in it. Radio maps made with the GRH showing the effects of the coronal streamers and noise storms on the quiet Sun brightness distribution are presented.

Observational evidence indicating the possibility of predicting the forerunners of the CME through low frequency radio observations are presented. The mass of the coronal material that was possibly associated with a halo CME event was estimated. It is pointed out that the mass of the slowly moving, persistent features of the CME may be slightly higher than that ejected during the initial phase of the event.

Bibliography

- [1] Alissandrakis, C.E., Lantos, P. and Nicolaidis, E.: 1985, *Sol. Phys.*, **97**, pp.267-282.
- [2] Alissandrakis, C.E.: 1994, *Adv. Space Res.*, **14 (4)**, pp.81-91.
- [3] Alissandrakis, C.E. and Lantos, P.: 1996, **165**, *Sol. Phys.*, pp.61-81.
- [4] Athay, R.G.: 1976, *The Solar Chromosphere and Corona: Quiet Sun*, Astrophysics and Space Science Library, Volume 53, D.Reidel Publishing Company.
- [5] Aubier, M., Leblanc, Y. and Boischot, A.: 1971, *Astr. Astrophys.*, **12**, pp.435-441.
- [6] Avignon, Y. et.al.: 1975, *Sol. Phys.*, **45**, pp.141-145.
- [7] Axisa, F. et.al.: 1971, *Sol. Phys.*, **19**, pp.110-127.
- [8] Bastian, T.S. and Gary, D.E.: 1997, *J. Geophys. Res.*, **102**, A7, pp.14031-14040.
- [9] Bazelyan, L.L.: 1987, *Sol. Phys.*, **112**, pp.107-117.
- [10] Borkowski, K.M.: 1982, *Sol. Phys.*, **81**, pp.207-215.

- [11] Bougeret, J.L. and Steinberg, J.L.: 1977, *Astr. Astrophys.*, **61**, pp.777-783.
- [12] Bracewell, R.N. and Preston, G.W.: 1956, *Astrophys. J.*, **123**, pp.14-29.
- [13] Broussard, R.M. et.al.: 1978, *Sol. Phys.*, **56**, pp.161-183.
- [14] Brueckner, G.E.: 1982, *Proc. of the 4th CESRA Workshop on Solar Noise Storms*, eds. A.O. Benz and P. Zlobec, p255.
- [15] Brueckner, G.E. et.al.: 1992, *Proc. of the 1st SOHO Workshop held at Annapolis, Maryland, USA*.
- [16] Chen, J. et.al.: 1997, *Astrophys. J.*, **490**, L191-194.
- [17] Christiansen, W.N. and Högbom, J.A.: 1969, *Radio Telescopes*, Cambridge University Press.
- [18] Cornwell, T.J. and Wilkinson, P.N.: 1981, *M.N.R.A.S.*, **196**, pp.1067-1086.
- [19] Cornwell, T.J. and Fomalont, E.B.: 1989, in *Synthesis Imaging in Radio Astronomy*, Astr. Soc. of the Pacific, Conf. Series Vol.6, (eds.) Perley, R.A., Schwab, F.R. and Bridle, A.H.
- [20] Cotton, W.D.: 1981, *Astron. J.*, **84**, pp.1122-1128.
- [21] Dulk, G.A. and Sheridan, K.V.: 1974, *Sol. Phys.*, **36**, pp.191-202.
- [22] Dulk, G.A. et.al.: 1976, *Sol. Phys.*, **49**, pp.369-394.
- [23] Dulk, G.A. et.al.: 1977, *Sol. Phys.*, **52**, pp.349-367.
- [24] Duncan, R.A.: 1979, *Sol. Phys.*, **63**, pp.389-398.

- [25] Ekers, R.D.: 1989, in *Synthesis Imaging in Radio Astronomy*, Astr. Soc. of the Pacific, Conf. Series Vol.6, (eds.) Perley, R.A., Schwab, F.R. and Bridle, A.H.
- [26] Elgaroy, O.: 1977, *Solar Noise Storms*, Pergamon Press, Oxford.
- [27] Erickson, W.C. et.al.: 1977, *Sol. Phys.*, **54**, pp.57-63.
- [28] Ferguson, B.G.: 1981, *Sol. Phys.*, **69**, pp.185-209.
- [29] Feynmann, J. and Martin, S.F.: 1995, *J. Geophys. Res.*, **100**, pp.3355-3367.
- [30] Fokker, A.D.: 1965, *Bull. Astr. Ins. Netherlands*, **18**, pp.111-124.
- [31] Golap, K. and Sastry, Ch.V.: 1994, *Sol. Phys.*, **150**, pp.295-304.
- [32] Golap, K.: 1998, *Ph.D. Thesis*, University of Mauritius.
- [33] Gonzalez, W.D. et.al.: 1996, *Geophys. Res. Lett.*, **23**, No.19, pp.2577-2580.
- [34] Gopalswamy, N. and Kundu, M.R.: 1992, *Astrophys. J.*, **390**, L37-39.
- [35] Gopalswamy, N. and Kundu, M.R.: 1993, *Sol. Phys.*, **143**, pp.327-343.
- [36] Gopalswamy, N. et.al.: 1997, *Astrophys. J.*, **486**, pp.1036-1044.
- [37] Gosling, J.T.: 1993, *J. Geophys. Res.*, **98**, pp.18937-18949.
- [38] Granuland, J., Thompson, A.R. and Clark, B.G.: 1978, *IEEE Transactions on Electromagnetic Compatibility*, Vol. EMC-20, No.3, pp.451-453.
- [39] Habbal, S.R. et.al.: 1996, *J. Geophys. Res.*, **101**, pp.19943-19955.

- [40] Hewish, A. and Bravo, S.: 1986, *Sol. Phys.*, **106**, pp.185-200.
- [41] Hey, J.S.: 1946, *Nature*, **157**, pp.47-48.
- [42] Högbom, J.A.: 1974, *Astr. Astrophys. Suppl.*, **15**, pp.417-426.
- [43] Howard, R.A. et.al.: 1984, *Adv. Space Res.*, **4** (7), pp.307-310.
- [44] Hundhausen, A.J.: 1993, *J. Geophys. Res.*, **98**, pp.13177-13200.
- [45] Jackson, B.V., Sheridan, K.V. and Dulk, G.A.: 1979, *Proc. Astr. Soc. Australia*, **3** (6), pp.387-389.
- [46] Jackson, B.V.: 1985, *Sol. Phys.*, **100**, pp.563-574.
- [47] Jennison, R.: 1958, *M.N.R.A.S.*, **118**, pp.276-284.
- [48] Kahler, S.W.: 1992, *Ann. Rev. Astron. Astrophys.*, **30**, pp.113-141.
- [49] Kai, K., Melrose, D.B. and Suzuki, S.: 1985, in *Solar Radio Physics*, eds. D.J. McLean and N.R.Labrum, Cambridge University Press, p415.
- [50] Kassim, N.E. et.al.: 1993, *Astron. J.*, **106**(6), pp.2218-2228.
- [51] Kerdraon, A.: 1979, *Astr. Astrophys.*, **71**, pp.266-268.
- [52] Kerdraon, A. et.al.: 1983, *Astron. Astrophys.*, **265**, L19-21.
- [53] Koshishi, H., et al.: 1994, *Publ. Astron. Soc. Japan*, **46**, L33-L36.
- [54] Kraus, J.D.: 1966, *Radio Astronomy*, McGraw-Hill.
- [55] Kundu, M.R.: 1965, *Solar Radio Astronomy*, Interscience, Newyork.
- [56] Kundu, M.R., Gergely, T.E. and Erickson, W.C.: 1977, *Sol. Phys.*, **53**, pp.489-496.

- [57] Kundu, M.R. et.al.: 1983, *Sol. Phys.*, **83**, pp.385-389.
- [58] Kundu, M.R. et.al.: 1987, *Sol. Phys.*, **108**, pp.113-129.
- [59] Kundu, M.R. and Gopalswamy, N.: 1990, *Sol. Phys.*, **129**, pp.133-152.
- [60] Kundu, M.R., et.al.: 1994, *Astrophysical J.*, **427**, L59-62.
- [61] Kundu, M.R.: 1996, *Astrophys. and Space Sci.*, **243**, pp.15-22.
- [62] Kundu, M.R.: 1996, in *Reviews of Radio Science*, at the 25th General Assembly of the URSI held at Lille, France.
- [63] Lang, K.R. and Willson, R.F.: 1987, *Astrophys. J.*, **319**, pp.514-519.
- [64] Lantos, P. and Avignon, Y.: (1975), *Astr. Astrophys.*, **41**, pp.137-142.
- [65] Lantos, P. et.al.: 1981, *Astron. Astrophys.*, **101**, pp.33-38.
- [66] Lantos, P., et.al.: 1987, *Sol. Phys.*, **112**, pp.325-340.
- [67] Lantos, P. and Alissandrakis, C.E.: 1994, *Adv. Space Res.*, **14(4)**, pp.97-102.
- [68] Lantos, P. and Alissandrakis, C.E.: 1996, *Sol. Phys.*, **165**, pp.83-98.
- [69] Leblanc, Y. and le Squeren, A.M.: (1969), *Astr. Astrophys.*, **1**, pp.239-248.
- [70] Leblanc, Y., Kuiper, T.B.H. and Hansen, S.F.: 1974, *Sol. Phys.*, **37**, pp.215.
- [71] Leblanc, Y. and De la noë, J.; 1976, *Sol. Phys.*, **52**, pp.133-139.
- [72] McLean, D.J. and Melrose, D.B.: 1985, in *Solar Radio Physics*, eds. D.J. McLean and N.R. Labrum, Cambridge University Press, p241.

- [73] McLean, D.J.: 1973, *Proc. Astron. Soc. Australia*, **2**, pp.222-226.
- [74] McMullin, J.N. and Helfer, H.L.: 1977, *Sol. Phys.*, **53**, pp.471-488.
- [75] Mercier, C. et.al.: 1984, *Sol. Phys.*, **92**, pp.375-381.
- [76] Moutot, M. and Boischoy, A.: 1961, *Ann. d'Astrophys.*, **24**, pp.171-179.
- [77] Nakajima, H. et al.: 1993, *Nobeyama Radio Observatory report*, **339**.
- [78] Nelson, G.J., Sheridan, K.V. and Suzuki, S.: in *Solar Radio Physics*, eds. D.J. McLean and N.R. Labrum, Cambridge University Press, p131.
- [79] Newkirk, G.: 1961, *Astrophys. J.*, **133**, pp.983-1013.
- [80] Newkirk, G.: 1967, *Ann. Rev. Astron. Astrophys.*, **5**, pp.213-266.
- [81] Noordam, J.E. and A.G. de Bruyn : 1982, *Nature*, **299**, pp.597-600.
- [82] Pawsey, J.L. and Yabsley, D.E.: 1949, *Aust. J. Sci. Res.*, **A 3** , pp.198-213.
- [83] Pearson, T.J. and Readhead, A.C.S.: 1984, *Ann. Rev. Astron. Astrophys.*, **22**, pp.978-130.
- [84] Perley, R.A.: 1989, in *Synthesis Imaging in Radio Astronomy*, Astr. Soc. of the Pacific, Conf. Series Vol.6, (eds.), Perley, R.A., Schwab, F.R. and Bridle, A.H.
- [85] Pick, M.: 1996, *Astrophys. and Space Sci.*, **243**, pp.179-186.
- [86] Press, W.H., et al.: 1992, *Numerical Recipes in Fortran*, Second Edition, Cambridge University Press, pp.51-63.

- [87] Readhead, A.C.S. and Wilkinson, P.N.: 1978, *Astrophys. J.*, **223**, pp.25-36.
- [88] Robinson, R.D.: 1983, *Proc. Astr. Soc. Australia*, **5** (2), pp.208-211.
- [89] Rogers, A.E.E., et al.: 1974, *Astrophys. J.*, **193**, pp.293-301.
- [90] Riddle, A.C.: 1974, *Sol. Phys.*, **36**, pp.375-381.
- [91] Rumsey, V.H.: 1966, *Frequency Independent Antennas*, Academic Press.
- [92] Saito, K.: 1972, *Ann. Tokyo Astron. Obs.*, **13**, No.2, pp.93-148.
- [93] Sastry, Ch.V. et.al.: 1981, *Sol. Phys.*, **73**, pp.363-377.
- [94] Sastry, Ch.V., Shevgaonkar, R.K. and Ramanuja, M.N.: 1983, *Sol. Phys.*, **87**, pp.391-399.
- [95] Sastry, Ch.V.: 1994, *Sol. Phys.*, **150**, pp.285-294.
- [96] Schmahl, E.J., Gopalswamy, N. and Kundu, M.R.: 1994, *Sol. Phys.*, **150**, pp.325-337.
- [97] Schwab, F.R.: 1980, *Proc. S.P.I.E.*, **231**, pp.18-24.
- [98] Schwab, F.R.: 1984, in *Low Frequency Radio Astronomy*, Proc. of Workshop held at NRAO, Erickson, W.E. and Cane, H.V. eds., p55.
- [99] Sheridan, K.V.: 1970, *Proc. Astr. Soc. Australia*, **1**, pp.304-305.
- [100] Sheridan, K.V. et.al.: 1978, *Proc. Astron. Soc. Australia*, **3** (4), pp.249-250.
- [101] Sheridan, K.V.: 1978, *Proc. Astr. Soc. Australia*, **3**, pp.185-194.

- [102] Sheridan, K.V. and Dulk, G.A.: 1980, in *Solar and Interplanetary Dynamics*, IAU Symposium 91, eds. M. Dryer and E. Tandberg-Hanssen, pp.37-43.
- [103] Sheridan, K.V. and McLean, D.J.: 1985, in *Solar Radio Physics*, eds. D.J. McLean and N.R. Labrum, Cambridge University Press, p446.
- [104] Shevgaonkar, R.K.: 1984, in *Low Frequency Radio Astronomy*, Proc. of Workshop held at NRAO, Erickson, W.E. and Cane, H.V. eds., p62.
- [105] Shevgaonkar, R.K., Kundu, M.R. and Jackson, P.D.: 1988, *Astrophys. J.*, **329**, pp.982-990.
- [106] Smerd, S.F.: 1950, *Aust. J. Sci. Res.*, **A 3**, pp.34-59.
- [107] *Solar Geophysical Data*, April 1995, Number 608, Part I.
- [108] *Solar Geophysical Data*, May 1997, Number 633, Part I.
- [109] *Solar Geophysical Data*, June 1997, Number 634, Part I.
- [110] *Solar Geophysical Data*, September 1997, Number 637, Part I.
- [111] *Solar Geophysical Data*, November 1997, Number 639, Part I.
- [112] *Solar Geophysical Data*, December 1997, Number 640, Part I.
- [113] Srivastava, N., Gonzalez, W.D. and Sawant, H.S.: 1997, *Adv. Space Res.*, **20 (12)**, pp.2355-2358.
- [114] Steinberg, J.L. et.al.: 1971, *Astr. Astrophys.*, **10**, pp.362-376.
- [115] Subramanian, K.R. and Sastry, Ch.V.: 1988, *J. Astr. Astrophys.*, **9**, pp.225-229.

- [116] Takakura, T. et.al.: 1967, *Proc. Astron. Soc. Australia*, **1**, pp.56-58.
- [117] Thejappa, G.: 1991, *Sol. Phys.*, **132**, pp.173-193.
- [118] Thejappa, G. and Kundu, M.R.: 1992, *Sol. Phys.*, **140**, pp.19-39.
- [119] Thejappa, G. and Kundu, M.R.: 1994, *Sol. Phys.*, **145**, pp.31-49.
- [120] Thompson, A.R., Moran, J.M. Swenson Jr., G.W.: 1986, *Interferometry and Synthesis in Radio Astronomy*, Wiley-InterScience, pp.78-83.
- [121] Trotter, G. and Lantos, P.: 1978, *Astr. Astrophys.*, **70**, pp.245-253.
- [122] Udayashankar, N.: 1986, *Ph.D. Thesis*, Bangalore University.
- [123] Van Vleck, J.H. and Middleton, D.: 1966, *Proc. IEEE*, **54 (1)**, pp.2-19.
- [124] Wagner, W.J.: 1984, *Ann. Rev. Astron. Astrophys.*, **22**, pp.267-289.
- [125] Wang, Z., Schmahl, E.J. and Kundu, M.R.: 1987, *Sol. Phys.*, **111**, pp.419-428.
- [126] Watanabe, T. et.al.: 1992, *Publ. Astron. Soc. Japan*, **44**, L199-202.
- [127] Weeks, W.L.: 1968, *Antenna Engineering*, McGraw-Hill.
- [128] Wieringa, M.H.: 1991, *Ph.D Thesis*, University of Leiden.
- [129] Wild, J.P. et.al.: 1967 (September), *Proc. I.R.E.E. Australia*, pp.277-384.

RESUME

Name : R.RAMESH

Date of Birth : May 19, 1968

Educational Qualifications:

Course	Subject(s)	Period	Institution
B.Sc	Physics, Maths and Chemistry	1985 - 88	Madurai University
M.Sc	Solid State Physics, Electromagnetic theory, Classical Mechanics and Electronics	1988 - 90	Madurai University
Joint Astronomy Program	Astronomy Techniques, Stellar structure, Plasma Physics and Radiative transfer	1991 - 92	Indian Institute of Science, Bangalore
Ph.D	Solar Radio Astronomy	1992 -	Indian Institute of Astrophysics, Bangalore

Areas of interest :

1. Development of algorithms for Synthesis imaging of the Solar corona.
2. Development of model-independent phase calibration schemes for low frequency radio telescopes.
3. Observations and interpretation of radio emission from the solar corona.

LIST OF PUBLICATIONS

1. **High angular observations of solar noise storm sources**
 - R.Ramesh, K.R.Subramanian and Ch.V.Sastry
 - To appear in **Advances in Space Research**
 - Proceedings of the 32nd COSPAR Scientific Assembly meeting held at Nagoya, Japan.

2. **The Gauribidanur Radio Heliograph**
 - R.Ramesh, K.R.Subramanian, M.S.SundaraRajan and Ch.V.Sastry
 - **Solar Physics**, Vol.181, 1998.

3. **Eclipse observations of compact sources in the outer solar corona**
 - R.Ramesh, K.R.Subramanian and Ch.V.Sastry
 - To appear in **Solar Physics**

4. **Phase calibration scheme for a T-array based on redundancy and closure techniques**
 - R.Ramesh and Ch.V.Sastry
 - Communicated to **Experimental Astronomy**

5. **First results from the Gauribidanur Radio Heliograph**

- R.Ramesh, K.R.Subramanian and Ch.V.Sastry

- **Bulletin of the Astronomical Society of India**, Vol. 26, 1998

- Proceedings of the PRL Golden Jubilee Workshop held at Udaipur, India.

6. **Results from the one-dimensional observations made with the
E-W arm of the Gauribidanur Radio Heliograph**

- K.R.Subramanian, R.Ramesh, M.S.SundaraRajan and Ch.V.Sastry

- **Astrophysics and Space Science**, Vol. 243, 1996

- Proceedings of the IAU Colloquium 154 held at Pune, India.

IN PREPARATION

1. Long wavelength observations of sunspot active regions and
estimation of the electron density of the solar corona.

2. Radio observations of the 'halo' CME event of October 23, 1997
and mass estimation.